A STUDY ON SPHERICAL EXPANDING FLAME SPEEDS OF METHANE,

ETHANE, AND METHANE/ETHANE MIXTURES AT ELEVATED PRESSURES

A Dissertation

by

JAAP DE VRIES

Submitted to the Office of Graduate Studies of
Texas A&M University
in partial fulfillment of the requirements for the degree of

DOCTOR OF PHILOSOPHY

May 2009

Major Subject: Mechanical Engineering

A STUDY ON SPHERICAL EXPANDING FLAME SPEEDS OF METHANE,

ETHANE, AND METHANE/ETHANE MIXTURES AT ELEVATED PRESSURES

A Dissertation

by

JAAP DE VRIES

Submitted to the Office of Graduate Studies of
Texas A&M University
in partial fulfillment of the requirements for the degree of

DOCTOR OF PHILOSOPHY

Approved by:

Chair of Committee,	Eric L. Petersen
Committee Members,	Kalyan Annamalai
	Jerald A. Caton
	Kenneth R. Hall
Head of Department,	Dennis L. O'Neal

May 2009

Major Subject: Mechanical Engineering

ABSTRACT

A Study on Spherical Expanding Flame Speeds of Methane, Ethane, and Methane/Ethane Mixtures at Elevated Pressures. (May 2009)

Jaap de Vries, B.A., Hogeschool van Amsterdam; M.S., University of Central Florida

Chair of Advisory Committee: Dr. Eric L. Petersen

High-pressure experiments and chemical kinetics modeling were performed for laminar spherically expanding flames for methane/air, ethane/air, methane/ethane/air and propane/air mixtures at pressures between 1 and 10 atm and equivalence ratios ranging from 0.7 to 1.3. All experiments were performed in a new flame speed facility capable of withstanding initial pressures up to 15 atm. The facility consists of a cylindrical pressure vessel rated up to 2200 psi. Vacuums down to 30 mTorr were produced before each experiment, and mixtures were created using the partial pressure method. Ignition was obtained by an automotive coil and a constant current power supply capable of reducing the spark energy close to the minimum ignition energy.

Optical cine-photography was provided via a Z-type schlieren set up and a high-speed camera (2000 fps). A full description of the facility is given including a pressure rating and a computational conjugate heat transfer analysis predicting temperature rises at the walls. Additionally, a detailed uncertainty analysis revealed total uncertainty in measured flame speed of approximately ± 0.7 cm/s.

This study includes first-ever measurements of methane/ethane flame speeds at elevated pressures as well as unique high pressure ethane flame speed measurements.

Three chemical kinetic models were used and compared against measured flame velocities. GRI 3.0 performed remarkably well even for high-pressure ethane flames. The C_5 mechanism performed acceptably at low pressure conditions and under-predicted the experimental data at elevated pressures.

Measured Markstein lengths of atmospheric methane/air flames were compared against values found in the literature. In this study, Markstein lengths increased for methane/air flames from fuel lean to fuel rich. A reverse trend was observed for ethane/air mixtures with the Markstein length decreasing from fuel lean to fuel rich conditions.

Flame cellularity was observed for mixtures at elevated pressures. For both methane and ethane, hydrodynamic instabilities dominated at stoichiometric conditions. Flame acceleration was clearly visible and used to determine the onset of cellular instabilities. The onset of flame acceleration for each high-pressure experiment was recorded.

To my beautiful wife

ACKNOWLEDGMENTS

Last but not least, my gratitude goes out to my academic advisor Dr. Eric Petersen whose academic integrity, work ethic, thoroughness, intelligence, and overall pleasant demeanor have set an exceptional standard for all who worked for him.

NOMENCLATURE

A_f	Flame surface area
BTU	British Thermal Units
CC	Combined Cycle
CC	Combined Cycle
CCS	Carbon Capture and Sequestration
CO	Carbon Monoxide
c_p	Specific heat at constant pressure
c_v	Specific heat at constant volume
Da	Damköhler number
$D_{i,j}$	Binary diffusivity
$D_{i,m}$	Diffusivity of component i with respect to the mixture
DLE	Dry Low Emission
DLN	Dry Low NO_x
DOE	Department of Energy
E_A	Activation energy
EIA	Energy Information Administration
EISA	Energy Independence and Security Act
FE	Fossil Energy
GT	Gas Turbine
h_i	Specific enthalpy

HRSG	Heat recovery steam generator
IEO	International Energy Outlook
IGV	Inlet Guide Vanes
IGV	Inlet Guide Vanes
k	Thermal conductivity
Ka	Karlovitz number
LHV	Lower Heating Value
LNG	Liquefied Natural Gas
LPG	Liquefied Petroleum Gas
Ma	Markstein number
$\overline{M}_i$	Molecular mass of species i
$\dot{m}''$	Mass flux
M_L	Markstein length
NG	Natural Gas
NO_x	Nitrous Oxides
OECD	Organization for Economic Cooperation and Development
P	Pressure
Q_{2-3}	Energy added to combustor
Re_c	Critical Reynolds number
R_f	Flame radius
r_P	Compression ratio
R_u	Universal gas constant

S	Flame speed
T	Temperature
T_{amb}	Ambient temperature
T_f	Firing temperature/Flame temperature
UHC	Unburned Hydrocarbons
UHC	Unburned Hydrocarbons
v_x	velocity in the x-direction
W_{cyc}	Useful work
WETO	World Energy Technology Outlook
X_i	Mole fraction
Y_i	Mass fraction

Greek symbols

$\dot{\omega}_i$	Species molar production
α	Thermal diffusivity/Flame stretch
γ	Ratio of specific heat at constant pressure and constant volume
η_c	compressor efficiency
η_{comb}	Combustor efficiency
η_{cyc}	Overall cycle efficiency
η_{ideal}	Ideal cycle efficiency
η_t	turbine efficiency
μ	Viscosity

ρ	Density
σ	Ratio of unburned and burned densities
τ_{chem}	Residence timescale
τ_{res}	Residence timescale

Subscripts and superscripts

0	Unstretched 1-dimensional conditions
b	Burned condition (products)
i	Species "i"
L	Laminar
u	Unburned conditions (reactants)

TABLE OF CONTENTS

LIST OF FIGURES

LIST OF TABLES

Page

CHAPTER I

INTRODUCTION

1.1 Energy Situation in the US

This study focuses on flame speeds of Natural-Gas (NG) fuel blends used by power-generation gas turbines. Demand for high-pressure combustion data of current and future candidate fuels is directly connected to changes in the world's energy supply and demands. A detailed projection and assessment of the international energy markets through 2030 is given in the International Energy Outlook (IEO) presented by the Energy Information Administration (EIA) [1]. The IEO divides global regions into members of the Organization for Economic Cooperation and Development (OECD) and non-members (non-OECD). Additionally, a projection through 2050 is presented in the World Energy Technology Outlook (WETO-H_2) published by the European Commission [2]. Both reports emphasize the importance of the world economic growth as the main driver of the world's energy demand. Due to uncertainty in world economic growth, the IEO contains three projections: a reference case, a high economic growth scenario, and a low economic growth scenario. The WETO-H_2 also describes three scenarios: the business-as-usual reference case, assuming a continuation of existing economic and technological trends; a scenario exploring the consequences of more stringent CO_2 restrictions;

_____

This dissertation follows the style of *Measurement Science and Technology*.

and a "hydrogen case" derived from the assumption of a series of technological breakthroughs in hydrogen technologies.

The findings from the EIA's IEO are consistent with the Annual Energy Outlook (AEO) [3], which focuses on the U.S., and are used in this dissertation. Unless otherwise specified, reference case information will be used.
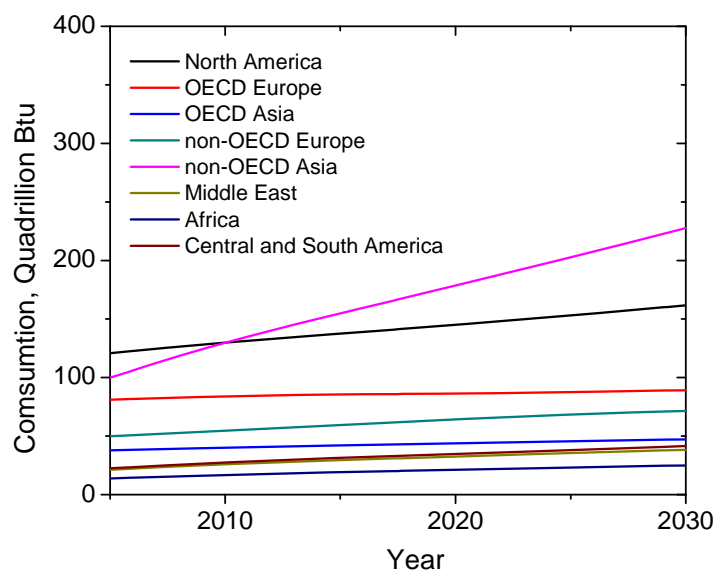
Figure 1. Energy consumption per geographical location projected to 2030, (Source IEO2008 [1])

The world marketed energy consumption by country grouping is shown in Figure 1. The IEO 2008 projects the global energy demand to increase by 50% over the 2005 to 2030 period. In absolute terms, the global energy consumption rises from 447 to 695 quadrillion Btu (131 to 297 x 10^{12} kWh). It is worth noting that this projection is down 7% from the projections made just one year earlier (IEO 2007). This decline is mainly

caused by an expected scenario in which world oil prices will remain relatively high. The high price of conventional fuels is an additional reason why understanding the combustion characteristics of potential alternatives is important. The world oil prices from 1980 to 2030 are shown in Figure 2; the projection after 2008 is shown as a band confined by a high price scenario and the reference case as used in IOE 2008. Figure 1 shows that the largest increases in energy demands originate in non-OECD countries. This observation is mainly caused by the strong economic development and industrialization by China and India as well as population growth.
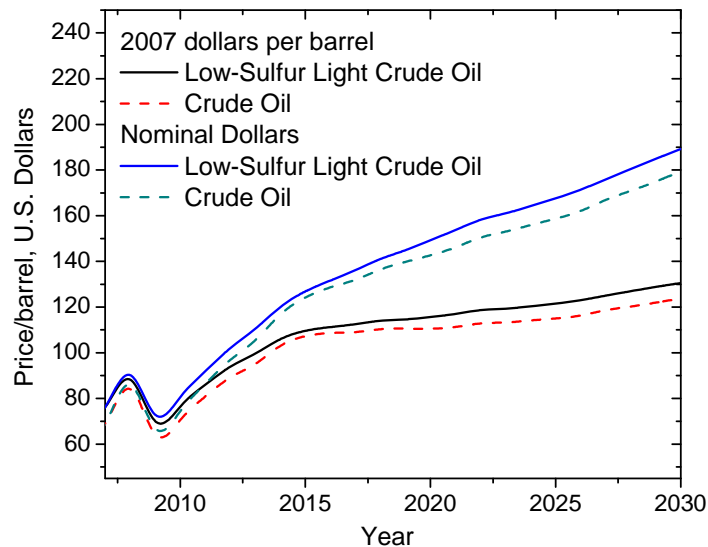
Figure 2. Oil price projections in nominal and 2007 dollars, (Source IEO2008 [1])

The economies of non-OECD countries are projected to grow more than three times faster than OECD countries.

Despite environmental concerns, fossil fuels will continue to be the largest percentage of the projected world-wide energy usage. With 83.6 million barrels of oil equivalent a day, liquid currently supplies the largest share of global energy consumed. Difficulties in finding alternatives in the transportation sector allow the demand for liquids to remain high through 2030. The strain on the conventional liquid market increases the demand for unconventional fuels including biofuels, coal-to-liquid, and gas to liquids. The renewable-liquid demand is expected to increase from 2.5 million barrels to a projected 9.7 million barrels a day.

Figure 3 shows the world marketed energy use by fuel type. Coal and renewable energy are the fastest growing sources. Renewable energy consumption increases due to growing concerns over the environmental impact of fossil burning fuels. The increase in coal is mainly caused by its low price and its relative abundance in China, India, and the U.S.
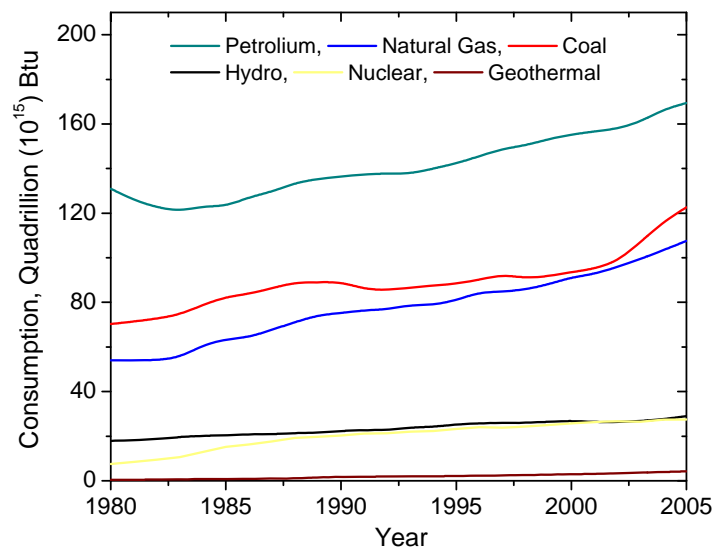
Figure 3. Global energy demand per source (Source IEO2008 [1])

In general, natural gas produces less carbon dioxide than either coal or petroleum. Therefore, greenhouse gas emissions can be reduced by replacing other fossil fuels with natural gas.
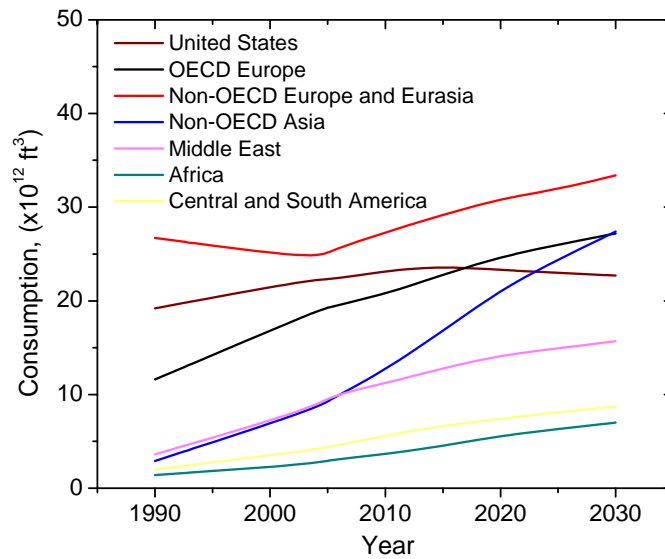
Figure 4. Natural gas consumption per region (Source IEO2008 [1])

The choice of natural gas for electricity generation is attractive because of the high efficiencies that can be reached. Efficiencies of some gas turbines in combined cycle mode can reach up to 65%. Currently, the worldwide natural gas consumption is approximately 100 trillion cubic feet a year and is expected to increase by 50% over the next 25 years. The U.S. consumes about 22 trillion cubic feet, with 19% used for electricity generation. The use of natural gas is expected to increase more rapidly in Europe as shown in Figure 4. The consumption of natural gas is expected to increase in

the next few years in the U.S., followed by a gradual reduction caused by the relatively high gas prices. The rises in shares of coal, renewable and nuclear sources will compensate for the drop in NG usage for electricity generation in the U.S.

An overview of the total world natural gas reserve is shown in Figure 5. The U.S. has 3.4% of the world's gas reserves while consuming 22% of the world's production.
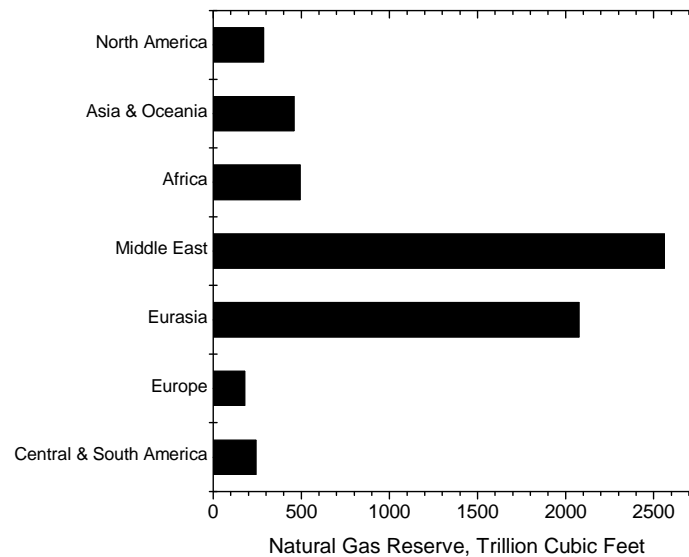
Figure 5. Natural gas reserves per region, 10^{12} cubic feet, (Source IEO2008 [1])

Electricity is the fastest growing form of end-use energy worldwide, and the world's net electricity generation is expected to double over the next 20 years. Currently, 18 trillion kilowatt-hours are used every year. Coal continues to be the dominant source of fuel for electricity generation, although environmental considerations have pushed the development of renewable, nuclear, and natural gas fired power plants. Electrical energy generated per fuel, including a projection through 2030, is listed in Figure 6. Power plants are the most likely candidates to implement alternative or low emitting technologies since little or no modification is necessary for the distribution infrastructure. However, the transportation sector would require changes in the vehicle fleet, fueling stations, and distribution centers.
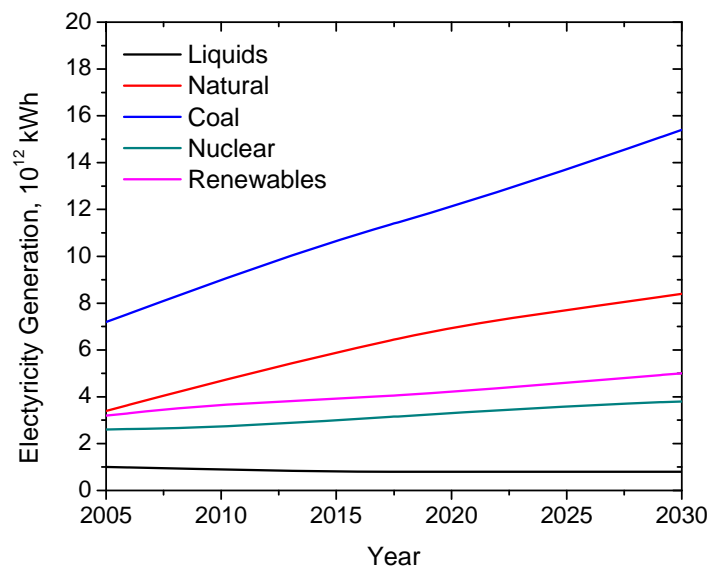
Figure 6. Electricity generation by fuel, 10^{12} kWh. (Source IEO2008 [1])

Within the U.S., several changes are expected to affect the production and demand for energy. The main causes for these changes would be high projected energy prices, slower projected growth in energy demand, increased use of renewable energy, higher domestic oil production, and slower growth in energy imports.

Table 1 shows total global energy consumption, a summary of U.S. energy consumption, and U.S. production per fuel source. Coal, liquids, and natural gas still provide 85% of the U.S. energy consumption.

With the exception of carbon capture and sequestration (CCS) technology, the emissions of CO_2 are proportional to the carbon content in the consumed fuel. Changing the U.S. energy portfolio to fuels with lower carbon content is expected to reduce the growth in CO_2 emissions. However, the total emission of CO_2 is expected to increase from 6000 million metric ton (2008) to about 6850 million metric ton (2030).

Table 1. US fuel consumption per source and as percentage of the global consumption, (Source IEO2008 [1] 2005)

	Consumption			US
	US	(%)	World	Production
Liquids, (Millions Barrels a Day)	20.8	24.9	83.6	5.18
Natural Gas, (Trillion Cubic Feet)	22.1	21.4	103.7	18.05
Coal, (Billion Short Tons)	1.1	17.4	6.5	1.13
Nuclear, (Billion kWh)	787.2	29.9	2630.0	781.99
Renewables, (Billion kWh)	380.4	11.6	3269.7	1052.00

The price of coal is expected to remain relatively constant over the next 10 years around $1.10-$1.20 per million Btu. The electricity prices are expected to increase proportionally to the increase in delivered fuel prices to the plants. Liquid fuel consumption (including biofuels) within the U.S. is currently 20.8 million barrels a day. The increase is expected to be marginal partly because of newly introduced standards for fuel mileage on trucks and cars. The Corporate Average Fuel Economy (CAFE) for Light-Duty Vehicles (LDV) is set to 35 mpg by 2020 by the Energy Independence and Security Act of 2007 (EISA2007). Renewables are expected to increase rapidly in the transportation sector due to AISA2007 requirements of 36 billion gallons of total renewable fuels by 2022. Although most gas turbines are capable of burning biodiesels, the main problem remains consistent availability to power plants.

Instead of measuring the energy consumed per capita, it is sometimes more useful to express the energy consumed per dollar of GDP. This is called the energy intensity and is expected to decrease in the U.S., mainly due to improvements in energy efficiency and a shift to less energy-intensive activities. The energy intensity in the U.S. is projected to decrease by about 2% each year.

The domestic crude oil production, currently estimated at a little over 5 million barrels a day, will increase due to enhanced oil recovery operations. However, eventually the increase in production from small discoveries will fail to offset the decline in production from large fields in Alaska and the Gulf of Mexico.

Many of the expected changes in energy consumption are a result of new regulations and policies concerning an increased demand for energy independence and

environmental sustainability. One of the latest of such laws is the Energy Independence and Security Act (EISA2007). These new regulations include: minimum production of renewable liquids, new efficiency standards for light-duty vehicles, appliance efficiency standards, lighting efficiency standards, industrial electric motor standards, and other requirements concerning housing and energy use in federal buildings. For the industrial sector, the amount of waste energy (quantity and quality) per combustion source will be registered by the EPA, and the DOE is authorized to provide up to $200 million in energy saving grants to industry partnerships. Some of the regulations that are specific to the gas turbine community are provided in the next section.

1.2   Gas Turbine Combustion

Changes in demands and variety of candidate fuels have significantly impacted the design of industrial combustors. A shift to coal-derived gases, renewable gases, renewable liquids, coke oven gases, and flare offgases is expected to impact both the combustor design and performance. Campbell et al. [4] presented the latest technologies available at GE for burning a multitude of fuels, and a summary of the adverse effects experienced by gas-turbine combustors is given by Lieuwen et al. [5]. In addition to the variety of fuels available, more stringent regulatory constraints on the emission of nitrous oxides (NO_x), carbon monoxide (CO), and unburned hydrocarbons significantly alters the design philosophy of modern combustors. To facilitate the combustor design, prior knowledge of fuel combustion characteristics is vital. One of these combustion characteristics is the laminar flame speed.

Laminar premixed flames are of interest not only to the gas-turbine community, but they also serve as fundamental data for modeling reciprocating engines and for validation of complex chemical kinetics models. In this study, the focus is on the impact of flame speed on the prediction of fundamental gas-turbine combustion problems and on chemical model validation as shown in Chapter IV.

Gas Turbines

A gas turbine is a rotary engine that extracts energy from a flow of combustion gas and can be used in several different modes such as power generation, oil and gas, process plants, aviation, and ground transportation. Cohen et al. [6] describes the details of gas-turbine theory, and Boyce [7] presents a handbook focusing on land-based gas turbines. The basic components are the compressor section, the turbine (expansion) section and a combustor. A schematic of a gas turbine can be seen in Figure 7.

In general, the overall efficiency increases with increasing combustion temperature. However, in gas turbines these temperatures are limited by the ability of the first turbine stage to withstand heat in combination with mechanical load.
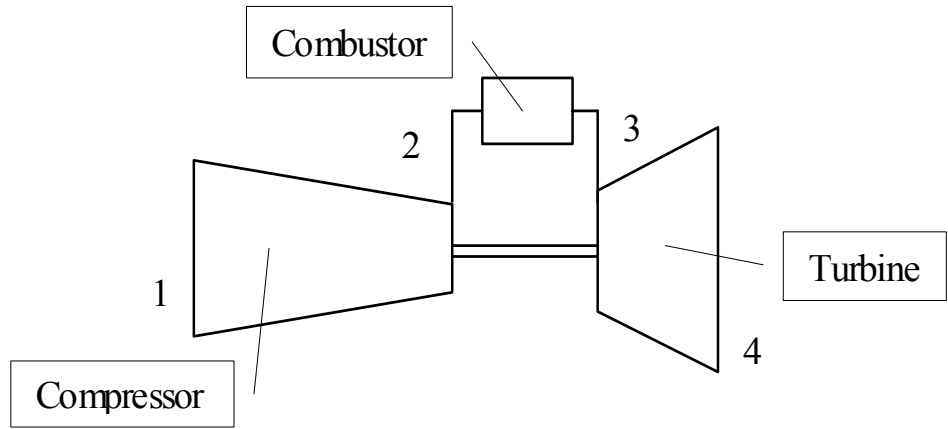
Figure 7. Gas turbine schematic
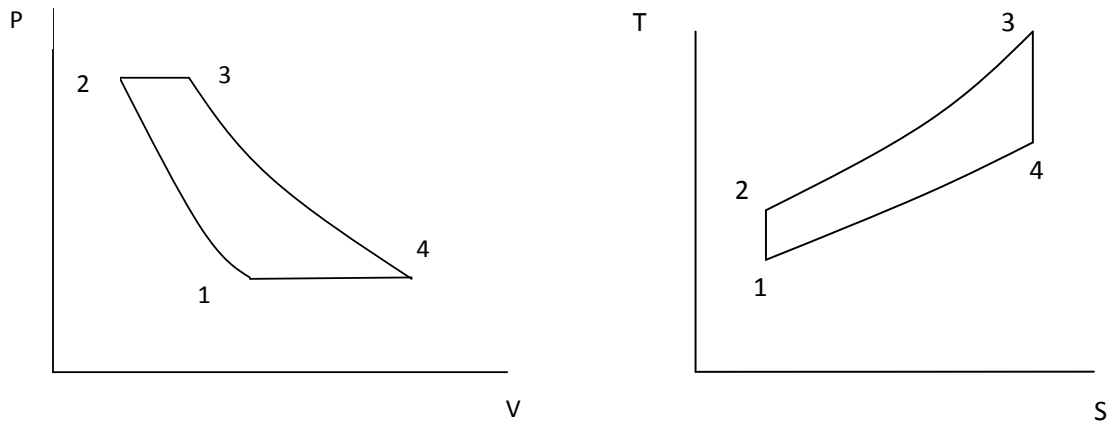
Figure 8. The air standard Brayton cycle

The thermodynamic principle of a gas turbine is founded on the Brayton Cycle which, in the ideal case, consists of two isobaric and two isentropic processes. The isobaric processes happen within the combustion system and the heat recovery system, and the two isentropic processes are the gas compression and the expansion through the turbine. P-v (pressure-volume) and T-S (temperature-entropy) diagram representing the Brayton cycle are shown in Figure 8. The overall cycle efficiency of the system is defined as

$$\eta_{cyc} = {W_{cyc}}/{Q_{2-3}} \tag{1}$$

where W_{cyc} is the useful work defined by the total turbine work minus the work needed to turn the compressor. Q_{2-3} is the energy added to the system inside the combustor and can be defined as the fuel mass flow multiplied by its lower heating value (LHV). The cycle efficiency becomes a function of pressure ratio only when the following assumptions are made:

- All gases are calorically perfect
- The ratio of air flow to fuel flow is large enough to allow the fuel flow to be insignificant
- All components operate on 100% efficiency
- The compression ratio r_p is the same for the compressor and the turbine

In this case, the ideal cycle efficiency can be expressed as follows:

$$\eta_{ideal} = 1 - \frac{1}{r_p^{\frac{\gamma-1}{\gamma}}}$$

(2)

In equation (2), r_p is the pressure ratio, and γ is the ratio of specific heat at constant pressure (c_p) and the specific heat at constant volume (c_v).

In simple cycle gas turbines, neither the compression nor the expansion of the gasses happens isentropically, and the compressor (η_c) and turbine (η_t) efficiencies must be taken into account. The overall cycle efficiency is then given by the following equation:

$$\eta_{cycle} = \left(\frac{\eta_t T_f - \frac{T_{amb} r_p^{\left(\frac{\gamma-1}{\gamma}\right)}}{\eta_c}}{T_f - T_{amb} - T_{amb}\left(\frac{r_p^{\left(\frac{\gamma-1}{\gamma}\right)} - 1}{\eta_c} \right)} \right)\left(1 - \frac{1}{r_p^{\frac{\gamma-1}{\gamma}}} \right)$$

(3)

In equation (3), T_f is the firing temperature and T_{amb} is the ambient temperature. Figure 9 shows the effect of firing temperature (T_f) and the pressure ratio (r_p) on the overall cycle efficiency. From Figure 9 it is clear that at lower firing temperatures, the pressure ratio can decrease the overall cycle efficiency. With new air film cooling techniques and breakthroughs in turbine blade metallurgy, the efficiencies of industrial gas turbines has increased from 15% to 40% over the past 50 years [7].
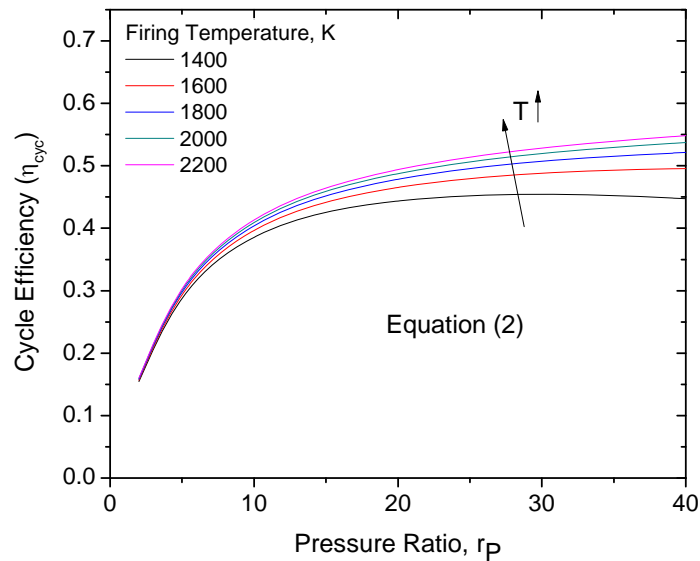
Figure 9. Overall cycle efficiency versus pressure ratio for five different firing temperatures, (equation (2))

The overall efficiency of the system can be greatly increased by utilizing the high enthalpy exhaust gases downstream of the last turbine. When both the gas turbine and a steam turbine are utilized to produce electricity, one speaks of combined cycle mode (CC). There are many different ways to utilize the hot exhaust gases, but in all systems a Heat Recovery Steam Generator (HRSG) is utilized.

An energy flow diagram can be seen in Figure 10 showing the flow of energy as a percentage of the total fuel heat release. Over 21% of the fuel's energy can be "recovered" by the Heat Recovery Steam Generator (HRSG) bringing the overall cycle efficiency up to 60%.

Fuel 100%

GT Output
38%

Exhaust
Energy 61%

ST Output 21%

Condenser 30%
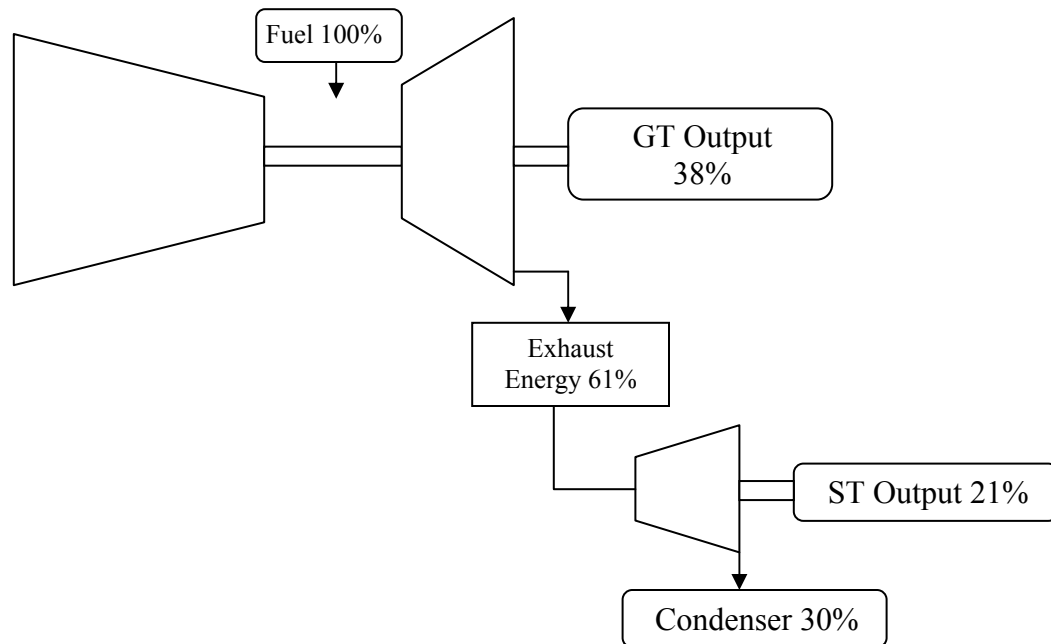
Figure 10. Combined cycle (CC) energy flow diagram

When the exhaust heat is used to produce steam for an additional steam turbine the system is called "combined cycle". When the heat is used to produce steam the process is called "co-generation". Typical modern gas turbines are capable of delivering over 60% and 85% in combined cycle and co-generation mode, respectively. Often, two gas turbines are combined with one steam generator. Figure 11 shows a more detailed image of a combined cycle plant, (source Siemens [8]). A gas turbine is said to be in single cycle mode when operating without exhaust heat recovery system.
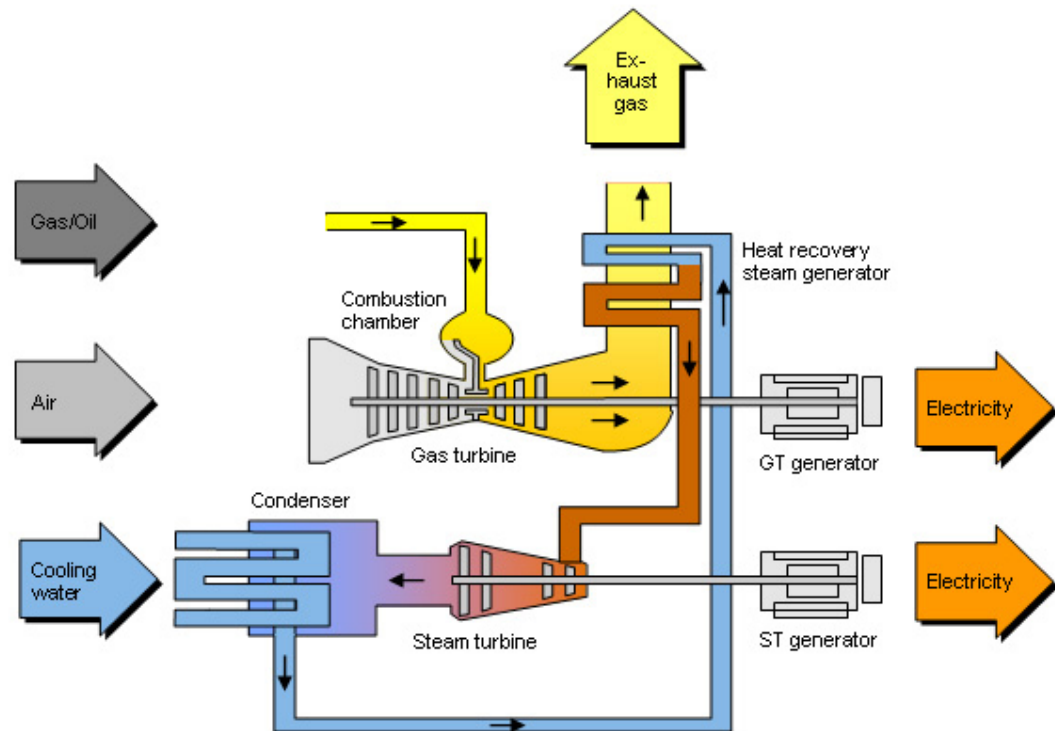
Figure 11 Schematic of combined cycle operation, (source Siemens [8])

Many similarities between industrial and aeroderivative gas turbines exist. Some aeroderivative engines are converted to produce electricity, such as the General Electric LM6000 and the Rolls Royce RB211 (Figure 12 and Figure 13).
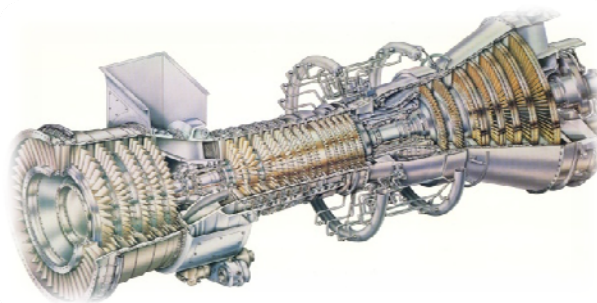
Figure 12. General Electric LM6000 aeroderivative gas turbine (source GE Energy [9])
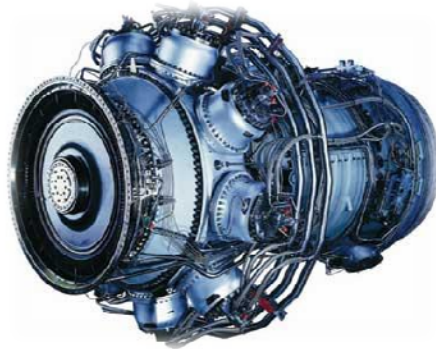
Figure 13. Rolls Royce RB211 aeroderivative gas turbine (source Rolls Royce Energy [9])

Most industrial gas turbines operate at either 3000 or 3600 revolutions per minute (rpm) to match a 50Hz and 60Hz AC power grid, respectively. Advantages of industrial gas turbines are smaller capital investment compared to coal and nuclear plants, short onsite construction times, and short spool up and coast down times. The compactness and low weight make the gas turbine ideal for powering offshore platforms.

One of the main benefits of a gas turbines is its capability to operate on a large variety of fuels such as natural gas, diesel fuel, naphtha, crude, LHV-fuels, and biomass gases/liquids [4]. Combined cycle power plants are replacing the conventional steam power plants due to their high efficiency and low emissions. Steam power plants have efficiencies around 35% versus combined cycle power plant efficiencies, which can be upwards of 60-65%. A summary of capital cost, net efficiency, and construction time is shown in appendix A.

Gas Turbine Combustors

The goal of a combustor is to convert the chemical energy of the fuel into thermal energy. In order to accomplish this goal, the combustor needs to mix the fuel and air entering the combustor, ignite the mixture, and provide a manageable temperature profile at the combustor exit. A typical combustor contains a primary zone, a secondary zone, various wall cooling holes, and a dilution section near the exit. A schematic representation of a gas turbine combustor is shown in Figure 14.
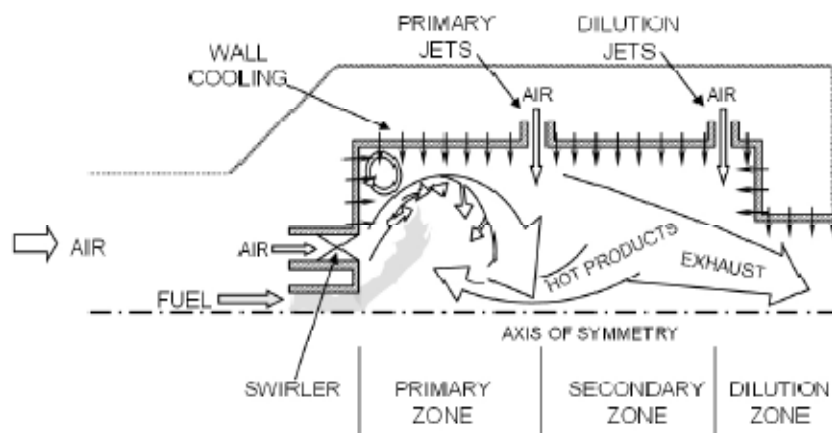
Figure 14. Typical schematic of a gas turbine combustor showing the primary zone, secondary zone, and dilution zone, (source NETL Gas Turbine Handbook section 3.2.1.1 [11])

The primary zone is where the fuel gets mixed with one quarter of the total airflow. Flame stabilization is accomplished through swirler vanes around the fuel nozzle and a primary jet promoting recirculation (Figure 14). Recirculation is critical to promote mixing of the fuel and air and to entrain high temperature products and radicals to ignite the unburned reactants. The secondary zone is needed to accomplish the slower

chemistry which mainly consists of the oxidation of carbon monoxide (CO to CO_2). The role of the dilution zone is to reduce the temperature at the exit of the combustor – creating very lean conditions and oxygen levels around 15%.

The combustion chamber is critical in the gas turbine design and is typically configured in one of three ways:

- Annular

- Can

- Can-Annular

The annular design is a compact design that is often seen in propulsion gas turbines. The air is introduced into the combustor through an annular space that is situated around the turbine shaft. For aeroderivative industrial gas turbines the annular combustor is usually replaced with separate discrete cans for better maintainability.

A can combustor is an individual combustion chamber made out of two separate tubes. The inner tube is called the liner and it is within the liner that the combustion takes place. The liner contains a multitude of holes for cooling air and to introduce secondary air to complete combustion and to cool the combustion products before entering the first stage of turbine inlet guide vanes (IGV). When separate combustion cans are mounted concentrically around the axis the system is called "can-annular". In the can-annular design, the individual tubes are connected via crossover tubes in order to carry the flame from one liner to the other during startup.

Combustor inlet temperatures are highly dependent on the pressure ratio and engine type. Most modern heavy duty industrial gas turbines have a pressure ratio around 17:1.

However, some aeroderivative gas turbines can have pressure ratios up to 40:1 (Rolls Royce industrial Trent 60 DLE). Combustor performance is expressed by its efficiency, which is a measure of the "completeness" of combustion and is defined as [7]

$$\eta_{comb} = \frac{\Delta h_{actual}}{\Delta h_{theoretical}} = \frac{(\dot{m}_a + \dot{m}_f)h_3 - \dot{m}_a h_2}{\dot{m}_f(LHV)} \qquad (4)$$

Equation (4) expresses the ratio of the actual heat increase of the gas divided by the theoretical heat input of the fuel, with $\dot{m}_a$ and $\dot{m}_f$ being the mass flow of the air and fuel, respectively. The inlet and exit gas enthalpies are given by h_2 and h_3, respectively. LHV stands for the lower heating value of the fuel. A major problem of a combustor is its pressure loss, which typically ranges between 2 and 8%. `

Pollutants

Several potential pollutants associated with the combustion process exist and restrictions on emissions combined with increased diversity in fuels create a large design challenge today. Unburned Hydrocarbons (UHC) and Carbon Monoxide (CO) are formed when the combustion process is incomplete and therefore more likely to form under idle or low power settings. CO production is decreased at higher temperatures, which is directly opposite to the formation of NO_x, which increases rapidly at higher firing temperatures. Oxides of nitrogen are the most important non-CO_2 pollutant formed during the combustion process. Both NO_2 and NO are typically formed at a 1 to 9 ratio. The level of a pollutant is calculated as parts per million (ppm) at 15% oxygen. A

schematic representation of NO_x and CO rate of formation as a function of fuel/air equivalence ratio is shown in Figure 15.
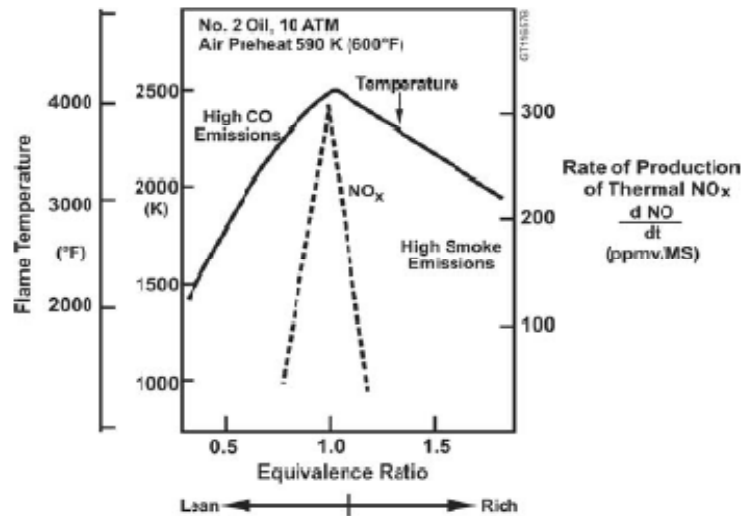
Figure 15. NO_x, CO production rate versus equivalence ratio, (source W.R. bender [12])

The principle causes of oxidation of nitrogen in air are high temperatures and the time allowed for nitrous oxides to form. Therefore, the most common way of reducing NO_x emissions is to reduce the firing temperature inside the combustor.

There are three main mechanisms responsible for the formation of nitrous oxides.

1) *Fuel bound nitrogen*

The nitrogen present in the fuel is converted partly into NO_x

2) *Thermal NO_x*

High temperature reactions between nitrogen and oxygen from the air

$O + N_2 = NO + N$

$N + O_2 = NO + O$

$$N + OH = NO + H$$
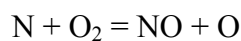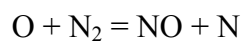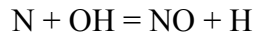
3) *Prompt NO_x*

Nitrous oxide created during the oxidation process of the fuel via $CH + N_2 = HCN + N$ where HCN and N are converted into NO

Opposite to thermal NO_x, prompt NO_x forms under fuel rich conditions at lower temperatures. Thermal NO_x becomes disproportionally more important at temperatures above 1750 K.

Premixed Combustion

Popular techniques available for reducing flame temperatures are steam injection, and premixing the fuel and air mixture before entering the combustor. The premixed combustors, also called Dry Low Emission (DLE) or Dry Low NO_x (DLN) combustors, burn the fuel at cool, fuel lean conditions [12]. A typical DLE combustor used for the Rolls Royce RB211 is shown Figure 16. By limiting the maximum flame temperature to 1725 K, single digit NO_x emission levels can be achieved. The use of premixed combustion comes with a new set of challenges.

Some of the common problems experienced with premixed combustion are:

- Auto-ignition

- Flash-back

- Blow-off

- Dynamic Instability
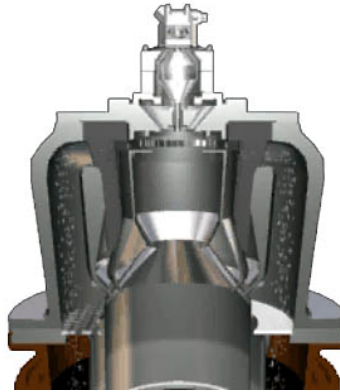
Figure 16. Rolls Royce RB211 combustion system (source Rolls Royce Energy [10])

Auto-ignition

Auto-ignition is a spontaneous ignition of a combustible mixture similar to engine knock in reciprocating engines. When a premixed combination of fuel and oxidizer is left at a sufficiently high temperature and pressure the mixture has the potential to self ignite with potential hazardous or damaging effects resulting in engine shut downs and decrease in availability and reliability [13]. Auto-ignition can be measured using a shock tube currently present at the Texas A&M Turbomachinery laboratory. A picture of the shock tube currently located at Texas A&M Turbomachinery laboratory can be seen in Figure 17.

**Figure 17. Shock-tube facility at Texas A&M Turbomachinery
Laboratory, design and construction by C.J. Aul and J. de Vries**

An extensive shock tube study of auto-ignition characteristics of natural-gas based fuel blends is presented by Petersen et al. [14], Bourque et al. [15], and de Vries and Petersen [16]. A shock-tube pressure trace is shown in Figure 18.
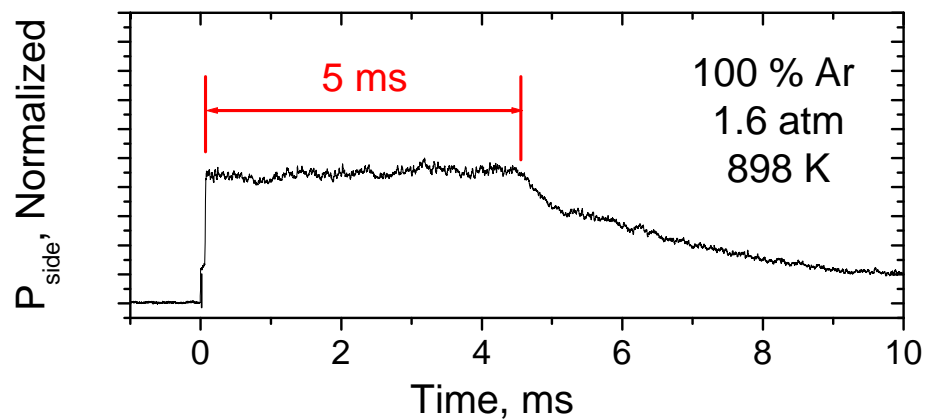
Figure 18. Pressure trace from shock tube

Sims et al. used a test rig with a general premix duct at GT conditions to predict auto-ignition of several gaseous and liquid fuels [12].

To avoid auto-ignition, the residence time must be kept to a minimum. Therefore, a careful balance must be found between auto-ignition and the minimum time required for proper mixing.

Flash-back

When the flame speed of the premixed fuel-air mixture exceeds the flow velocity at the duct's exit, the flame can travel upstream into the premixer duct. Flash-back is often the result of sudden changes in airflow such as an engine surge. Flash-back can be prevented

by using advanced cooling techniques or fast acting shutoff valves triggered by downstream flame detectors [17]. Evidently, proper knowledge of the flame speed of different fuels at different fuel-air ratios is relevant for the prediction of flash back properties.

Blow-off

For most GT combustors, flame speeds of the fuel-air mixtures are significantly lower than the flow velocities. Therefore, in order to stabilize the flame, a recirculation zone must be created to introduce hot products into the fresh reactants. A flame can only be stabilized over a certain range of aerodynamic and thermodynamic conditions. When these conditions are not met, the flame will eventually fail to remain anchored and blow off. Blow-off is a form of static stability and can be predicted via empirical phenomenological methods [17] and [18]. The most common method is to evaluate the ratio of residence time over chemical time τ_{res}/τ_{chem}. The chemical time represents the time required for the reaction to take place and the residence time is the time a mixture spends at a particular location. The resulting ratio is called the Damköhler number.

$$Da = \frac{\tau_{res}}{\tau_{chem}} = \frac{S_L^2 d}{\alpha U_{ref}} \tag{5}$$

U_{ref} and d represent velocity scale and length scale, respectively. α represents the thermal diffusivity, and S_L is the laminar flame speed. From Eqn. (5), it is clear that the

estimation of the flame speed is integral to the determination of static stability. A Damköhler number greater than one represents susceptibility to blow-off.

Dynamic Instability

Dynamic instabilities are complicated couplings between acoustic disturbances and heat release oscillations [17]. An excellent review on the topic of combustion instabilities is presented by Lieuwen and Yang [18].

Generally, combustion instabilities occur at frequencies that are combustor specific, depending on their acoustic modes. Universal prediction of instabilities is therefore complicated. The only way acoustic instability can happen is when the heat release from the oscillating combustion process exceeds the capability of the combustor to dissipate acoustic disturbances. Again, the flame speed is important to predict the flame location; faster flame speed allows the flame to anchor further upstream [17].

Obviously, the measurements of laminar flame speeds are of fundamental importance to combustor design. With the increase in premixed DLE/DLN systems and potential fuels on the market, there has been a strong increase in demand for reliable experimental data at gas-turbine conditions. Currently, Texas A&M's Turbomachinery Laboratory is capable of measuring auto-ignition times and laminar flame speeds at elevated pressures and temperatures. Additionally, an aerosol shock-tube will be capable of studying the combustion behavior of lower vapor pressure fuels. A short summary of candidate gas-turbine fuels and their major properties is given next.

Potential Fuels and Fuel Flexibility

Fuel flexibility is one of the major advantages of gas turbine engines and successful GT operation is demonstrated burning fuels ranging from low BTU coal gas to heavy distillates like #2 distillate oil [4]. Some properties of common liquid fuels are presented in Appendix B. In this study the main focus will be on gaseous fuels, with the primary focus on natural-gas fuels. However, the current experimental setup used in this study will be capable of studying all gaseous fuels and lower vapor pressure fuels when small modifications are made. Gaseous fuels traditionally include natural gas, process gas, low-BTU coal gas, and vaporized fuel oil gas providing up to 60% of the total industrial GT fuel consumption [4]. The main issue with lower heating value gases is the change is mass flows required to maintain performance. Low-BTU gases require more primary combustion air leaving less available for liner cooling.
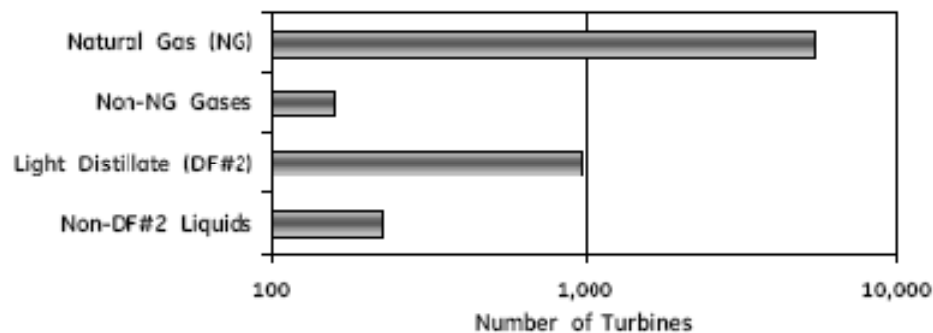
Figure 19. Number of GE gas turbines by fuel type, (source Campbell et al. [4])

Figure 19 shows the number of General Electric units currently in operation per fuel group. The variation in energy content, fuel reactivity and other combustion properties

produce challenges to the combustion designer. The most common gases available today are Natural Gas (NG), Liquefied Petroleum Gas (LPG), Gasified coal (IGCC), refinery offgas, blast furnace gas, and coke oven gas. Table 2 shows these gases and their respective range of Lower heating Values (LHV).

Table 2. Typical gas turbine gaseous fuels, (source Campbell et al. [4])

	Primary Constituents	LHV, MJ/Nm3		U/L Flamability Ratio (289K, 101 kPa)	
		Min	Max	Min	Max
Natutral Gas	CH4, C2H6	29.8	44.7	2.2	3.0
LPG	C3H8, C4H10	85.7	119.2	4.0	5.0
Air Blown IGCC	H2, CO, N2, H2O, CO2	4.8	7.5	2.4	5.4
Oxygen Blown IGCC	H2, CO, H2O, CO2	7.5	14.9	6.0	12.0
Refinery Offgas	H2, C2H6, C3H8, C4H10, C2H4, C3H6	11.2	59.6	3.0	18.0
Blast Furnace Gas	H2, CO, N2, H2O, CO2	2.8	4.7	1.5	3.0
Coke Oven Gas	H2, CO, N2, H2O, CO2	11.2	18.6	6.0	8.0

Natural Gas

Natural gas is still the most common fuel for industrial gas turbines as can be seen in Figure 19. However, the specific make-up of natural gas has been susceptible to variability by geographical location and due to increased importation of Liquefied Natural Gas (LNG) [16]. This variation poses greater challenges with increased risk of auto-ignition, flash-back, blow-off, dynamic stability, and emissions, particularly for premixed DLE combustors [5].

Table 3 shows the compositional range by volume of the constituents of natural gas. Methane levels as low as 85 percent exist with ethane and propane being the major secondary alkanes.

Table 3. Compositional range for typical natural gases (Source Campbell et al. [4])

Constituent	Min %	Max %
Nitrogen (N2)	0	0.4
Carbon Dioxide (CO2)	0	0.7
Methane (C1)	85	96
Ethane (C2)	3	13
Propane (C3)	0	4
Iso-Butnane (IC4)	0	0.9
n-Butane (NC4)	0	0.9
Iso-Pentane (IC5)	0	0.1
n-Pentane (nC5)	0	0
LHV (BTU/scf)	1045	1170

Refinery Off-gas

Refinery off-gases are composed of a combination of higher order hydrocarbons ($C_2H_x - C_6H_x$) and hydrogen (H_2). The increased reactivity of these gases makes them more susceptible to flash-back, auto-ignition, and emissions problems.

Blast Furnace Gas

Blast furnace gas (35% CO, 2-3% H_2, inert) is the product of steel production and has very low energy content. The increased mass flow necessary to maintain stable operation usually requires modification to the combustor.

LNG Field Gas

Liquefied-Natural-Gas (LNG) Field gases typically contain high levels of ethane and nitrogen since removal of these gases from Liquefied Natural Gas (LNG) is necessary

before transport. Therefore, the gases pose similar challenges as seen with refinery off gas in the high ethane case. High nitrogen content can lead to decreased flame temperature and thus increased CO emission. High N_2 can also lead to static stability issues reducing the margin to lean blow out.

Syngas-

Coal derived syngas used in Integrated Combined Cycle (IGCC) power plants is one of the most promising fuels today. The high overall cycle efficiency, the capability of pre-combustion carbon capture, and the relative abundance of coal in the U.S. have led to several DOE programs sponsoring the development and exploration of syngas-fueled power plants. Examples are the GE/DOE High Hydrogen Turbine Program (HHTP) [19] and the Fossil Energy (FE) Advanced Turbine Program. These programs are intended to provide technological solutions to high level DOE goals, such as the Climate Change Initiative, the Clear Skies Initiative, the Hydrogen Initiative, and the FutureGen Initiative. The FutureGen Initiative can be described as an effort to:

"...validate the technical feasibility and the economic viability of "zero" emission energy from coal. By 2012, begin operation of a nominal 275-megawatt (MW) prototype plant that will produce electricity and hydrogen with "zero" emissions; and prove the effectiveness, safety, and performance of CO2 sequestration [20]"

The combustion of syngas remains a major issue due to its high hydrogen content. Most of the tactics for reducing NO_x emissions have tightened the safe operating regime

due to increased risk to auto-ignition and static or dynamic instability. Premixed combustion techniques used for NO$_x$ reduction in conventional natural-gas fired gas turbines can often not be applied to high-hydrogen fuels. As a fuel, hydrogen behaves very differently than natural gas due to its higher specific heat, diffusivity, flammability limits, and flame speed. Additionally, different gasification processes lead to very different gas compositions as can be seen in Table 4 [21]. The non-linear behavior of hydrogen in terms of auto-ignition warrants further study. Recently, much focus has been on the effect of hydrogen on gas-turbine combustion systems. Experiments vary from single combustor/burner rigs in a laboratory setting as done by Daniele et al. [22] and Singh et al. [19] to full scale in field testing.

Table 4 Syngas compositions, (source Mcdonell [21])

Constituents	PSI	Tampa	El Dorado	Pernis	Sierra Pacific	ILVA	Schwarze Pumpe	Sarlux	Fife	Exxon Singapore	Motiva Delaware	PIEMSA	Tonghua
H2	24.8	37.2	35.4	34.4	14.5	8.6	61.9	22.7	34.4	44.5	32	42.3	10.3
CO	39.5	46.6	45.0	35.1	23.6	26.2	26.2	30.6	55.4	35.4	49.5	47.77	22.3
CH4	1.5	0.1	0.0	0.3	1.3	8.2	6.9	0.2	5.1	0.5	0.1	0.08	3.8
CO2	9.3	13.3	17.1	30.0	5.6	14.0	2.8	5.6	1.6	17.9	15.8	8.01	14.5
N2+AR	2.3	2.5	2.1	0.2	49.3	42.5	1.8	1.1	3.1	1.4	2.15	2.05	48.2
H2O	22.7	0.3	0.4	---	5.7	---	---	39.8	---	0.1	0.44	0.15	0.9
LHV													
BTU/ft^3	209	253	242	210	128	183	317	163	319	241	248	270.4	134.6
kJ/m^3	8224	9962	9528	8274	5024	7191	12492	6403	12568	9477	9768	10655	5304
Tfuel , F	570	700	250	200	1000	400	100	392	100	350	570	338	---
Tfuel , C	300	371	121	96	538	204	38	200	38	177	299	170	---
H2/CO	0.63	0.8	0.79	0.98	0.61	0.33	2.36	0.74	0.62	1.26	0.65	0.89	0.46
Diluent	steam	N2	N2/steam	steam	steam	---	steam	moisture	H2O	steam	H2O/N	N2	n/a
Equivalent LHV													
BTU/ft^3	150	118	113*	198	110	---	200	---	*	116	150	129	134.6
kJ/m^3	5910	4649	4452	7801	4334	---	7880	---	---	4600	5910	5083	5304

Currently, IGCC plants with GE gas turbines total more than 2300 MW and Siemens is currently working on offering complete IGCC power plants.

From the diversity of fuels listed above, one can conclude that there is an increased demand for reliable data during the combustor design process. Experiments provide fundamental inputs to empirical models, as well as validation to full chemical kinetics mechanisms. Currently, Texas A&M's Turbomachinery Laboratory is capable of testing both gaseous and liquid fuels under gas-turbine relevant thermodynamic conditions. This dissertation focuses on the flame speeds of natural gas based fuels. However, the current facility can be used in the future to study syngas and LHV-fuels.

1.3   Perspective

The changing energy situation in the world and the U.S. has caused an increased interest in a wider variety of potential fuels. For example, for land-based gas turbines this has meant that gases that used to be flared off are now considered potential fuels. New technologies in coal gasification along with combined cycle power plants (IGCC) have further widened the list to include high-hydrogen fuels. Gas-turbine combustors do not always respond favorably to fuel flexibility, showing an increased risk for auto-ignition, flashback, blow off, dynamic instability, and emissions. Proper knowledge of the combustion characteristics of these different fuels is fundamental in predicting robustness against some of these aforementioned risks.

Laminar flame speeds form a fundamental and unique combustion property of a fuel, indicating its reactivity and exothermicity [23], [24]. Laminar flames have added complexity when compared to zero-dimensional ignition data, due to the importance of the fuel's transport properties (conductivity, diffusivity, viscosity). However, the geometry specific complexity of turbulence is not incorporated in a premixed laminar

flame, allowing 1-D laminar flames to be modeled with full scale chemical mechanisms included. For these reasons, laminar flame speed data can be used in empirical formulations predicting turbulent flame speed, flash back, and blow off. Additionally, flame speed data are used to validate full scale chemical kinetics models with potentially thousands of reactions.

A new experimental apparatus was built at Texas A&M's Turbomachinery Laboratory capable of measuring premixed laminar flames at pressure up to 15 atm. This dissertation describes the design philosophy, experimental techniques, data processing, modeling, and analysis of high-pressure methane flames doped with ethane and propane. The fuels are important for the gas turbine community where higher levels of mainly ethane and propane have become more common recently.

There are many techniques available for measuring a laminar premixed flame. Some of these are summarized in the next chapter. Also, an extensive background on similar studies performed in the past by other researchers is included. This background shows that reliable, high-pressure flame speed data are scarce.

CHAPTER II

BACKGROUND

2.1   Laminar Premixed Flames

A laminar premixed flame LPF can be defined as a "self sustaining propagation of a localized combustion zone at subsonic velocity" [23]. The flame is localized because it only takes a small, finite region in space, dividing unburned reactants and burned combustion products. Laminar flames are subsonic and therefore distinctly different from detonations which are self sustained supersonic combustion waves. A subsonically moving flame is also called a deflagration. Some confusion exists between the term "burning velocity", "flame speed", "deflagration velocity", "wave speed", and "propagation velocity" [25]. In this study, these terms will be used interchangeably and all refer to the velocities with respect to the gas ahead of the wave [25].

Full understanding of premixed flames requires prior knowledge of heat and mass transfer, chemical kinetics, and thermodynamics. In general, understanding laminar flames is a prerequisite for understanding turbulent flames. LPF's are also important in order to predict flame extinction and ignition behavior. Lastly, the measurements of LPF's serve as fundamental target data for the development of chemical kinetics mechanisms.

When a flame is freely propagating, it can be used as the reference frame and, relative to the flame, the unburned reactants would approach the flame with a velocity of $S_{L,u}^0$. In this dissertation, the subscript L stands for laminar, u refers to the unburned

mixture, and the superscript *0* relates to the fact that the flame is not subjected to stretch effects. Effects of flame stretch on flame speed will be covered in later chapters. Logically, combusted gases leave the flame with a velocity $S_{L,b}^0$, where the subscript *b* refers to the burned state of the gas. An ideal presentation of a flame front is shown Figure 20.

Flame

Unburned Gases

$S_{L,u}^0$

Pressure = P_u

Density = ρ_u

Temperature = T_u

Burned Gases

Pressure = P_b

Density = ρ_b

Temperature = T_b

$S_{L,b}^0$
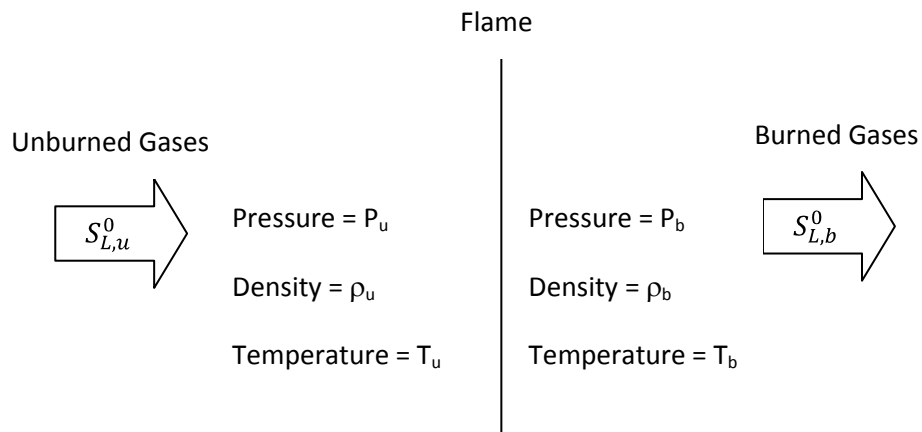
Figure 20. Flame sheet dividing unburned reactants from the burned products

Since the flame travels subsonically, the pressures P_u and P_b must be equal. The flame area is constant, and the density decreases from ρ_u to ρ_b across the flame. Therefore, burned and unburned flame speed can be related via the continuity equation.

$$S_{L,u}^0 A \rho_u = S_{L,b}^0 A \rho_b \tag{6}$$

$$\frac{S_{L,b}^0}{S_{L,u}^0} = \frac{\rho_u}{\rho_b} = \sigma \tag{7}$$

Were ρ_u and ρ_b are the unburned and burned densities, respectively. The ratio of the two

densities is expressed by σ.

A flame can be divided into two zones, the preheat zone and the reaction zone. In the preheat zone, little or no heat release takes place and much of the temperature increase is caused through diffusive heat transfer from the reaction zone. Most of the chemical energy is released in the reaction zone. A modeled flame structure of methane and air is shown in Figure 21.
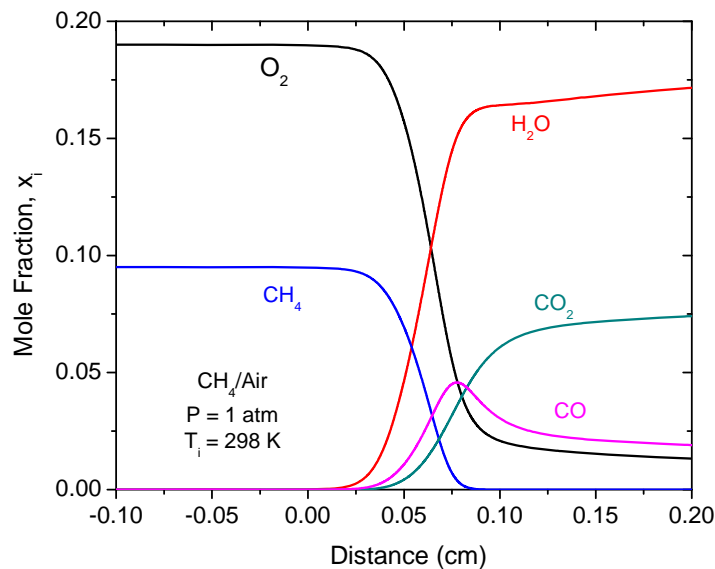
Figure 21. Mole fraction of CH$_4$, O$_2$, H$_2$O, CO$_2$, and CO across an atmospheric methane/air flame modeled using GRI 3.0 [26]

For the flame to be self sustaining, there must be a high gradient of temperature and species concentration, which means that the spatial distance, the flame

thickness, must be small. Typical flame thicknesses are on the order of a millimeter and decrease with increasing pressure.

Figure 21 shows that the formation of CO_2 from CO is comparatively slow and happens at the trailing edge of the reaction zone. This slow reactivity of CO is particularly important in a gas-turbine combustor design, where failing to allow for this reaction to take place increases CO emission and reduces the combustor efficiency.

Governing Equations

The assumption that the pressure remains constant across the flame greatly reduces the complexity of the problem since the momentum equation no longer needs to be considered. The governing equations then reduce to the continuity equation, the species conservation equation, and the energy equation. The main equations and their meaning will be presented here for steady, one-dimensional flow. More details on the species specific transport, thermodynamic, and kinetic parameters are given in Chapter IV. Some theory concerning instabilities, cellular flames, and flame stretch interactions is including here in this chapter. A more rigorous analysis on flame theory can be found in references [23]-[27].

Continuity

Since nuclear reactions are not considered here, mass can neither be created nor destroyed. The continuity equation for steady flow then becomes

$$\frac{d\dot{m}''}{dx} = 0 \tag{8}$$

Which, for one-dimensional flow becomes

$$\frac{d(\rho v_x)}{dx} = 0 \tag{9}$$

Species Conservation

The species equation is more complex because it incorporates the transport of species due to bulk transport, molecular diffusion, and includes volumetric species creation due to chemical reactions. The scalar relationship in multiple dimensions can be written as:

$$\frac{\partial(\rho Y_i)}{\partial t} + \mathbf{\nabla} \cdot [\rho Y_i(\mathbf{V} + \mathbf{v}_{i,\text{diff}})] = \dot{m}_i''' \tag{10}$$

Where Y_i is the mass fraction, ρ is the density of the mixtures, $\mathbf{V}$ is the bulk velocity, and $\mathbf{v}_{i,\text{diff}}$ is the diffusional velocity. The subscript i refers to the individual species. For one-dimensional steady flow, equation (10) becomes

$$\dot{m}_i'' \frac{dY_i}{dx} + \frac{d}{dx}(\rho Y_i v_{i,\text{diff}}) = \dot{\omega}_i \bar{M}_i \tag{11}$$

Where $\dot{\omega}_i$ is the species molar production rate and $\overline{M}_i$ is the molecular mass.

Energy Conservation

The energy equation is composed of energy due to chemical reactions, conduction at the boundaries, molecular diffusion, and bulk motion.

$$\dot{m}_i'' c_p \frac{dT}{dx} + \frac{d}{dx}\left(-k\frac{dT}{dx}\right) + \sum_{i=1}^{N}(\rho Y_i v_{i,\text{diff}} c_{p,i}) = \sum_{i=1}^{N} h_i \dot{\omega}_i \overline{M}_i \qquad (12)$$

In addition to these three equations, the boundary conditions can be set as the initial condition (T_i, Y_i's) at x = -∞, and the fact that all gradients become 0 as x = +∞.

A More detailed description of the transport properties of gases is presented in Chapter IV.

Temperature and Pressure Dependency

Conditions inside a gas-turbine combustor vary with fuel, compression ratio, and specific application. Therefore, it is important to understand the flame's response to increases in temperature and pressure. Simplified analysis of flame speed and thickness as a function of temperature and pressure is presented by Turns [23]. The result from this analysis is presented here and later compared to experimental findings by others, including results from this study. The flame speed's proportionality to pressure and temperature is given as follows:

$$S_L^0 \propto \overline{T}^{0.375} T_u T_b^{-n/2} exp\left(\frac{-E_A}{2R_u T}\right) P^{(n-2)/2}$$

(13)

where T_u and T_b are the unburned and burned gas temperatures, respectively. E_A is the overall activation energy, R_u is the universal gas constant (8.314 kJ/kgK), P is the pressure, and n represents the overall reaction order. The overall reaction order, n is approximately 2. Several methods for obtaining the overall activation energy exist. For instance, the activation energy of ethane, obtained using the shock-tube method, was found to be 40 kcal/mol [28]. For methane, the activation energy was found to be as high as 52.3 kcal/mol at one atmosphere, [29] and as low as 19 kcal/mol at pressures above 40 atm and temperatures below 1300 K [29], [30]. The relative effect of unburned temperature on the flame speed (equation 8) is shown in Figure 22.
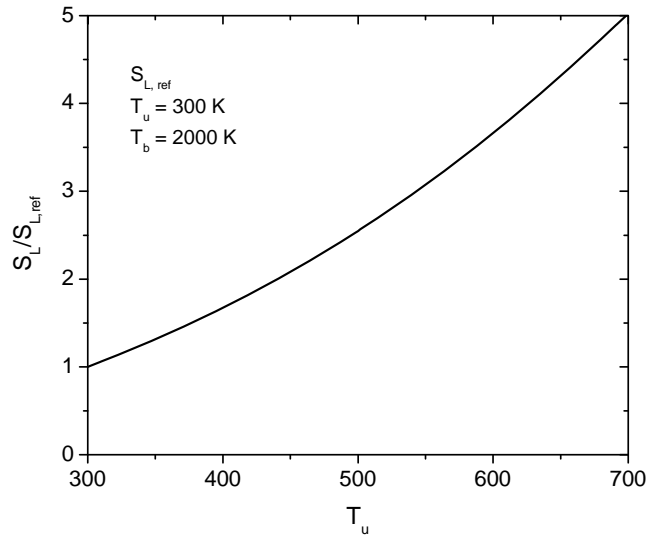
Figure 22. Relative flame speed versus unburned gas temperature normalized by the reference flame speed at $T_u = 300$

Figure 22 shows that there is a strong dependency of the flame speed on the temperature of the unburned reactants. The effect of pressure on the temperature profile across a flame is shown in Figure 23. The temperature rise takes place over a smaller spatial distance. This means that the flame thickness decreases with increasing pressure. Flame speeds decrease with pressure, and the pressure dependency of the mixtures used in this study is presented in Chapter VI. There are many experimental methods to find the premixed laminar flame speed, and a summary of these different techniques is presented here.
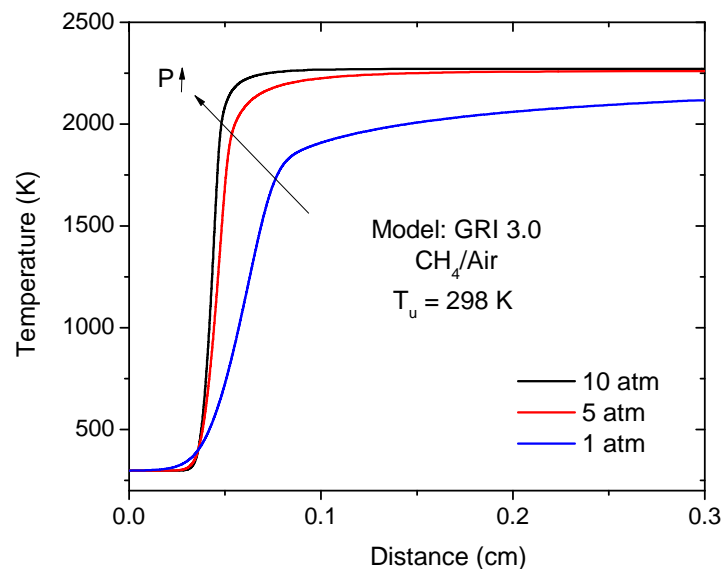
Figure 23. Modeled temperature profiles across a stoichiometric methane flame at 1, 5, and 10 atm

(model GRI 3.0 [26])

2.2   Measurement Techniques for Laminar Premixed Flames

Many studies on laminar premixed flames exist. The study of non-premixed diffusion flames will not be covered in this study. Several methods to obtain the premixed laminar flame velocity are available, and a summary of these methods is given.

Bunsen Flame

Of all experimental techniques available, the Bunsen-burner flame, named after the German chemist Robert Wilhelm Bunsen, is probably the least complex and can easily be used in classroom situations. In the ideal case, the fuel and air get premixed and burn above the exit nozzle in a conical fashion. The flame shape is caused by the combined effect of heat loss at the wall and the exit velocity profile as shown in Figure 24. Per definition, the localized flame speed is equal to the normal vector component of the unburned gas as shown Figure 24. Obtaining the flame speed from a Bunsen burner is complicated due to the flame curvature and the flame thickness [24]. Alternatively, the flame speed can be obtained by dividing the mass flow through the tube by the unburned gas density and the flame area, thereby assuming that the flame speed, s_u is constant across the flame, such that

$$S_{L,u} = \frac{\dot{m}}{\rho_u A_f} \tag{14}$$

In equation (14), $S_{L,u}$ is the laminar flame speed, $\dot{m}$ is the mass flow through the burner, and A_f is the total flame surface area.

Figure 24. Bunsen flame, flame speed equal to $v_u \sin \alpha$

The superscript 0 is omitted in equation (14) due to the fact that a Bunsen flame is prone to curvature and flame stretch effects making it different from an adiabatic planar flame speed designated as $S^0_{L,u}$. In this dissertation nomenclature used by C.K. Law is adapted.

Flat Flame

Some of the difficulties of obtaining the flame front with Bunsen flames can be overcome by creating a uniform flow at the exit. This can be accomplished by sending the gases through an array of screens and beads. Flat flame burners stabilize a planar flame above or between two porous plates. In this configuration, the flow becomes nearly one dimensional. The major drawback of this technique is the heat transfer to the

walls, which makes the measured flame speed appear lower and must be corrected for [25]. In some instances, the heat flux is measured and used to determine the flame speed. Measuring high-pressure, laminar flame speeds using the flat-flame method is complicated by the fact that the experimental apparatus needs to be confined within an enclosure. Additionally, elevated pressures increase the Reynolds number in the mixing tube upstream of the burner plate causing the flow to become turbulent above about (Re = 2300). Variants of the flat flame burner are stagnation flames where the flow is directed towards a solid flat plate, or an opposing flow of inert gas.

Heat Flux Method

Bosschaart and de Goey used the heat flux method to obtain the laminar burning velocity of hydrocarbon and air mixtures [31]. In their method, a thin perforated plate was used to stabilize the flame keeping the edge of the burner at a relatively high temperature. The parabolic temperature profile was measured using thin thermocouples, and the laminar burning velocity of methane/air was found to be around 36 cm/s. The laminar burning velocity of ethane was found by Konnov et al, using a similar technique [32]. Konnov found the flame speed of stoichiometric, atmospheric flame speed to be around 41 cm/s.

Problems with stationary flames are caused by upstream flow nonuniformities, flame curvature, and heat transfer effects. These issues can be avoided by allowing the flame to freely expand into a reactants filled domain.

Spherically Expanding Flames

The Bunsen, flat flame, and the heat flux method fix the flame to the laboratory coordinates, requiring gas flow measurements for the flame speed. Alternatively, a mixture of fuel and oxidizer can be ignited within an enclosure creating a freely propagating, spherically expanding laminar flame, schematically shown in Figure 25.
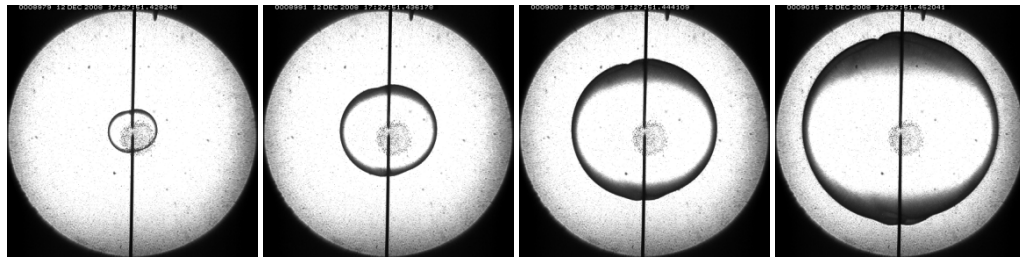
Figure 25. Spherically expanding flame (images from this study)

Two major philosophies exist on obtaining the burning velocity from spherical expanding flames inside an enclosure. The first method uses the pressure rise during the combustion event to determine the mass fraction burned, which can be related to the radius of the flame via a thermo-chemical balance. These experiments require the pressure and temperature of the unburned gases surrounding the flame to uniformly increase. Many models have been proposed to convert the pressure rise into a burning velocity.

When the flame radius is small compared to the radius of the enclosure, the pressure and temperature ahead of the flame can be considered constant. This means that the

flame radius must be obtained via some optical method. When the radius-time history is obtained, the flame speed can be obtained by

$$\frac{dR_f}{dt} = S_{L,b} \tag{15}$$

Since the combustion products in the center are stationary, the obtained flame speed must be that of the burned gases, i.e. $S_{L,b}$. The unburned burning velocity can then be obtained by dividing equation (15) by the density ratio across the flame so that

$$S_{L,u} = \frac{\rho_b}{\rho_u} S_{L,b} \tag{16}$$

Measurements of spherically expanding flames with the constant "bomb" method are comparatively simple in design and consume less gas than constant flow burners. Some of the complexities with this method include: heat loss through electrodes, buoyancy effects, cellular instabilities, and radiative heat loss from the flame [24]. Obtaining flame radius histories with a high speed camera requires the flame speed vessel to be equipped with optical access. These windows must withstand the high post combustion temperatures and pressures. In this study, data are obtained using a constant-volume cylindrical bomb with large optical access on each side.

2.3 Prior Work with Spherically Expanding Flames

Premixed, centrally ignited, spherically expanding flames have long been recognized as a valuable experimental technique.

Table 5. List of work using spherically expanding flames

Optical Access	Primary Investigator	Location/University	Year	P_i(Mpa)*	Ti(K)	Ref.
No	Manton et al.	Bureau of Mines, Pittsburgh	1953	0.1	300	[33]
No	Smith et al.	Purdue University	1956	2	300	[34]
Yes	Agrawal	Government Engineering College, Ujjain, India	1981	0.4	300	[35]
Yes	Groff et al.	General Motors Research Laboratories / University of Michigan	1982	0.5	300	[36]
No	Gulder	National Research Council, Canada	1982	0.8	500	[37]
No	Iijima et al.	Tokai University/The University of Tokyo, Japan	1986	3	500	[38]
Yes	Aung et al.	The University of Michigan	1997	0.3	300	[39]
yes	Bradley et al.	University of Leeds	1998	1	600	[40]
No	Elia et al.	Northeastern University	2001	4.3	300	[41]
No	Radwan et al.	Helwan University, Egypt Cairo University, Egypt	2001	0.1	400	[42]
Yes	N. Djebaili-Chaumeix	Laboratoire de Combustion et Systemes Reactifs,	2003	0.5	300	[43]
No	Saeed et al.	Oxford University, UK	2004	0.3	423	[44]
No	Dahoe	University of Ulster, UK	2005	0.1	293	[45]
Yes	Ilbas et al.	Cardiff University UK	2005	0.1	300	[46]
Yes	Johnston et al.	Engineering	2005	0.3	450	[47]
Both	Takizawa et al.	AIST Japan	2005	0.1	300	[48]
Yes	Kitagawi	Kyushu University, Japan	2005	0.5	298	[49]
Yes	Huang et al.	People's Republic of China	2006	0.1	300	[50]

* When absolute pressure rating of chamber is given it will be divided by 10 to roughly give the allowed pre-combustion pressure.

A list of prior work using spherically expanding flames is shown in Table 5, including the pressure and temperature range per facility.

Spherical expanding flame speed measurements can be divided into the classical method and the optical method. The classical method uses the pressure-time history in combination with an energy balance to measure the propagation of the flame [33]. This windowless design allows for high initial pressure experiments (P_i > 40 bar) as shown by Elia et al. [41]. However, the exclusion of direct flame-front visualization inhibits the ability to measure stretch intensity, flame-shape deformation, cellular instabilities, and buoyancy effects. Also, transient temperature and pressure behavior of the unburned gas further complicate the data analysis and its accuracy [51].

Classical Method

In 1953, Manton et al. [33] related the laminar flame speed to pressure time histories and reported a laminar flame speed of stoichiometric CH_4/Air mixtures to be approximately 36 cm/s, a value close to that found in this study of 35 cm/s. Smith and Agnew observed laminar flame speeds of stoichiometric CH_4/Air decreasing when the pressure was raised from 1 to 20 atm [34]. The classical method was also used by Gülder [37], Iijima and Takeno [38] using ionization probes, and more recently by Elia et al. [41], Radwan et al. [42], Saeed and Stone [44], and Dahoe [45]

Gülder [37] measured the laminar burning velocity of methanol, ethanol, and isooctane-air mixtures. The variation of burning velocity with initial pressure and temperature was observed to follow an empirical correlation as shown below:

$$S_L = S_{L,r} \left(\frac{T}{T_r}\right)^m \left(\frac{P}{P_r}\right)^n \tag{17}$$

In this equation, $S_{L,r}$, T_r, and P_r are a reference burning velocity, temperature and pressure respectively. Ijima and Takeno [38] measured the burning velocity of methane/air and hydrogen/ air at temperatures up to 500 K using a spherical vessel with an inside diameter of 16 cm. The relationship between burning velocity and pressure history used by Ijima and Takeno [38] is shown in the equation below:

$$S_L = \frac{1}{F(P)} \frac{r_c}{P} \frac{dP}{dt} \tag{18}$$

In this equation, F(P) is a function of the pressure only, r_c is the vessel inside diameter, P is the pressure, and t is the time.

Elia et al. [41] was able to measure laminar burning velocities of methane-air mixtures up to 70 atm and temperatures up to 550 K. Again, a spherical chamber was used with an inside diameter of approximately 15 cm. The pressure histories were converted into burning velocities via a model that takes into account temperature gradients in the burned gases. The results were correlated in a form similar to that shown in equation (17) used by Gülder [37]. In contrast to the work by Ijima and Takeno [38], Elia et al. [41] evaluated the flame stretch effect.

The complexity of using the transient pressure technique resulted in more complicated models as derived by Saeed and Stone [44]. Saeed and Stone [44] used a

novel multi-zone model to study the combustion process inside a closed vessel. The model shows that a temperature difference as large as 500 K between the first and the last burned zone may exist.

Finally, Dahoe [45] measured hydrogen air mixtures using a windowless vessel. Dahoe [45] measured transient pressure profiles and used this information to obtain the burning velocity by matching it to an integral energy balance. The results by Dahoe seem to fall within the experimental scatter of other experiments even when flame stretch effects are not taken into account.

In general, windowless designs allow for higher initial pressures to be measured due to the absence of optical access and the design complexities associated with high pressure windows. However, flames show a larger propensity to become unstable or cellular at elevated pressures. Additionally, without direct observation of the flame movement the flame stretch effects cannot be determined within an acceptable level of uncertainty. Flame shape distortion, flame front cellular instabilities, and buoyancy effects cannot be observed in windowless vessels. Finally, the continuous change in pressure and temperature of the unburned gases impose a significant challenge in the accuracy of data reduction [51]. For these reasons, a flame speed bomb with optical access was used in this study, and the remainder of this chapter will focus on results obtained by other researchers using high-speed cine-photography.

Optical Technique

The optical method using high-speed imaging of flame-front propagation via a rotating drum camera was conducted by Agrawal [35] and Groff [52]. Agrawal confirmed that the burning velocities of methane/air mixtures decrease inversely proportionally with pressure. Groff observed the discrete polyhedral cellular nature of propane-air flames up to 5 atm and related the onset of cellularity by a critical Reynolds number defined as shown below:

$$Re_c = \frac{\rho_u R_{f,c} S_L}{\mu_u} \tag{19}$$

In equation (19), ρ_u is the density of the unburned gas, $R_{f,c}$ is the critical radius at which cells are formed on the flame surface, S_L is the (stretched) burning velocity, and μ_u is the dynamic viscosity of the unburned gas mixture. Manton et al. [53] observed similar effects in spherical expanding flames in 1951. Groff [52] concluded that the cellular flames were caused by hydrodynamic instabilities rather than preferential diffusion. One key observation was that cellular flames can influence the accuracy of burning velocity measurements.

The fact that spherically expanding flames impose flame stretch effects that need to be accounted for was shown by Dowdy et al. [54] and by Aung and coworkers [39], [55]. Dowdy related the stretched and unstretched flame speed for hydrogen air mixtures, where flame stretch is defined as:

$$\alpha = \frac{1}{A_f}\frac{dA_f}{dt} \tag{20}$$

In equation (20), A_f is the spherical flame surface area and t is the time. Since the surface of a sphere is given by $4\pi R_f^2$, equation (20) can be expressed solely as a function of R_f, so that

$$\frac{1}{A_f}\frac{dA_f}{dt} = \frac{1}{4\pi R_f^2}\frac{d4\pi R_f^2}{dt} = \frac{2}{R_f}\frac{dR_f}{dt} \tag{21}$$

Asymptotic analysis and detailed modeling [54] show a linear relationship between stretch and burning velocity in the low stretch regime given as:

$$S_L^0 = S_L + L_m\alpha \tag{22}$$

In equation (22), L_m is the Markstein length relating the burning velocity to flame stretch. S_L^0 is the 1-D laminar planar flame speed used to compare against models and other experimental observations.

Aung et al. [39] measured the flame speed of H_2/air mixtures at pressures up to 4 atm. Flame stretch interaction was correlated in a similar linear fashion as was done by Dowdy et al. [54]. Aung et al. [39] non-dimensionalized the flame stretch and the

Markstein length to form the Karlovitz and Markstein numbers, respectively. The Karlovitz number Ka is defined as:

$$Ka = \frac{\alpha D_u}{S_L^2} \tag{23}$$

In equation (23) α is the flame stretch as defined by equations (20) and (21), S_L is the stretched burning velocity, and D_u is the mass diffusivity. Selecting the proper value for D_u is arbitrary in multicomponent mixtures, and Aung et al. [39] used the binary diffusion of hydrogen with respect to nitrogen. The Markstein number Ma is defined as:

$$Ma = \frac{L_m}{\delta_D} \tag{24}$$

In equation (24), δ_D is the characteristic flame thickness, which is defined as:

$$\delta_D = \frac{D_u}{S_L} \tag{25}$$

Combining equations (23) and (24) with equation (22) allows the effect of preferential-diffusion/stretch interaction to be correlated according to the following equation:

$$\frac{S_L^0}{S_L} = 1 + MaKa \tag{26}$$

For hydrogen/air mixtures, there is a large difference between the mass diffusivity of hydrogen and air. This can result in different behavior for fuel lean and fuel rich mixtures.

Figure 26 shows the mass diffusivities of methane, ethane, propane, and oxygen for pressures up to 10 atm. Oxygen and methane have very similar mass diffusivities, while ethane and propane are less diffusive by almost a factor of two.
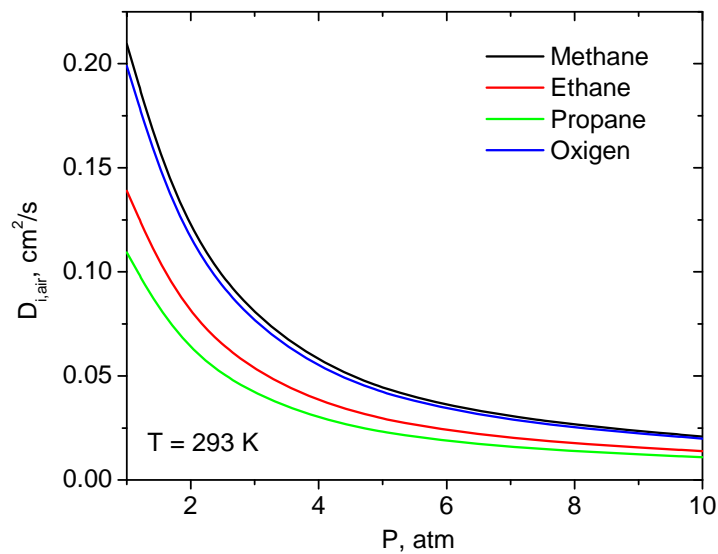
Figure 26. Diffusivities for oxygen and the fuels used in this study versus pressure

Hassan et al. [55] studied methane/air flames up to 4 atmospheres using the same setup as Aung et al. [39]. Hassan et al. [55] showed substantial effect of laminar flame stretch

on burning velocities with values of S_L^0/S_L ranging from 0.6-2.3. Similar to hydrogen/air flames, methane/air flames exhibit unstable preferential-diffusion behavior at fuel lean conditions. These preferential-diffusion instabilities were not observed in this study. Diffusivities of methane and oxygen are nearly equal. Therefore, explaining flame front instabilities through preferential-diffusion mechanisms seem unlikely.

Higher pressure experiments were performed by Bradley et al. [56], (P_i = 10 bar), and by Rozenchan et al. (P_i = 60 bar) [57]. The high initial pressure obtained by Rozenchan et al. [57] was made possible by two concentric cylinders that would allow combustion products from the inner cylinder to expand into an inert-filled outer cylinder. A schematic of the setup used by Rozenchan et al. [57] can be found in Figure 27
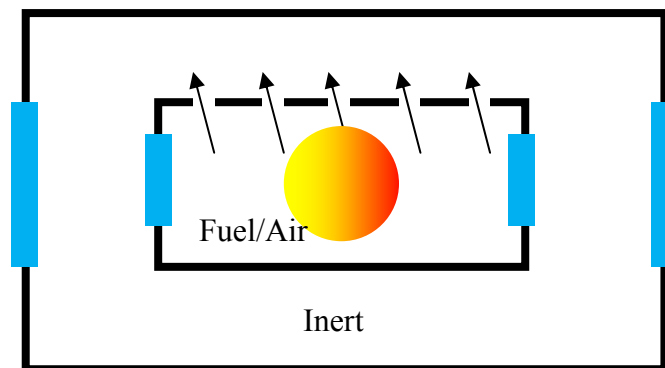
**Figure 27. Double cylinder as used by Rozenchan et al. [49]
and Tse et al. [35]**

Rozenchan et al. [57] showed that stable flame fronts at high pressures could be achieved when lower O_2 levels or different bath gases such as helium were used.

This study focuses on methane, ethane, and propane mixtures at elevated pressures. A list of previous work by other researchers with these fuels is shown in Table 6, 7, and 8, including the experimental range in terms of pressure and temperature.

Table 6. Overview of methane burning velocity measurements

Researcher	Reference	Year	Technique	SL	P, atm	T, K
Clingman	[58]	1953	Burner	39.7	1	298
Edmondson	[59]	1969	Nozzle Burner	37.0	1	298
Edmondson	[60]	1970	Flat Flame	35.7	1	298
Andrews	[61]	1972	Windowless Bomb	42.6	1	298
Gunter	[62]	1972	Flat Flame	41.5	1	293
Wu	[63]	1984	Bunsen/Stagnation flame	39.2	1	298
Iijima	[64]	1986	Windowless Bomb	34.9	0.5-30	291-500
Kawakami	[65]	1988	Closed Bomb/Zero Gravity	34.5	1	298
Egolfopoulos	[66]	1990	Counterflow	40.0	0.5-2	298
van Maaren	[67]	1994	Flat flame/heat flux	37.0	1	298
Clarke	[68]	1995	Windowless Vessel	36.8	1	298
Vagelopoulos	[69]	1998	Counterflow	36.7	1	298
Hassan	[55]	1998	Windowed Vessel	34.9	1-4	298
Gu	[70]	2000	Windowed Vessel	36.8	1-10	300-400
Rozenchan	[57]	2002	Windowed Vessel	36.0	1-20	298
Boschaart	[71]	2004	Heat flux	35.7	1	298

Table 6 shows an overview of methane burning velocity measurements. Measured methane burning velocities vary from 34.5 to 42.6 cm/s at stoichiometric conditions, a difference of more than 23%. Also, few studies were conducted at engine-relevant conditions; Gu et al. 0 and Rozenchan et al. [57] have measured methane/air flames above 5 atm.

Ethane flame experiments are less common as can be seen in Table 7, where the highest pressure showing is 2 atm. In addition, the author was not able to find spherical expanding flames measurements with ethane air mixtures.

Table 7. Overview of ethane flame speed experiments

Researcher	Reference	Year	Technique	SL	P, atm	T, K
Egolfopoulos	[66]	1990	Counterflow	42.5	0.5-2	298
Vagelopoulos	[69]	1998	Counterflow	40.3	1	298
Konov	[72]	2003	Heat flux	40.7	1	298
Bosschaart	[71]	2004	Heat flux	40.7	1	298
Jomaas	[73]	2005	Windowed Vessel	38	5	298

Finally, a list of propane/air measurements is presented in Table 8.

Table 6, 7 and 8 show that there are large discrepancies between reported data for methane, ethane, and propane burning velocities. Additionally, multi-fuel mixtures (i.e. mixtures with methane and ethane or propane) have hardly been tested at all.

Table 8. Overview of propane/air measurements

Researcher	Reference	Year	Technique	SL	P, atm	T, K
Singer	[74]	1952	Burner	47.1	1	298
Egolfopoulos	[66]	1990	Counterflow	43.6	0.5-2	298
Law	[75]	1993	Counterflow	44.1	1	298
Vagelopoulos	[69]	1998	Counterflow	38.5	1	298
Bosschaart	[71]	2004	Heat flux	39.5	1	298
Jomaas	[73]	2005	Windowed Vessel	41.0	1	298
Kitagawa	[76]	2005	Windowed Bomb	39.7	1-5	298
Zhao	[77]	2004	Stagnation Flame	39.0	1	298-650

For mixtures tested at elevated pressures, it has become apparent that instabilities occur on the flame's surface. Since spherically expanding flames at elevated pressures are presented in this study, the mechanisms behind these instabilities will be discussed next.

2.4   Flame Front Instabilities

Cellular flames have been observed for over 80 years on slot burners or with sheet flames. In order to gain familiarity with the concept of cellular flames, some images obtained in this study are shown in Figure 28 and Figure 29 for methane/air flames at 1 and 5 atm, respectively.
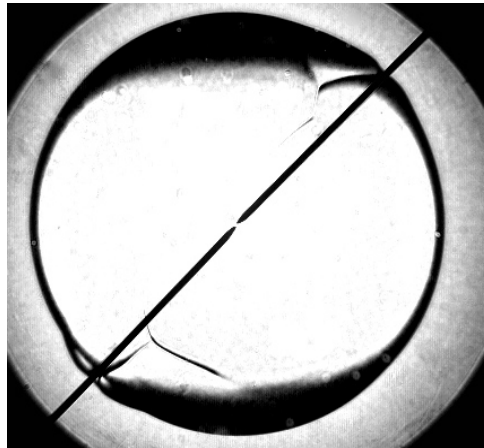
Figure 28. Methane/air at 1 atm, T_i = 300 K, and ϕ = 1.0 (image from this study)
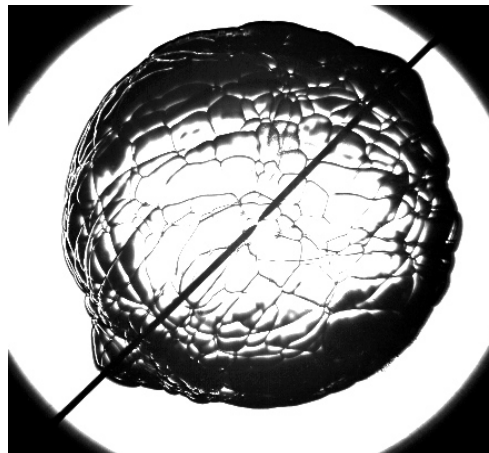
Figure 29. Methane/air at 5 atm, T_i = 300 K, and ϕ = 1.0 (image from this study).

Figure 29 clearly shows a cellular structure on the flame's surface. In general, flame cellularity increases the flame surface area and therefore the burning rate. Flames that are measured in a windowless vessel, where these distortions are undetectable, might therefore falsely be presented as laminar.

Strehlow [78] describes two forms of instabilities, short wavelength instabilities called cellular flames and long wavelength hydrodynamic instability. Strehlow mentions

that the latter is mostly unobservable since the wavelength exceeds the length scales of the most experiments. Whether hydrodynamic or diffusional effects are causing instabilities has been debated over half a century and evidence exists for both.

Manton et al. [53] took high speed images of spherically expanding flames, a summarization of their findings can be seen in Table 9. In Table 9, "+" and "−" signs represent cellular and smooth flame propagation, respectively.

Table 9. Cellular and non-cellular spherical flame propagation in fuel air mixtures as determined by Manton et al. [53]

ϕ	H_2	CH_4	CO	Larger Fuels
Lean	+	+	-	-
Rich	-	-	-	+

Manton et al. explain the difference between hydrodynamic and preferential diffusion instabilities. For clarity, the difference between the two will be explained here.

Hydrodynamic Instability

The principle of a hydrodynamic instability is shown schematically in Figure 30. The thermally expanding gases pass through the flame and cause a local acceleration of the flow. Due to this acceleration, thrust is created in the direction of the unburned gases. When a small flow perturbation causes a ripple to form on the surface of the flame, the flame will be locally concave or convex towards the burned gas as can be seen in Figure

30. Convergence (divergence) in the convex (concave) part of the flame increases (decreases) the local thrust. The local increase or decrease of the created thrust causes these indentations to grow in depth. Some theory behind hydrodynamic instabilities is given by Landau [79] and Darrieus [80]. Karlovitz et al. [81] showed that these perturbations cannot grow indefinitely but have limited amplitudes based on the process of wave propagation.
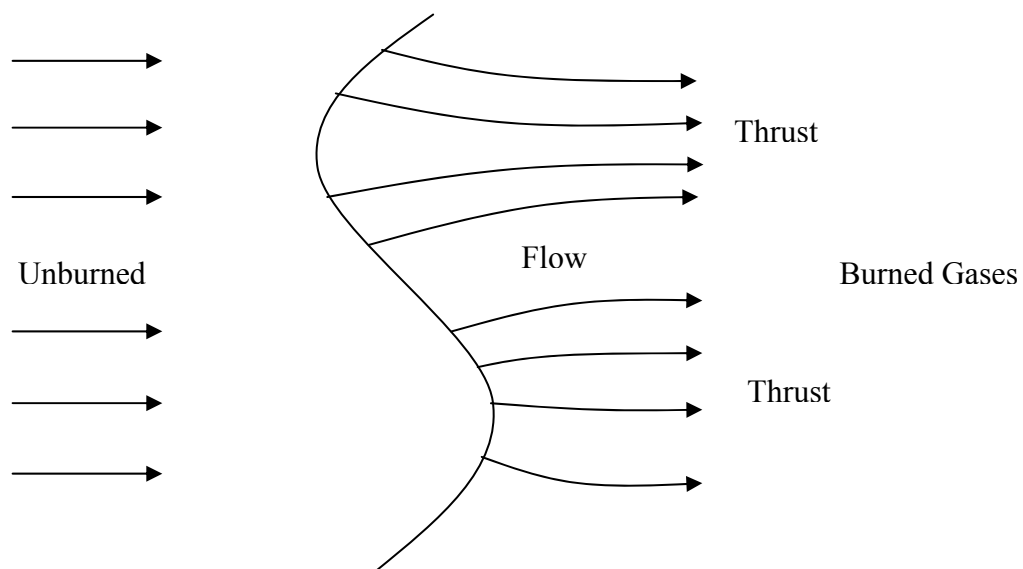
Figure 30. Principle of hydrodynamic instability

Eventually, concave perturbations have the tendency to vanish caused by the convex section's tendency to grow and merge. This will cause the convex surfaces to become flatter as shown in Figure 31. As a consequence, the flame will obtain cracks dividing the flame-front surface into discrete convex cells. These cells are separated by sharp ridges along the lines of neighboring cells [53]. Figure 31 shows that some of the images taken in this study support this theory.
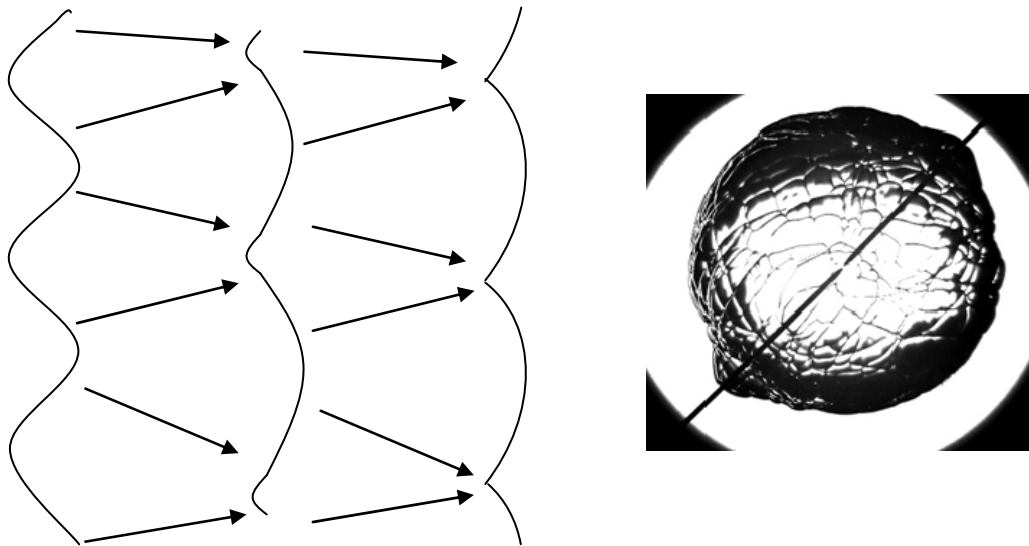
Figure 31. Stabilizing effect of wave propagation

Preferential Diffusion

The results from Manton et al. [53] clearly show a correlation between the non-equal diffusivities of different species on the observed instabilities. In a combustion wave, the mixture is changed by chemical reactions as well as inter-diffusion of reactants and products. When the flame front is planar, all concentration gradients are normal to the wave and all lines of mass flow are parallel to each other. When the wave in concave towards the unburned mixture, concentration gradients of the reactant species diverge. Oppositely, when the wave is convex towards the unburned gases the concentration gradients converge. Locally, the equivalence ratio can change when differences between diffusivities of the fuel and oxidizer exist, resulting in altered flame speeds.

Some of the diffusive effects are captured by a non-dimensional number, called the Lewis number, which measures the relative influence of thermal to mass diffusion. The Lewis number is defined as:

$$Le_{i,j} = \frac{k}{c_p \rho D_{i,j}} = \frac{\alpha}{D_{i,j}} \tag{27}$$

In equation (27), k is the thermal conductivity, c_p, is the specific heat at constant pressure, ρ is the density, α is the thermal diffusivity, and $D_{i,j}$ is the binary molecular diffusivity coefficient between species i and j. The selection of $D_{i,j}$ is arbitrary and usually the diffusion coefficient of the deficient species is used for estimating the Lewis number, i.e. the fuel for lean mixtures or oxygen for fuel rich mixtures.

The underlying principle for preferential diffusion instability is the tendency of non-equal molecular diffusion to alter the local equivalence ratio and therefore the local burning velocity. A qualitative representation on the effect of equivalence ratio on flame speed is shown Figure 32.

Two possibilities exist when non-equal diffusive fuel-oxidizer mixtures are subjected to small flame front perturbations. Either the mass diffusivity of the oxidizer is larger than that of the fuel (ethane and propane), or the mass diffusivity of the fuel is larger than that of the oxidizer, e.g. hydrogen.
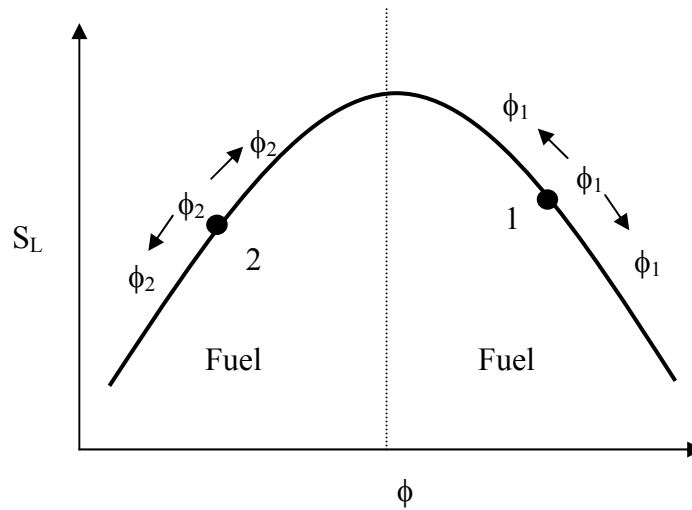
Figure 32. Flame speed versus equivalence ratio

$D_{f,air} < D_{ox,air}$

In the first case, the unburned gases are fuel rich and the oxidizer is more diffusive than the fuel, e.g. ethane and propane as shown in Figure 26. The equivalence ratio of the unburned gases is represented by point 1 in Figure 32.
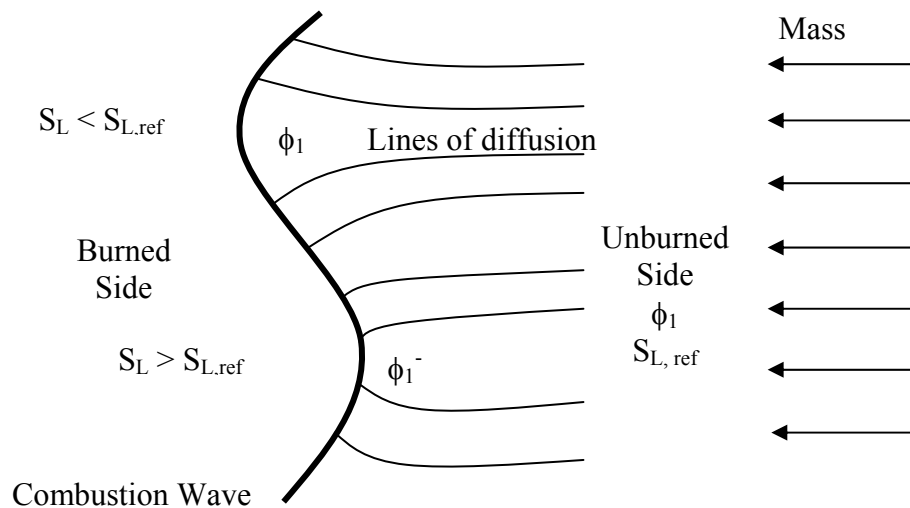
Figure 33. Fuel rich mixtures of heavy fuels, diffusively unstable

Figure 33 shows that at the concave part of the flame, lines of diffusion diverge. Since the oxidizer diffuses more rapidly than the fuel, fuel-air mixtures locally become richer causing the flame speed to decrease. Additionally, at the convex side the diffusive lines converge causing the local fuel-air mixture to become leaner, locally increasing the flame speed. Therefore, heavy fuels in rich mixtures are diffusively unstable. This has been shown by Manton et al. [53] and Kitagawa [76].

$D_{f,air} > D_{ox,air}$

For very light fuels such as hydrogen, the mass diffusivity of the fuel is much larger than that of the oxidizer. Therefore, if the unburned gases are fuel rich, lighter fuels have the tendency to make the fuel-air mixture leaner in the concave section of the flame and richer at the convex part as can be seen in Figure 34.
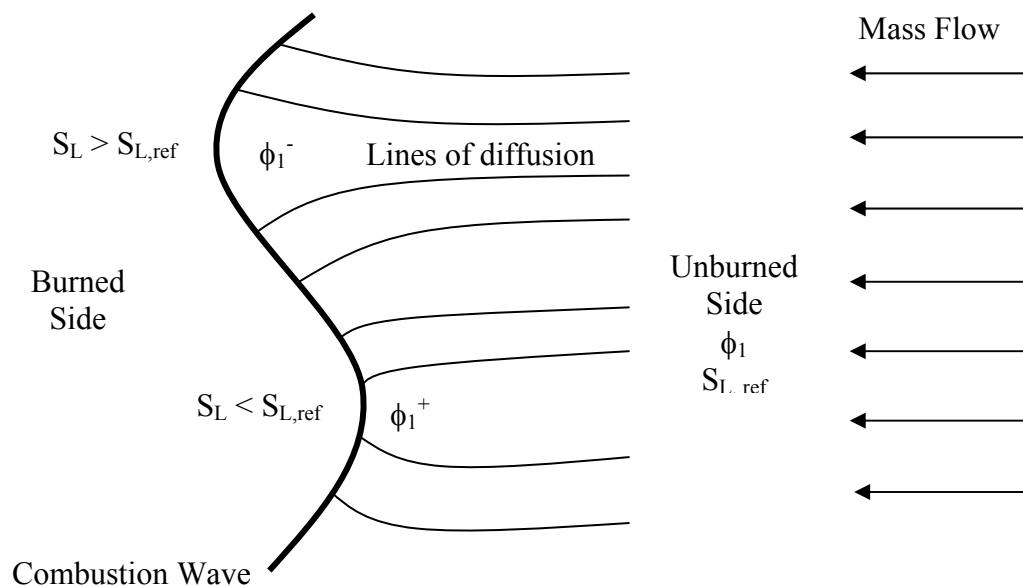
Figure 34. Light fuels are stable at fuel rich conditions

Hydrogen flames are therefore diffusively stable at fuel rich conditions and very susceptible to cellularity under fuel lean conditions.

CHAPTER III

DESCRIPTION OF THE FACILITY

3.1 Design and Hardware

Overall, the facility consists of the vessel hardware, vacuum system, control system, ignition system, high-speed camera, data processing software, mixing tank, and digital data acquisition system. The total layout of the facility can be seen in Figure 35. Each component is described in more detail below. The pressure vessel is comprised of the following components: a thick-shelled cylindrical drum (OD 38.1 cm, 3.18 cm thick), two 9.89-cm thick threaded inserts, two bolted flat heads (OD 38.1, 5.08 cm thick), and two fused quartz cylindrical windows (OD 20 cm, 6.35 cm thick). The internal length of the vessel is 35.6 cm, making it comparable to the inside diameter. The diameter and corresponding volume of the vessel were chosen to minimize the pressure rise during the full use of the aperture, which means this vessel is capable of measuring flames with radii up to 6 cm with less than a 5% rise in pressure. The cylindrical shell has six ports; two ½-inch NPT stainless steel ports for gas supply, two ¼-inch NPT stainless steel ports for insulated electrodes, and one ½-inch NPT ports for the thermocouple and pressure transducer, each. The vessel was built according to the ASME Boiler and Pressure Vessel Code VIII (1 & 3) [82]. Front and side views of the vessel can be found in Figure 36.

Figure 35. General layout of the flame speed facility
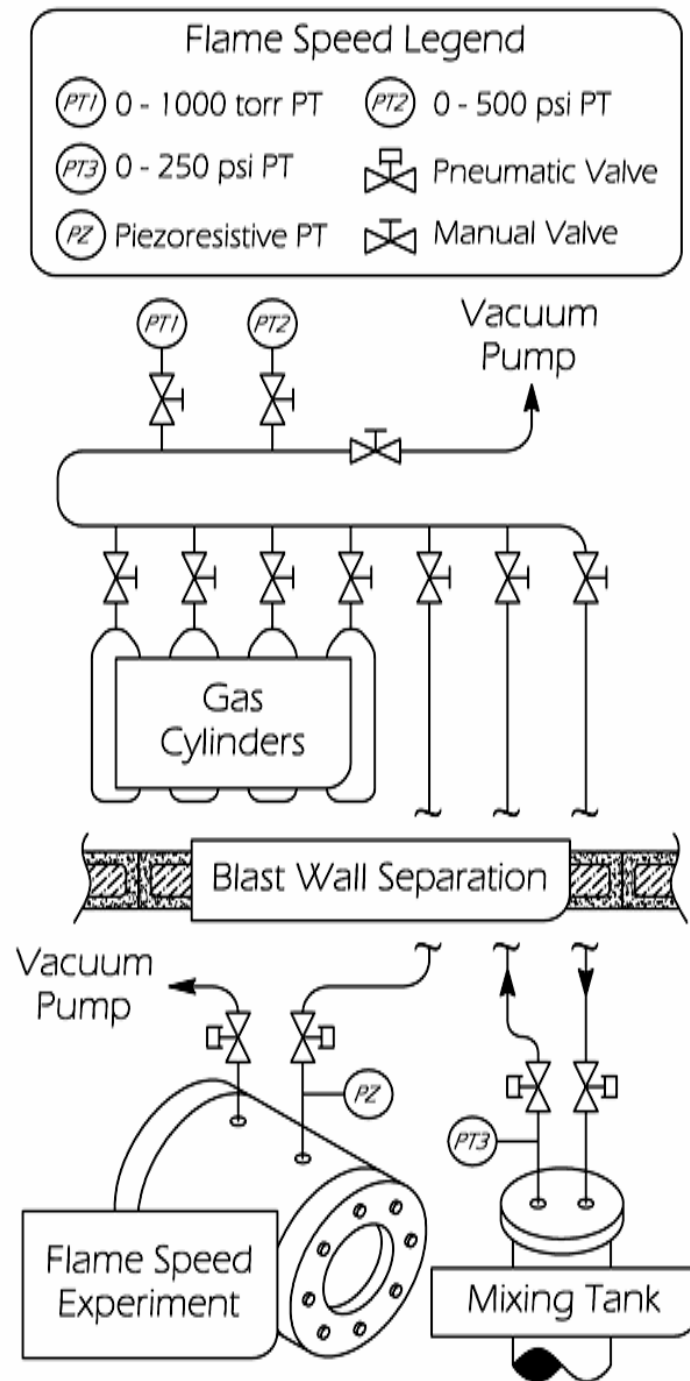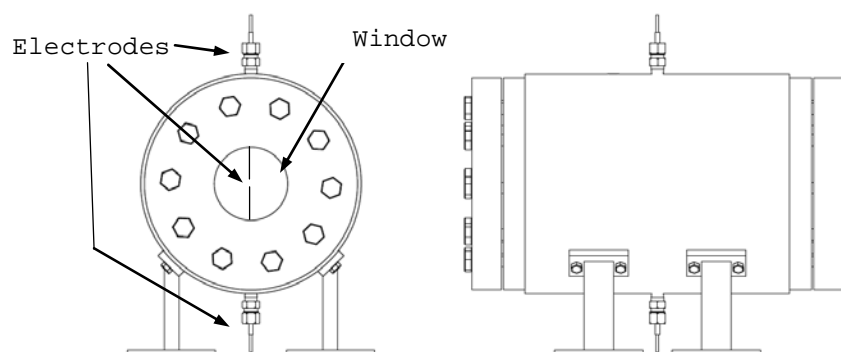
Figure 36. Front and side view of the vessel used in this study

The windows are clamped in between the insert and the endplate and are made of fused quartz because of its favorable transmission range (> 90% for $\lambda = 270 - 2200$ nm) and high temperature resistance. Sealing is provided by two neoprene gaskets (OD 20.3 cm, ID 15.2 cm, 0.318 cm thick), and two parker O-rings (Parker # 2-452).
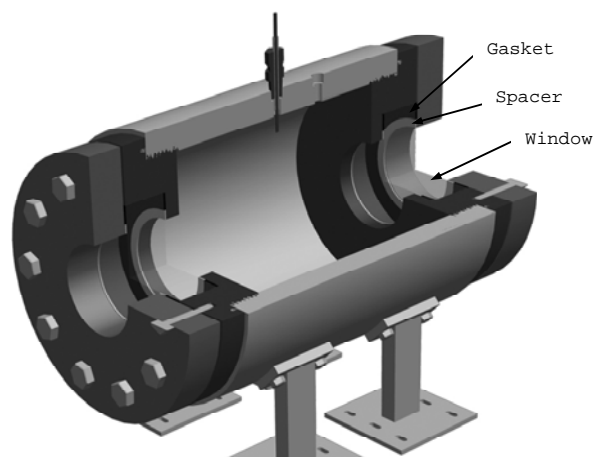
Figure 37. Cutaway view of the flame speed bomb, positions of spacers and gaskets are clearly visible

The gaskets are protected from the hot gases by two stainless steel spacers as can be seen in Figure 37 and Figure 38, leaving a 12.7-cm diameter aperture. More detailed drawings can be found in Appendices C to I.

Figure 38. Projected view showing the location of the windows and the internal dimensions

Vacuum as low as 0.04 mbar is provided by a Varian DS202 Rotary Vane Pump connected to the vessel via ½-inch tubing. For enhanced safety, the whole experiment is shielded by a cement- and steel-reinforced cinderblock blast wall, and high-pressure remote control of the filling and venting processes is provided by 4 electro-pneumatic ball valves. Rupture disks are provided to prevent over pressurization of the flame speed vessel as well as the mixing tank.

3.2   Pressure Rating

Although the ultimate tensile strength for AL 7075 is comparable to that of steel at room temperature (572 versus 505 MPa, respectively, if T304 is used as reference steel), the yield strength-versus-temperature curve is less favorable for the aluminum alloy. The ultimate tensile strength of AL7075-T6 decreases from 572 to 483 MPa when the temperature is increased from 24 ºC to 100 ºC, a decrease of more than 17%. Raising the temperature further causes an even more dramatic reduction in tensile strength and should be avoided [83]. For this reason, it is important to estimate the temperature rise in the vessel wall during high-pressure, stoichiometric experiments (since a stoichiometric mixture will produce the highest flame temperature). A conjugate, unsteady heat transfer analysis was performed using FLUENT for one of the most energetic experiments (P_i = 15 bar, CH_4/Air, ϕ = 1.0) setting the starting temperature of the gas (air) at 2625 K. The 2-D simulation creates a conservative estimate of the wall heating since heat transfer through the two end caps is neglected. A temperature gradient adaptive grid was used with a maximum cell count set at 20,000. The solver was pressure-based and implicit with absolute velocity formulation and Green-Gauss cell-based gradient option. A realizable k-ε model with standard wall functions and full buoyancy effects was used. For simplicity, air with constant c_p (constant-pressure specific heat) and thermal conductivity was used for the gas with properties evaluated at the film temperature of 1600 K (c_p = 1.248 kJ/kg-K and k = 0.106 W/m-K). The aluminum was modeled with c_p = 960 J/kg-K and thermal conductivity k = 130 W/m-K [83].
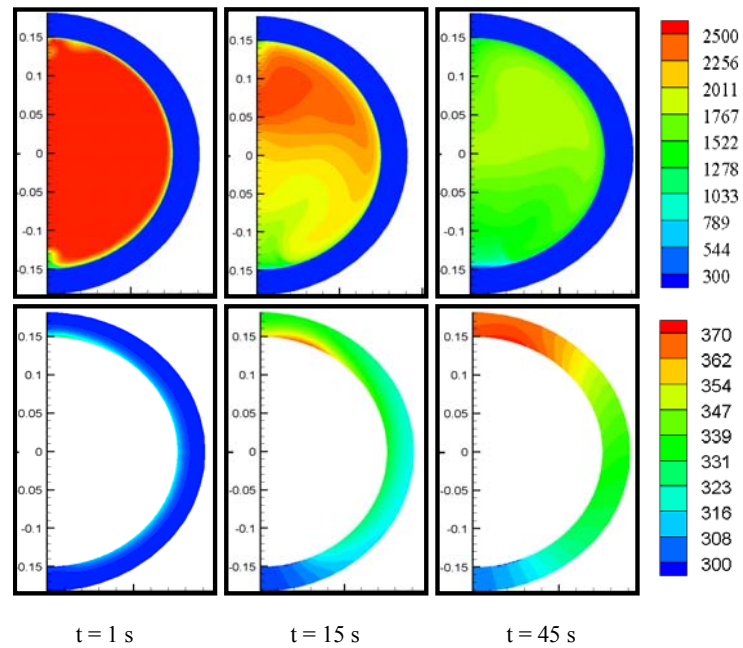
Figure 39. Temperature contours of the gas and the vessel wall at 1, 15, and 45 seconds after the combustion event

A quantitative temperature distribution for the gas and the vessel can be found in Figure 39. Two contour ranges are used to represent the fluid and the solid in Figure 39. Temperature contours of the gas and the vessel wall at 1, 15, and 45 seconds after the combustion event It can be seen that due to natural convection, the highest temperature at the vessel wall occurs at an angular position of about 20º from the top.
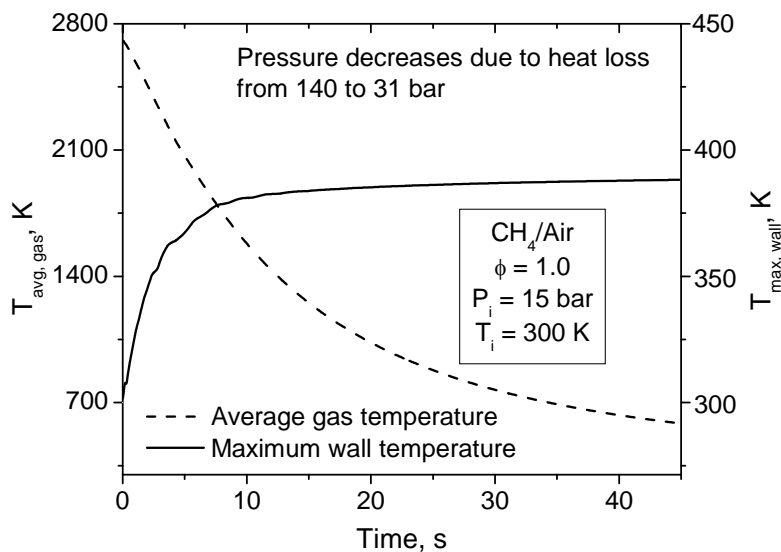
Figure 40. Wall and average gas temperature plotted versus time, maximum wall temperature

remains under 385 K

Figure 40 shows the average temperature of the gas and the maximum temperature of the vessel wall starting right after all the reactants have been consumed and the maximum pressure in the vessel has been reached (2700 K, 136 bar). Forty-five seconds after the pressure peak, the maximum temperature in the vessel wall has only risen from 300 K to 370 K. Even though this temperature is only seen by a small part of the vessel under the most extreme conditions, the material characteristics at 100ºC (ultimate tensile strength $S_u = 483$ Mpa) were used in the design of the pressure vessel to be conservative.

A separate mixing tank is used for pre-mixing fuel and oxidizer before each experiment where the initial pressure is less than 5 bar. Turbulent mixing is provided by a perforated stinger through the center of the mixing tank (Fig. 1). This mixing technique, using the partial pressure method, has proven successful by the authors in

previous studies [84]. Initial pressures of more than 5 bar are directly mixed into the vessel and allowed several hours homogenize.

The pressure rating was found based on the standards set by the ASME pressure vessel code (BPVC) sections II and VIII. AL7075 (100 °C) has an ultimate tensile strength and yield strength of 483 MPa and 427 MPa, respectively, which led to an allowable tensile stress of 106 MPa (BPVC section II-D, appendix 2, Table 2-100(b)). Based on the ultimate stress above, the maximum internal pressure (based on the shell thickness) is 220 bar (BPVC section VIII, UG-27 and UG-53). The critical parts of the design are the threaded inserts. According to the BPVC section VIII-3, appendix E the load on the threads is not uniform but increases from the one thread to the next. With 7 fully engaged threads, the maximum allowable pressure was found to be 140 bar, using a safety factor of 4. This corresponds to the post combustion pressure of a stoichiometric CH_4/Air mixture ignited at 15 bar.

3.3   Instrumentation

Several measurements are made during each experiment. Pre-test vacuum level prior to filling the mixing tank or the flame speed vessel is measured using a Varian 0531 TC vacuum gauge. During the experiment, the pressure history is read by an Endevco 8511A piezo-resistive pressure transducer (0 − 689 bar). The signal is directly fed to a GageScope PCI (5 MHz, 16-bit resolution) data acquisition system. Temperature is measured constantly by a K-type thermocouple inserted 7.6 cm into the vessel. The capacitance discharge ignition system consists of an automotive coil, a 10-µF capacitor,

a solenoid switch, and a constant-current power supply (GwInstek GPR-1810HD), creating a voltage over the spark gap of (0 - 20kV). A schematic of the ignition system can found in Figure 41.

1. 115 V, 60 Hz AC
2. Constant Current Power Supply
3. 12 V DC Source
4. Solenoid
5. Capacitor
6. Ignition Coil
7. Spark Gap
8. Free Floating Ground
9. Nonlocking Normally Open Switch
10. Blast Wall
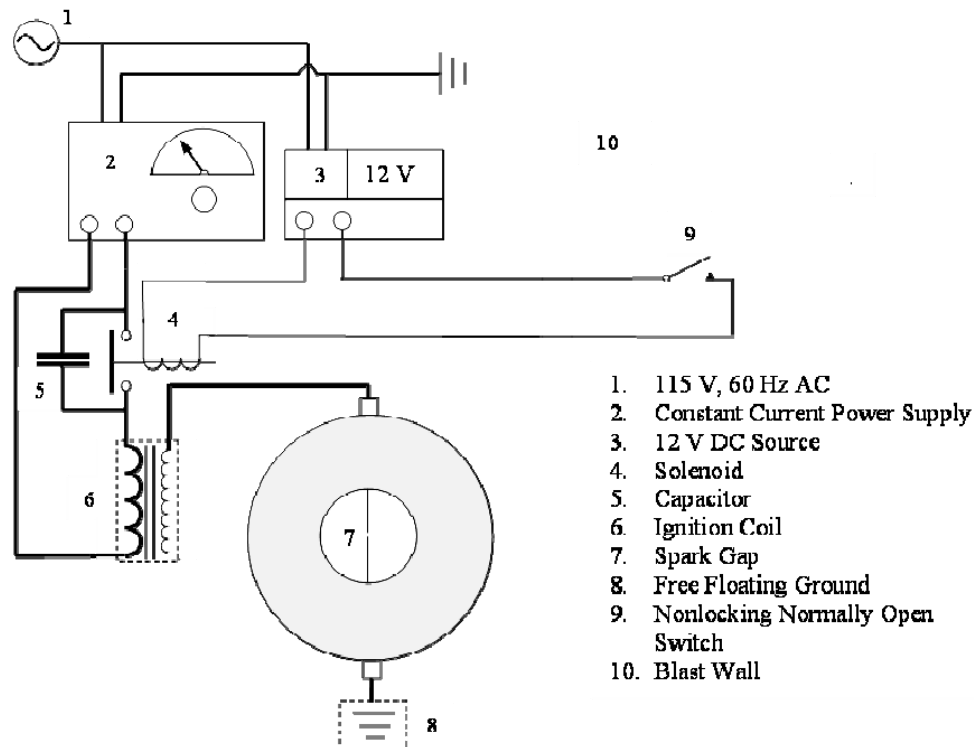
Figure 41. Schematic of the ignition system used in this study

The voltage for each experiment was minimized by continuous adjustment of the current through the primary windings, allowing ignition of the mixture. The electrodes consist of two, 1-mm stainless steel rods sharpened at the tips and set 0.5 – 1.5 mm apart. The receiving electrode is connected to a free-floating ground so the corresponding large voltage spike does not affect other instruments.

3.4 Optical Setup

In this study, a Z-type schlieren system as described by Settles [85] was used. A schematic of this setup is shown in Figure 42. The light source is a mercury arc lamp (100W Mercury Olympus USH-102D) housed in an enclosure (Oriel 66000M). The lamp is powered by a constant-current DC power supply. Parallel light rays through the test area are created by two, 15.2-cm Diameter f/8 parabolic mirrors. The light is sent through a condenser lens (f/8) and a circular aperture at the source side, and steered light caused by the density gradients in the flame are cut off by a pinhole aperture set at the focal point of the second mirror (see Figure 42).
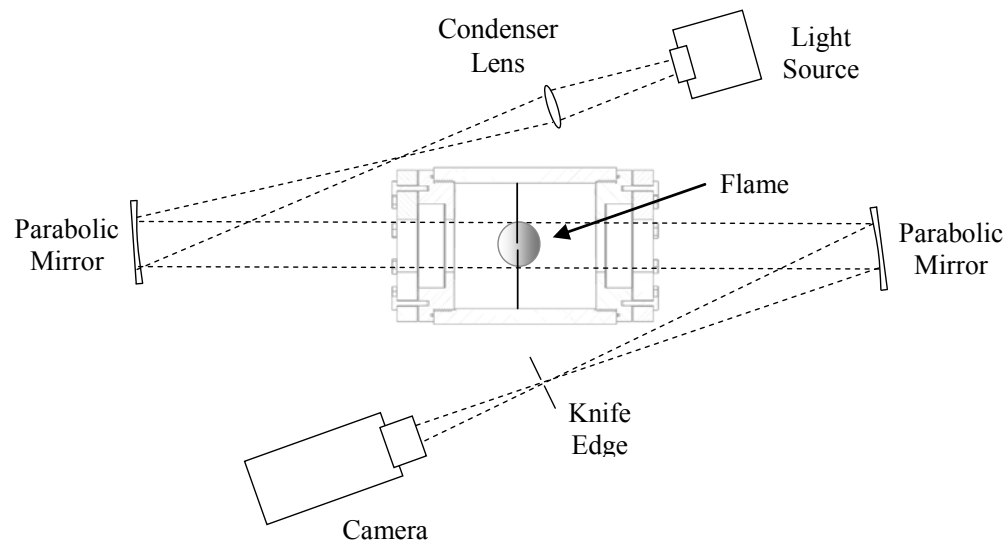
Figure 42. Schematic of the Z-type schlieren setup used in this study

A pin-hole aperture was found to resolve the flam radius with much better resolution than a conventional knife edge, as depicted in Figure 43. Flame propagation is captured

using a high-speed digital camera (Cooke Corp. PCO 1200-hs) with a 12-bit pixel resolution and a frame rate set between 2000 and 3500 fps. The images were analyzed by using image-tracking software developed by Klimek and Wright [86].

3.5 ms	5.5 ms	8.1 ms	10.8 ms

CH$_4$/Air
$\phi = 1.0$
$P_i = 1.01$ bar
$T_i = 298$ K

(a)

2 ms	7.4 ms	12.7 ms	18.1 ms

CH$_4$/C$_2$H$_6$/Air
$\phi = 1.0$
$P_i = 2.0$ 1bar
$T_i = 300$ K

(b)
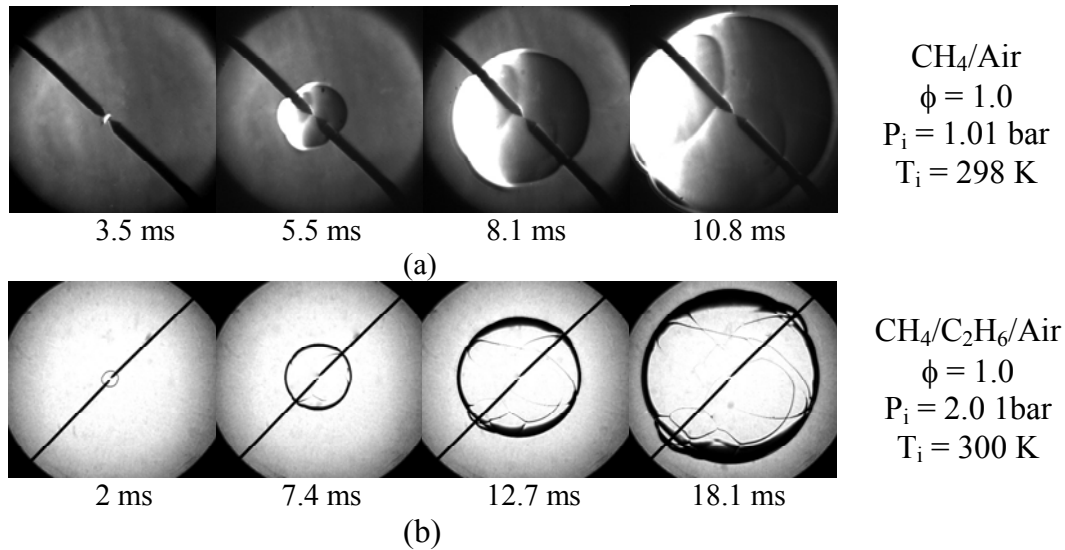
Figure 43. Difference between a vertical knife edge (above) and a pinhole aperture knife edge

3.5   Pressure Versus Radius

Compression-induced flow velocity of the burned gas behind the flame front can significantly alter the measured burning velocity. According to Chen and Ju, a 5% pressure increase can cause a 4% error in the measured flame speed [87]. Figure 44 shows the flame front location relative to the measured pressure rise, indicating that the pressure rise remains within 3% when the flame radius is greater than 5 cm. Figure 44 shows that large flame radii can be measured with relatively small compression effects in the new facility. Using Figure 44 as a guide, the pressure increase at the time the

flame would be at the maximum window aperture of the current setup, 6.35-cm radius is

4%. Flame growth images for 5 different mixtures are shown in Figure 45 (a)-(e). For

very slow flames (high pressure, fuel lean), the buoyancy effect becomes important as

can be seen in Figure 45 (c). In Figure 45 (e), the region of interest is reduced to about

one fourth of the original size; this allows for a higher camera frame rate. For most

experiments, this setting is less favorable because buoyancy effects will remain hidden.

It can be seen in Figure 45 (a) and (d) that increase in pressure can cause detailed,

cellular structures to develop at the flame front increasing the effective flame area and

increasing the flame speed. One of the primary advantages of having optical access

(relative to many earlier windowless flame speed bomb experiments) is the ability to

determine whether the flame has developed cellular structures. The effect of the finite

spatial and temporal resolution on the final uncertainty is discussed in a later section.
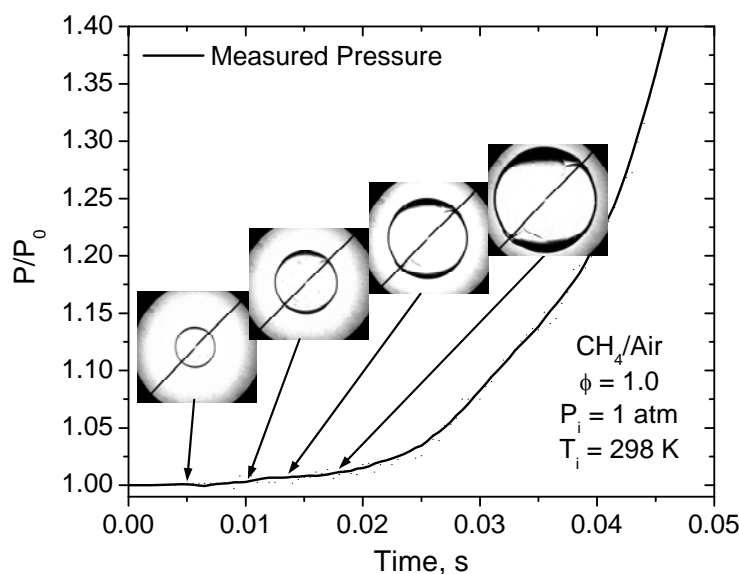
Figure 44. Flame location with respect to total pressure rise
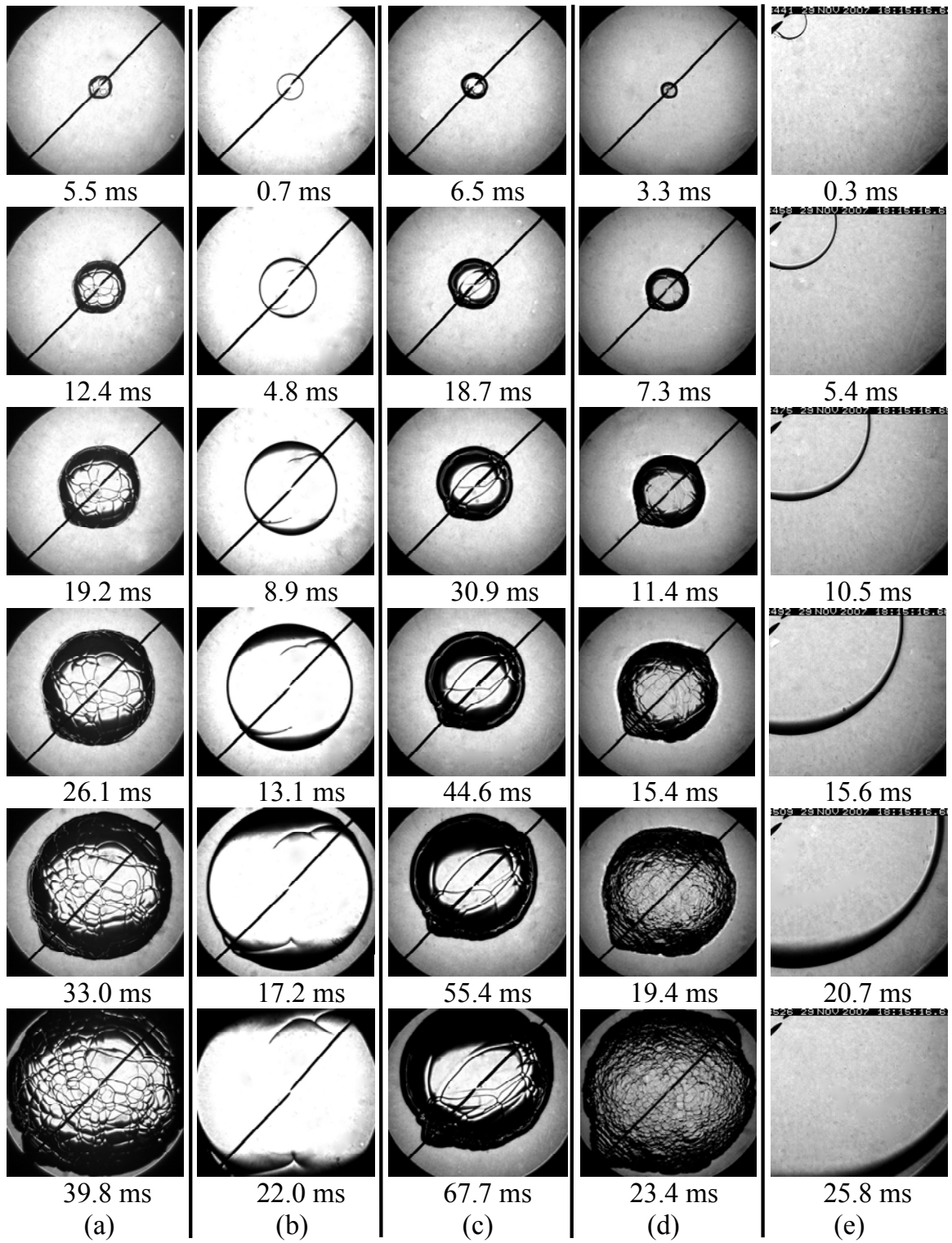
Figure 45. Flame growth for (a) methane/air at 3 atm, (b) methane/air at 1 atm, (c) methane/air at 5 atm, (d) ethane/air at 10 atm, and methane air at 1 atm

3.6   Data Analysis

As mentioned previously, laminar flame speeds are a fundamental combustion characteristic of a specific fuel-air mixture under given thermodynamic conditions. Propagation of a flat, laminar flame front can be modeled utilizing the full chemistry, diffusion parameters, and thermodynamic properties. Therefore, spherical expending flames obtained in this study must be translated into one-dimensional, flat flames.

Curvature of spherical flames imposes stretch which, depending on the fuel and stoichiometry, affects the flame speed. One of the early flame-speed/flame-stretch relationships was proposed by Markstein [88], who defined the flame stretch α as,

$$\alpha = \frac{1}{A_f}\frac{dA_f}{dt} = \frac{1}{4\pi R_f^2}\frac{d4\pi R_f^2}{dt} = \frac{2}{R_f}\frac{dR_f}{dt} \tag{21}$$

In equation (21), R is the flame radius, and "A_f" is the flame surface area. Laminar flame speed can be related to flame stretch as:

$$S_{L,b}^0 = S_{L,b} + L_{m,b}\alpha \tag{22}$$

In equation 22 $S_{L,b}$ and $S_{L,b}^0$ are the stretched and unstretched, burned flame speeds, respectively. $L_{m,b}$ is the burned Markstein length, which is a linear parameter that quantifies the effect of stretch on the flame speed.

Equation 22 can be used to obtain the unstretched flame speed by extrapolating the spherical flame data to zero stretch. Aung et al. [39] found that equation (22) did not match with some of the nonlinearities found when measuring hydrogen/air flames. However, since CH_4/Air, C_2H_6/air, and C_3H_8/air mixtures were used in this study, there is no statistical evidence that a relation other then equation (22) should be used. This result might change when more exotic fuel blends are used in the future (e.g. H_2, CO, etc). In order to acquire the burning velocity with respect to the unburned gases, the results form equation (22) must be divided by the density ratio across the flame so that:

$$S_{L,u}^0 = \frac{\rho_b}{\rho_u} S_{L,b}^0 \tag{28}$$

and

$$L_{m,u} = \frac{\rho_b}{\rho_u} L_{m,b} \tag{29}$$

Matching the radius versus time data with equation (22) is facilitated by integrating the latter equation with respect to time, getting

$$R_f = S_{L,b}^0 t - 2L_{m,b} Ln(R_f) + B \tag{30}$$

In equation (30), R_f is the flame radius, $S_{L,b}^0$ and $L_{m,b}$ are the burned unstretched flame speed and Markstein length, respectively. B is an arbitrary constant that has no impact on

the obtained properties. Unburned properties can be found by using equations (28) and (29).

Figure 46 shows the flame speed versus flame stretch as obtained from (30). Alternatively, the flame speed and stretch can be found directly by using finite differencing (FD) on the radius- versus-time data array. It is evident that small perturbations in measured flame front radius due to finite camera resolution, optical aberrations, and flame front imperfections can cause some variance in the obtained flame speeds, which is represented by some of the scatter in Figure 46.
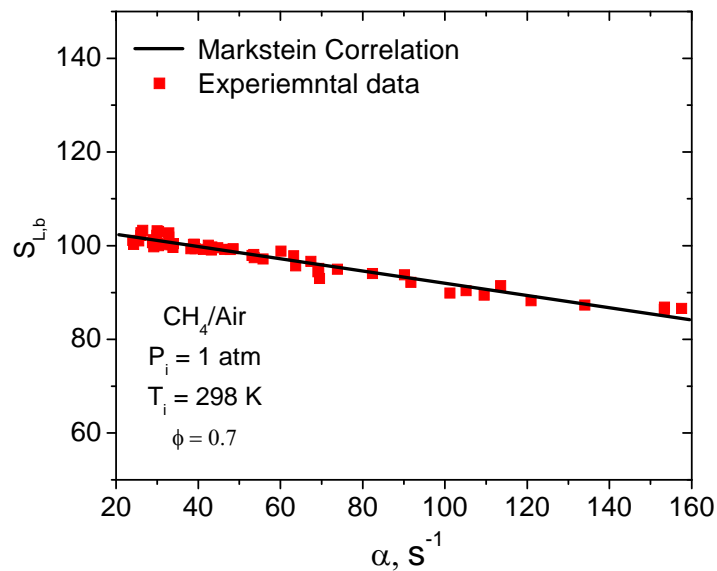
Figure 46. Flame speed versus flame stretch obtained using finite differencing and by using equation

(30)

Equation (30) circumvents the need for FD. An additional advantage is that the unstretched flame speed S_L^0 is directly obtained as one of the regression parameters.
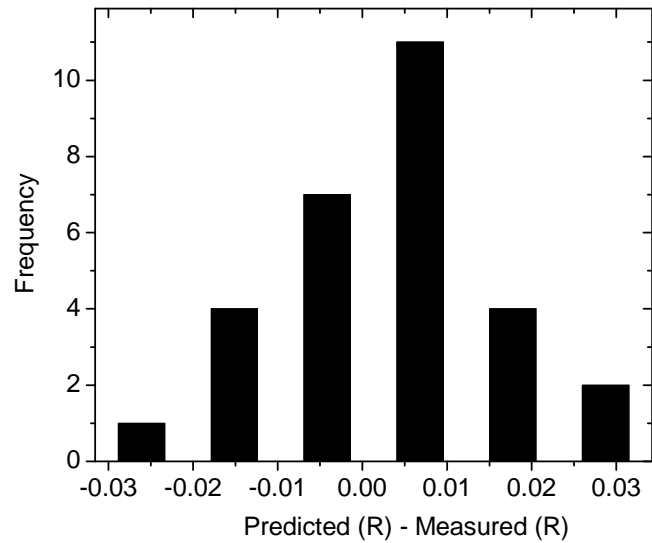
Figure 47. Distribution of residual errors obtained from subtracting experimental data from equation (30)
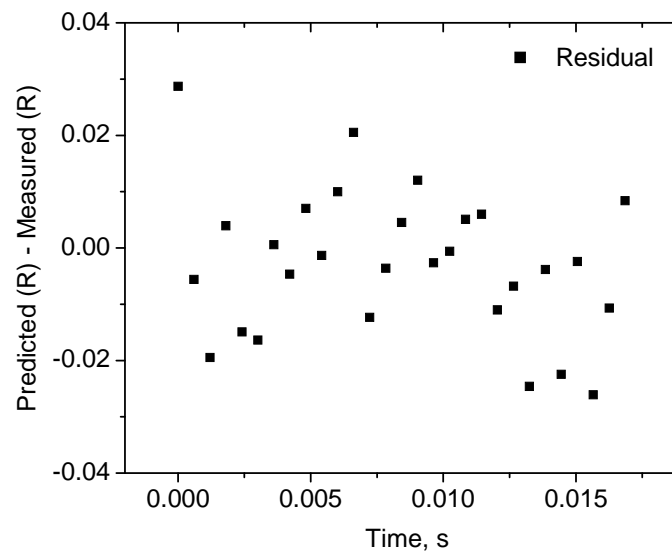
Figure 48. Residual error plotted against time showing no trend

The validity of Markstein's linear flame speed versus stretch relationship can be investigated by doing a residual analysis, where the residuals herein are defined as the

difference between the measured radii and those predicted by equation (22). Equation (30) is an implicit function of the flame radius. Therefore, Newton-Raphson was used to find the radius corresponding to each time step.

For further statistical analysis, it is important to validate the assumption that the residuals are approximately normally distributed by creating a normal probability plot, as can be seen in Figure 47, which shows that the perturbations caused by finite camera resolution and flame front imperfections are normally distributed.

Figure 48 shows the residual errors as a function of the time showing no particular pattern. These small yet random residuals, together with a coefficient of determination, $R^2 > 0.99993$ indicate that equations (21) and (22) do a sufficient job at describing the physical nature of the spherical flame propagation concerning CH_4/Air mixtures. More detail about some of the sources of uncertainty is given in the following section.

3.7   Uncertainty Analysis

The statistical uncertainty for each experiment is determined by adding the bias error and the precision error, where the latter is determined herein by repeating some experiments over 5 times. Being a fixed value, the bias error cannot be estimated by statistical methods alone and can sometimes be difficult to uncover. Obtaining the systematic error is further complicated by the fact that the experiment cannot be calibrated against a local standard since reported values (inter-laboratory comparison) of even simple mixtures (CH_4/Air) have a larger spread than the estimated uncertainty reported in this study.

Table 10. Elemental uncertainties contributing in the total flame speed uncertainty

#	Elemental error source	Systematic, B_i	Random, S_i	Degrees of freedom, ν
U1.0	**Transducer 0-1000 Torr**			
U1.1	Non-linearity	0.150%		
U1.2	Hysterisis	0.200%		
U1.3	Non-Repeatbility	0.020%		
U1.4	Display Resolution (psi)		0.0500	30
U2.0	**Transducer 0-250 Psi**			
U2.1	Non-linearity			
U2.2	Hysterisis			
U2.3	Non-Repeatbility	0.120%		
U2.4	Display Resolution (Torr)		0.0500	30
U3.0	**Thermocouple K-Type**			
U3.1	Accuracy (K)	1.500		
U3.2	Display Resolution (K)		0.0500	30
U3.3	Spatial Variation (K	1.000		
U3.4	Radiation (K)	1.500		
U4.0	**Repeatability**			
U4.1	Auxilary test (cm/s)		0.3680	4
U5.0	**Camera Resolution**			
U5.1	Finite Pixel (cm)		0.0147	30
U6.0	**Markstein Correlation**			
U6.1	Sx (cm)		0.0159	
U7.0	**Optical aberrations**			
U7.1	Spatial (cm)	0.0281		
U8.0	**Non uniform flame front**			
U8.1	Radius Variation		0.0130	7
U9.0	**Calibration (Pixels to cm)**			
U9.1	Resolution (cm)		0.0147	30
U10.0	**Schlieren limit**			
U10.1	1 pixel (cm)	0.029		

There are several sources that can contribute to the fixed uncertainty, and all elemental sources are numbered U1.0 to U10.1 and are listed in Table 10. Some individual components have several elemental errors which are divided into systematic and random errors. Each random (precision) error has a corresponding degree of freedom, ν, which is important to find the student t of a single-run experiment. All mixtures are created using the partial pressure method, obtaining the pressure through

the 0-1000 Torr and 0-250 psi pressure transducers. The elemental errors caused by non-linearity, hysteresis, non-repeatability, and display resolution are listed in Table 10 by U1.0 through U2.4. These pressure transducers are also used to find the initial pressure before ignition.

Initial temperature is established via a K-type thermocouple which, besides accuracy and display resolution, has an error caused by a potentially non-uniform temperature profile inside the vessel and through radiating effects to the vessel walls. It will be shown later that the flame speed is a strong function of the initial temperature. A difference of lab temperature of 5 degrees can result in a 3.4% difference in measured burning velocity. For atmospheric methane-air, this can be as much as 1.2 cm/s, comparable to the standard deviation of reported data in the literature.

Besides pressure and temperature, there are several optical sources for elemental errors, such as camera resolution, aberrations, pixel-to-distance calibration, and the schlieren limit (all listed in Table 10). Finally, precision error contribution can be expected from repeatability, Markstein lengths, and flame-front non uniformities.

The mixtures created in a separate mixing tank have an uncertainty in the fuel-to-air equivalence ratio. The flame speed is a strong function of the fuel/air ratio as was shown in Figure 32. An uncertainty in reported equivalence ratio will result in an uncertainty in measured flame speed. Additionally, when the mixture is introduced into the flame speed vessel, the reported pressure and temperature have inherent uncertainties caused by the thermocouple and pressure transducer errors. The temperature measurement is

further complicated by the fact that the thermocouple junction is inserted into a radiating environment where the walls may have different temperatures than the gas nearby.

Table 10 summarizes the different error sources and their respective values. Note that elemental errors are divided into systematic (B_i) and random errors (S_i). Only the systematic elemental errors are used to determine the bias error. All values are obtained through factory specifications or by simple measurements. The precision error can be found by repeating an experiment M times at the same conditions, resulting in a mean value and a standard deviation. This standard deviation was multiplied with the value of the student t for 4 degrees of freedom ($v = 5$) and a 95% confidence interval ($t_{4,95}$) and divided by the square root of M.

To summarize, the overall reported uncertainty is found by adding the systematic uncertainty and the precision error using RSS

$$u_{S_L} = \sqrt{B_{S_L}^2 + \left(\frac{t_{M-1,95}S_{S_L}}{\sqrt{M}}\right)^2} \ (95\%) \tag{31}$$

Where u_{SL} is the uncertainty in measured flame speed at a 95% confidence interval, B_{SL} is the total bias uncertainty, M is the number of repeated experiments per condition, S_{SL} is the standard deviation found through the repeated experiments, and $t_{M-1,\ 95}$ is the student t value at a 95% confidence interval and M − 1 degrees of freedom. When an experiment is repeated 5 times, then the student t factor becomes $t_{4,95\%} = 2.78$.

The bias uncertainty B_{SL} is found by

$$B_{S_L} = \sqrt{\sum_{i=1}^{N} \left(\frac{\partial S_L^0(x_i)}{\partial x_i} u_i \right)^2}$$

(32)

Where u_i are all the elemental bias uncertainties listed in Table 10, $S_L^0(x_i)$ is the functional relationship between the flame speed and the equivalence ratio, initial pressure, initial temperature, optical aberrations, and schlieren limit, as listed in Table 10, and x_i represents each elemental error source.

Equation (32) shows that a functional relationship between the measured laminar flame speed, equivalence ratio, initial pressure, and initial temperature must be established in order to determine the required partial derivatives, $\frac{\partial S_L^0(x_i)}{\partial x_i}$. For each error source, it is evident that the functional relationship $S_L^0(\phi,P,T)$ must be known. There have been several correlations proposed that relate the burning velocity to the initial pressure, temperature, and equivalence ratio.

Elia et al. [41] proposed a correlation of the form

$$S_{L,u}^0 = f(\phi) \left(\frac{T}{T_0} \right)^{\alpha} \left(\frac{P}{P_0} \right)^{\beta}$$

(33)

where T_0 and P_0 are the reference temperature and pressure (298 K and 1 atm), respectively, and α and β are two fitting parameters ($\alpha = 1.857$, $\beta = -0.435$)

An alternate correlation is given by Sharma et al. [89]

$$S_{L,u}^0 = f(\phi)\left(\frac{T}{300}\right)^{1.68/\sqrt{\phi}} \quad \text{for } \phi < 1$$

$$S_{L,u}^0 = f(\phi)\left(\frac{T}{300}\right)^{1.68\sqrt{\phi}} \quad \text{for } \phi > 1$$

(34)

With

$$f(\phi) = -418 + \frac{1287}{\phi} - \frac{1196}{\phi^2} + \frac{360}{\phi^3} - 15\phi(log_{10}P)$$

(35)

Finally, Iijima and Takeno came up with a more complicated correlation

$$S_{L,u}^0 = S_{su}\left[1 + \beta log\left(\frac{P}{P_0}\right)\right]\left(\frac{T}{T_0}\right)^{\alpha}$$

(36)

where the reference pressure and temperature are $P_0 = 1$ atm and $T_0 = 291$ K [64], respectively. S_{su}, α, and β are all functions of ϕ and are given by

$$S_{su} = 36.9 - 210(\phi - 1.12)^2 - 335(\phi - 1.12)^3$$

(37)

$$\alpha = 1.60 + 0.22(\phi - 1) \tag{38}$$

$$\beta = -0.42 - 0.31(\phi - 1) \tag{39}$$

Figure 49 shows the three aforementioned correlations in comparison to data taken in the present facility.
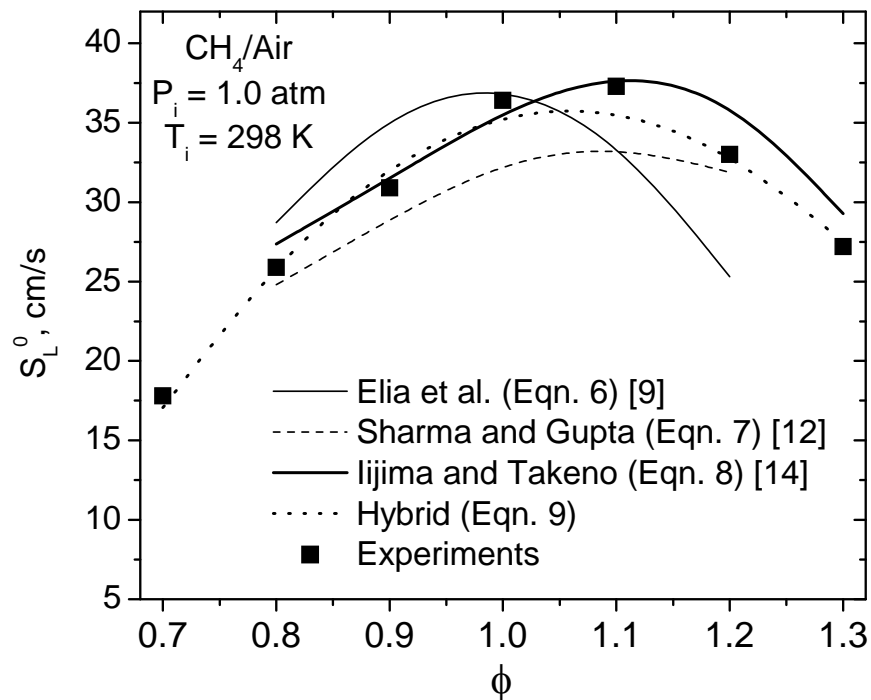
Figure 49. Correlations given by equations (33)-(39) plotted against atmospheric methane/air data obtained in this study

In addition to existing correlations, a hybrid correlation was created from the temperature coefficient taken from Elia et al. [41] ($\alpha = 1.857$) and using the best fit

through the data obtained in this study with respect to the equivalence ratio, ϕ and the pressure, P. The resulting empirical correlation is given by equation (40).

$$S_{L,u}^0 = (130.76 + 315.52\phi - 149.047\phi^2)\left(\frac{P}{P_0}\right)^{-0.314}\left(\frac{T}{T_0}\right)^{1.857} \tag{40}$$

In equation (40), the reference pressure and temperature are $P_0 = 1$ atm and $T_0 = 298$ K, respectively. Equation (40) is shown in Figure 49 in comparison to the data found herein. Since equation (40) best represents the data, it is used in the uncertainty analysis by taking the partial derivatives with respect to ϕ, P, and T and inserting those in equation (32).

It can be seen that the pressure dependency is represented by an exponential decay of -0.314 and that the temperature dependency is much stronger, given by a factor of 1.857. Uncertainties in initial temperature have therefore a stronger effect than uncertainties in initial pressure.

Table 11. Summary of measured uncertainties for atmospheric methane/air mixtures

ϕ	S_L (cm/s)	B_{SL} (cm/s)	S_{SL} (cm/s)	u_{SL} (cm/s)	%
0.7	17.80	0.723	0.368	1.00	5.59
0.8	25.90	0.640	0.470	1.08	4.18
0.9	30.90	0.597	0.164	0.67	2.17
1	36.40	0.580	0.566	1.20	3.30
1.1	37.30	0.579	0.332	0.85	2.27
1.2	33.00	0.593	0.907	1.79	5.41
1.3	27.20	0.630	0.740	1.51	5.56

Table 11 summarizes the measured flame speed for CH_4/Air mixtures, with equivalence ratios ranging from $\phi = 0.7$ to 1.3. The bias error (systematic error B_{SL}) was found by combining equations (32) and (40), and the standard deviation (S_{SL}) was obtained through repeated experiments (typically five times). The overall uncertainty, u_{SL}, per mixture is obtained through equation (31) and shown in Table 11 both as absolute values and as percentages of the measured flame speed. The overall uncertainty in measured flame speed ranges between 2.5 and 6%.

To summarize, both the systematic and the precision errors were obtained for each measured mixture and initial condition and combined through the RSS method. The uncertainty obtained is slightly higher for fuel lean and rich mixtures since the absolute value of the partial derivative with respect to ϕ is higher in these regimes. Small initial temperature perturbations can be corrected for using equation (40).

CHAPTER IV

MODELING

4.1   General Structure

In this study, all modeling was done using CHEMKIN-III, a FORTRAN chemical

kinetics package for the analysis of gas-phase chemical and plasma kinetics [90]. The

CHEMKIN-III package consists of several individual FORTRAN routines whose

purpose is to facilitate the formation, solution, and interpretation of problems involving

elementary gas-phase chemical kinetics. The package consists of two major software

components:

- An interpreter that links reaction rates and thermodynamic information to one

  linking file

- A gas-phase subroutine library. In this study, the gas-phase library routines used

  are transport and premix.

One of the main advantages of the CHEMKIN structure is that it has standardized the

input protocol for chemical information, allowing the analyst to work with the same

chemical input regardless of the particular problem.

CHEMKIN-III is an updated version of the original CHEMKIN, published in 1980.

The second version, CHEMKIN-II allowed for accurate expression of pressure

dependent reactions. CHEMKIN-III allows for the treatment of non-equilibrium multi

fluid systems. Additionally, new capabilities include the expression of non-integer

stoichiometric coefficients. Both these additions are useful for describing plasma

systems and have little bearing on modeling premixed laminar flames as used in this study.

CHEMKIN is now a commercial product developed and sold by reaction design®. Some of the latest versions include: CHEMKIN 4.0 and CHEMKIN-PRO. Both have a full graphical user interface and can be used for parametric studies.

In this study, a custom graphical user interface was utilized, created specifically for analyzing premixed laminar flames. This tool was developed at Rolls-Royce Canada and allowed for the management of input files, mechanism storage, and post process analysis.

The modeling of laminar, planar, premixed flames happens in three steps: First the reaction rates and thermodynamic data are read by a FORTRAN interpreter (chem.exe). Second, the transport properties, such as the conductivity, diffusivity, and viscosity must be calculated based on collision theory and given Lenard-Jones parameters. This is done using the tran.exe routine. Finally, the chem.exe and tran.exe outputs are combined and used by premix.exe together with an input file describing the initial unburned conditions of the flame.

The remainder of this chapter describes these individual routines in more detail, followed by a description of the two chemical kinetic mechanisms used in this study.

Chem.exe

Chem.exe is an interpreter that reads a symbolic description of the reaction mechanism and extracts the thermodynamic information per species from the thermodynamic database (therm.dat). After successfully linking the kinetic and

thermodynamic data, chem.exe creates two outputs. One is a binary file called the linking file (chem.bin) and the second is an ASCII output file (chem.out) that summarizes the species and reactions processed as well as any potential errors caused by improper input formulations.

Figure 50 shows a schematic diagram of CHEMKIN's general structure. Once the chem.bin linking file is created, the user is ready to use the specific FORTRAN routines describing the problem.
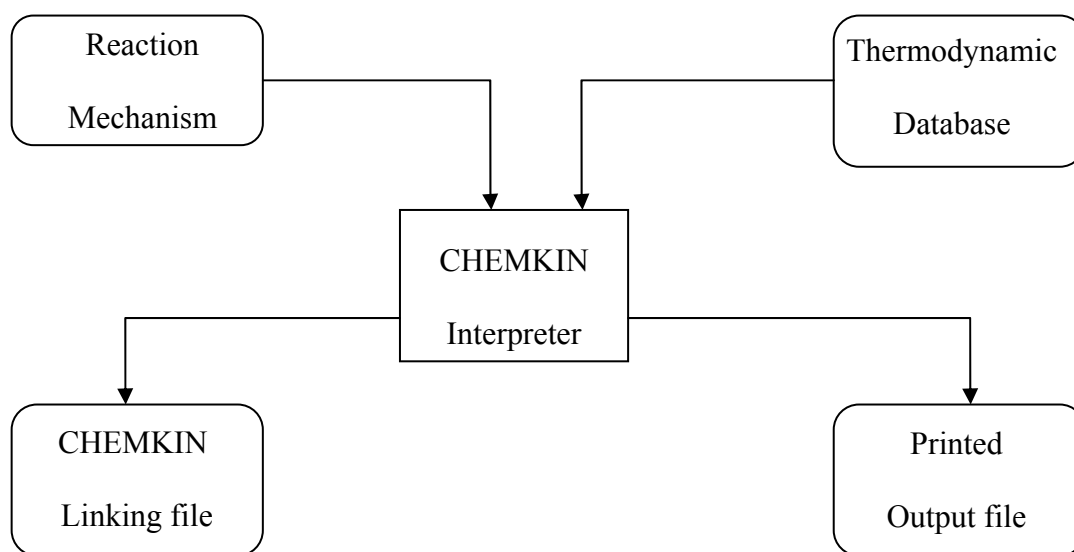
Figure 50. Schematic of CHEMKIN III's general structure

Chem.inp

Chem.inp forms the symbolic description of the reaction mechanism. It must start with a declaration of the elements involved. In this study these elements include N, O, H, and C. After the element statement, all individual species present in the reaction

mechanism must be identified. An example of the elements and species declaration section of a well known chemical reaction mechanism (GRI 3.0) is shown in Figure 51.

```
! GRI-Mech Version 3.0 7/30/99  CHEMKIN-II format
! See README30 file at anonymous FTP site unix.sri.com, directory gri;
! WorldWideWeb home page http://www.me.berkeley.edu/gri_mech/ or
! through http://www.gri.org , under 'Basic  Research',
! for additional information, contacts, and disclaimer

ELEMENTS
O   H   C   N   AR
END
SPECIES
H2          H          O          O2         OH         H2O        HO2        H2O2
C           CH         CH2        CH2(S)     CH3        CH4        CO         CO2
HCO         CH2O       CH2OH      CH3O       CH3OH      C2H        C2H2       C2H3
C2H4        C2H5       C2H6       HCCO       CH2CO      HCCOH      N          NH
NH2         NH3        NNH        NO         NO2        N2O        HNO        CN
HCN         H2CN       HCNN       HCNO       HOCN       HNCO       NCO        N2
AR          C3H7       C3H8       CH2CHO     CH3CHO
END
```

Figure 51. Truncated example of element and species declaration part of a CHEMKIN input mechanism file (GRI 3.0 [26])

All reactions in the chem.inp mechanism expresses the forward rate constants for the I-reactions according to the following Arrhenius temperature dependence.

$$k_{f,i} = A_i T^{\beta_i} exp\left(\frac{-E_i}{R_c T}\right)$$

(41)

In equation (41) $k_{f,i}$ is the forward rate of the i'th reaction, A_i is the pre-exponential factor, β_i is a secondary temperature dependency, E_i is the activation energy, R_c is the universal gas constant, and T is the temperature.

The reverse rates for each reaction can be explicitly presented or calculated via the equilibrium constant. An example of a forward and backward reaction would then be:

	A	β	E
H+O2<=>O+OH	1.92E+14	0.0	16440.0
Rev/	5.48E+11	0.4	-293.0

In some reactions a third body [M] is required for the reaction to proceed. This is often the case for dissociation or recombination reactions. In this case, the progress variable per reaction must be modified by the first term on the right hand side of the following equation:

$$q_i = \left(\sum_{k=1}^{K} (\alpha_{ki}) [X_k] \right) \left(k_{fi} \prod_{k=1}^{K} [X_k]^{v'_{ki}} - k_{ri} \prod_{k=1}^{K} [X_k]^{v''_{ki}} \right) \tag{42}$$

In equation (42), α_{ki} represent the collision efficiencies per species. When all species in the mixture contribute equally as third bodies, the first term on the right hand side of equation (42) collapses to the following:

$$\sum_{k=1}^{K} (\alpha_{ki}) [X_k] = \sum_{k=1}^{K} [X_k] = [M] \tag{43}$$

The Arrhenius rate expression is solely a function of temperature. However, some reaction rates depend on pressure as well as temperature. One can imagine that at sufficiently high pressure, the appropriate description of methyl recombination is CH_3 + $CH_3 \Leftrightarrow C_2H_6$. However, at low pressures a third body is required to provide the energy necessary for the reaction to proceed. When the reaction is either in the high pressure or low pressure limit, the rate is solely a function of temperature. When the pressure and temperature are such that the reaction is in between those limits, the rate expression becomes more complicated.

Typically, CHEMKIN expresses a reaction that is in between the low and high pressure limit with a +M enclosed in parentheses. (e.g. CH_3 + CH_3 (+M) $\Leftrightarrow C_2H_6$ (+M). There are several methods available for describing the reaction rate between the two pressure limits. These methods are:

- Lindermann method

- Troe fall-off

- Stewart et al.

In the mechanisms employed in this study, the Troe's fall approach is used. In this case, the rate coefficients for the low and high pressure limit are given as k_0 and k_∞, respectively. k_0 and k_∞ are expressed in regular Arrhenius form so that,

$$k_0 = A_i T^{\beta_0} exp\left(\frac{-E_0}{R_c T}\right)$$

(44)

And

$$k_{f,\infty} = A_\infty T^{\beta_\infty} exp\left(\frac{-E_\infty}{R_cT}\right)$$

(45)

At any pressure, the rate coefficient if found by

$$k = k_\infty \left(\frac{P_r}{1 - P_r}\right) F$$

(46)

Where the reduced pressure in given by $P_r = k_0[M]/k_\infty$. The value for F can be found as follows:

$$logF = \left[1 + \left[\frac{logP_r + c}{n - d(logP_r + c)}\right]\right] logF_{cent}$$

(47)

where $c, n, d,$ and F_{cent} are expressed as:

$$c = -0.4 - 0.67logF_{cent}$$

(48)

$$n = -0.75 - 1.2767logF_{cent}$$

(49)

$$d = 0.14$$

(50)

And

$$F_{cent} = (1 - \alpha)exp\left(\frac{-T}{T^{***}}\right) + \alpha\, exp\left(\frac{T}{T^*}\right) + exp\left(\frac{-T^{**}}{T}\right) \qquad (51)$$

The values for a, T^*, T^{**}, and T^{***} are input parameters expressed in the input mechanism. An example of a pressure dependent reaction rate expression for CH3O(+M) $\Leftrightarrow$ CH2O+H(+M) with enhanced collision efficiencies for H_2, H_2O, CO, CO_2, CH_4, and C_2H_6 is given in Figure 52.

```
CH3O(+M)<=>CH2O+H(+M)        6.80E+13     0.0      26170.0
Low pressure limit:          0.18670E+26 -0.30000E+01  0.24307E+05
TROE centering:       0.90000E+00  0.25000E+04  0.13000E+04  0.10000+100
        H2              Enhanced by   2.000E+00
        H2O             Enhanced by   6.000E+00
        CO              Enhanced by   1.500E+00
        CO2             Enhanced by   2.000E+00
        CH4             Enhanced by   2.000E+00
        C2H6            Enhanced by   3.000E+00
```

Figure 52. Example of pressure dependent reaction as expressed in an input mechanism

Chem.out

Figure 53 shows a truncated version of the chem.out file. The statement "NO ERRORS FOUND ON INPUT" is important and expresses a successful creation of the linking file.

```
CHEMKIN-III GAS-PHASE MECHANISM INTERPRETER:
DOUBLE PRECISION Vers. 6.15 98/03/03
Copyright 1995, Sandia Corporation.
The U.S. Government retains a limited license in this software.
                       --------------------
                       ELEMENTS    ATOMIC
                       CONSIDERED  WEIGHT
                       --------------------
                        1. C       12.0112
                        2. H        1.00797
                        3. N       14.0067
                        4. O       15.9994
                        5. AR      39.9480
                        6. HE       4.00260
                       --------------------
```

```
-------------------------------------------------------------------------
                      C
                  P   H
                  H   A
                  A   R
SPECIES           S   G   MOLECULAR  TEMPERATURE  ELEMENT COUNT
CONSIDERED        E   E   WEIGHT     LOW    HIGH  C  H  N  O  AR HE
-------------------------------------------------------------------------
  1. H            G   0    1.00797   300    5000  0  1  0  0  0  0
  2. H2           G   0    2.01594   300    5000  0  2  0  0  0  0
  3. C            G   0   12.01115   300    5000  1  0  0  0  0  0
  4. CH3COCH2O2H  G   0   90.07947   300    5000  3  6  0  3  0  0
                            (etc)
-------------------------------------------------------------------------
                                     (k = A T**b exp(-E/RT))
      REACTIONS CONSIDERED           A        b          E

  1. H+O2<=>O+OH                     1.92E+14   0.0   16440.0
     Reverse Arrhenius coefficients: 5.48E+11   0.4    -293.0
  2. O+H2<=>H+OH                     5.08E+04   2.7    6292.0
     Reverse Arrhenius coefficients: 2.67E+04   2.6    4880.0
  3. OH+H2<=>H+H2O                   2.16E+08   1.5    3430.0
     Reverse Arrhenius coefficients: 2.30E+09   1.4   18320.0
                          (etc)


NOTE:  A units mole-cm-sec-K, E units cal/mole


NO ERRORS FOUND ON INPUT:
ASCII Vers. 1.0 CHEMKIN linkfile chem.asc written.

WORKING SPACE REQUIREMENTS ARE
   INTEGER:    19885
   REAL:       12378
   CHARACTER:   124
Total CPUtime (sec):        7.66E-01
```

Figure 53. Truncated version of the "Chem.out" file after successful creation of the linking file

Therm.dat

The preferred source for thermodynamic data is the JANNAF Tables [91]. When the thermodynamic properties of certain species are not available in the JANNAF tables, they can be computed using ab-initio electronic structure calculations. The representation is loosely based on the format proposed by Gordon and McBride [92]. The thermodynamic data are stored as polynomial fits to specific heat, enthalpy, and entropy for two temperature ranges, as can be seen in the following equations:

$$\frac{c_p}{R} = a_1 + a_2 T + a_3 T^2 + a_4 T^3 + a_5 T^4, \tag{52}$$

$$\frac{H^0}{RT} = a_1 + \frac{a_2}{2} T + \frac{a_3}{3} T^2 + \frac{a_4}{4} T^3 + \frac{a_5}{5} T^4 + \frac{a_6}{T}, \tag{53}$$

and

$$\frac{S^0}{R} = a_1 \ln T + a_2 T + \frac{a_3}{2} T^2 + \frac{a_4}{3} T^3 + \frac{a_5}{4} T^4 + a_7. \tag{54}$$

Since the polynomials fit two temperature ranges, the temperature ranges need to be specified. Typically, the ranges are split at 1000 K, but this is not required and arbitrary temperature ranges may be chosen. An example of the thermodynamic format is shown in Figure 54 for H and H_2.

```
H                 120186H   1                G  0300.00   5000.00   1000.00        1
 0.02500000E+02  0.00000000E+00  0.00000000E+00  0.00000000E+00  0.00000000E+00   2
 0.02547163E+06-0.04601176E+01  0.02500000E+02  0.00000000E+00  0.00000000E+00    3
 0.00000000E+00  0.00000000E+00  0.02547163E+06-0.04601176E+01                    4
H2                121286H   2                G  0300.00   5000.00   1000.00        1
 0.02991423E+02  0.07000644E-02-0.05633829E-06-0.09231578E-10  0.01582752E-13     2
-0.08350340E+04-0.01355110E+02  0.03298124E+02  0.08249442E-02-0.08143015E-05     3
-0.09475434E-09  0.04134872E-11-0.01012521E+05-0.03294094E+02                     4
```

Figure 54, Example of thermodynamic data used in the "therm.dat" file for H and H₂

Chem.bin

Chem.bin is a binary linking file that can only be opened inside the user's code. This linking file contains all the pertinent information about the input mechanism, including the thermodynamic data from the therm.dat file.

Tran.exe

Laminar premixed flames are a strong function of the mixture's transport properties. It is therefore important to evaluate the mass diffusivity, thermal diffusivity, conductivity, and to a lesser extent the viscosity of each species involved in the combustion process. Computing ordinary multi-component diffusion coefficients is computationally expensive and involves inverting a K x K matrix, where K represents the number of species. Also, evaluating the conductivity and thermal diffusion of a multi-component mixture is not trivial and requires solving a 3K x 3K system of equations.

Tran.exe takes the fundamental collision parameter for each species and uses these to calculate the transport properties per species. These transport properties are then fitted via polynomials that can be called upon at any time by a particular FORTRAN

subroutine. Doing this allows for much of the computations to be completed beforehand, thus saving valuable computational time during the calculations.

The single component viscosities are given by the standard kinetic theory expression [93]

$$\mu = \frac{5}{16} \frac{\sqrt{\pi m_i k_B T}}{\pi \sigma_i^2 \Omega^{(2,2)*}} \tag{55}$$

Were σ_i is the Lennard-Jones collision diameter, m_i is the molecular mass, k_B is the Boltzman constant, and T is the temperature. The collision integral $\Omega^{(2.2)*}$ depends on the reduced temperature and on the molecule's polarity.

The binary diffusion coefficient is given as a function of pressure and temperature so that

$$D_{i,j} = \frac{3}{16} \frac{\sqrt{2\pi k_B^3 T^3/m_{ij}}}{P\pi \sigma_{ij}^2 \Omega^{(1,1)*}} \tag{56}$$

where m_{ij} is the reduced molecular mass given as

$$m_{ij} = \frac{m_i m_j}{m_i + m_j} \tag{57}$$

The mixture conductivity is an important property since it defined how fast the unburned reactants can be heated to the required ignition temperature. In CHEMKIN, the conductivities of pure species are calculated first, which are then used to evaluate the mixture's conductivity. Warnatz [94] proposed the conductivities of pure species to be composed of translational, rotational and vibrational contributions, so that

$$\lambda_i = \frac{\mu_i}{m_k}\left(f_{trans.}C_{v,trans.} + f_{rot.}C_{v,rot.} + f_{vib.}C_{v,vib.}\right) \tag{58}$$

As said before, the transport properties are fitted in a polynomial fashion where the logarithm of a property is plotted versus the logarithm of the temperature, as shown in the following equations:

$$\ln \mu_i = \sum_{n=1}^{K} a_{n,i}(\ln T)^{n-1} \tag{59}$$

$$\ln \lambda_i = \sum_{n=1}^{K} b_{n,i}(\ln T)^{n-1} \tag{60}$$

and

$$\ln D_{ij} = \sum_{n=1}^{K} d_{n,ij}(\ln T)^{n-1} \tag{61}$$

By default, N = 4 and the fitting errors are well within one percent.

The mixture-averaged properties are not only important with the numerical routines, but also serve to calculate experimentally obtained properties such as the Reynolds number and Peclet number, both of which are defined in the next chapter. CHEMIKIN uses the semi empirical formula due to Wilke [95] and modified by Bird et al. [96]. The mixture viscosity is then given by:

$$\mu = \sum_{k=1}^{K} \frac{X_k \mu_k}{\sum_{j=1}^{K} X_j \Phi_{kj}}$$ (62)

In equation (62), Φ_{kj} depends on the pure species viscosities and the molecular mass per species.

The mixture's conductivity can more easily be found by using the averaging formula given by Mathur et al. [97].

$$\lambda = \frac{1}{2} \sum_{k=1}^{K} X_k \lambda_k + \frac{1}{K \sum_{k=1}^{K} X_k / \lambda_k}$$ (63)

4.2   Premix.exe

All numerical laminar flame predictions were created using "PREMIX: A Program for Modeling Steady, Laminar, One-dimensional Premixed Flames" developed by Kee et al. [98]. PREMIX computes species and temperature profiles in steady state, burner

stabilized, and freely propagating premixed laminar flames. The program accounts for finite rate chemical kinetics and multi-component molecular transport as described above. The governing equations form a boundary value problem solved using finite-difference discretization and the Newton method. PREMIX requires both the chemical linking file created by "chem.exe" and the processed transport properties created by "tran.exe".

Chapters I and II introduced the laminar flame speed for describing the principal combustion process inside a gas-turbine combustor and an internal combustion engine. Moreover, laminar premixed flames are often used to study chemical kinetics in a combustion environment characterizing the combustion of various fuel-oxidizer combinations. The ability to model chemical kinetics and transport processes in these flames is critical to interpreting flame experiments such as those conducted in this study.

PREMIX is largely based on the implicit finite difference methods introduced by Spalding [99] and the finite-difference-boundary-value-problem techniques introduced by Wilde [100] and Kendall and Kelly [101] for solving the steady state problem directly. The flame configuration used in this study is the freely propagating adiabatic flame. In this case there are not heat losses and the temperatures are calculated from the energy equation. Predicting the temperature profile is fundamental in predicting laminar flame speed due to its dependence on thermal diffusivity.

Steady, one-dimensional, flame propagation can be described by the following equations:

Continuity:
$$\dot{m} = \rho u A$$

(64)

Energy:
$$\dot{m}\frac{dT}{dx} - \frac{1}{c_p}\frac{d}{dx}\left(\lambda A \frac{dT}{dx}\right) + \frac{A}{c_p}\sum_{k=1}^{K}\rho Y_k V_k c_{p,k}\frac{dT}{dx} + \frac{A}{c_p}\sum_{k=1}^{K}\dot{\omega}_k h_k W_k = 0$$

(65)

Species:
$$\dot{m}\frac{dY_k}{dx} + \frac{d}{dx}\left(\rho A Y_k V_k\right) - A\dot{\omega}_k W_k = 0$$

(66)

Equation of State:
$$\rho = \frac{p\overline{W}}{RT}$$

(67)

In the above equations, x denotes the spatial coordinate, $\dot{M}$ the mass flow rate, Y_k the mass fraction, ρ is the mass density, W_k is the molecular weight of the kth species, $\overline{W}$ the mean molecular weight of the mixture, R is the universal gas constant, c_p is the specific heat of the mixture, $c_{p,k}$ is the specific heat of species k, $\dot{\omega}_k$ is the molar rate of production, h_k is the specific enthalpy of the kth species, V_k is the diffusional velocity, and A is the cross sectional area of the stream tube encompassing the flame.

There are two different options regarding the treatment of molecular diffusion. One is using mixture-averaged properties for the mass diffusivities. Resulting in K number of diffusion coefficients D_{km}, where K is the number of species present in the problem and D_{km} is the diffusion coefficient of species k with respect to the mixture m. Alternatively, multi-component diffusion coefficients can be used requiring K x K number of

coefficients. Multi-component or mixture-averaged diffusion can be selected by inclusion of "MULT" or "MIX" keywords in the input file.

Boundary conditions are important for the solution to converge. Since the mass flow rate $\dot{m}$ is an eigenvalue and part of the solution of a freely propagating flame, an additional boundary condition is required. This is done by fixing the flame at a specific location. This can be done by specifying the temperature of the flame at a specific location. In this study the flame is "anchored" to the spatial grid at a temperature of 400 K. An example of a PREMIX input file as used in this study can be found in appendix J.

4.3 Mechanisms Used

GRI 3.0

The Gas Research Institute's (GRI) 3.0 is an optimized mechanism created by Smith et al. [26] designed to model natural gas combustion. The mechanism includes the formation of NOx and reburns chemistry. GRI is a continuous effort building on previous versions. The optimization process is designed to provide sound basic kinetics combined with the capabilities to predict basic combustion properties. The mechanism is developed in the following fashion.

First a full mechanism is created using consistent treatment of pressure and temperature dependencies. Second, reliable experimental data related to natural gas combustion and NO formation is collected. These experiments include shock-tube ignition delay measurements [102]-[105], shock-tube species profile measurements [106]-[110], laminar flame speed measurements [66], [69], as well as prompt NO,

reburn, and HCN oxidation. Third, a computer code is used to predict the target experimental values including a sensitivity analysis of the predicted values with respect to the reaction rate coefficients.

Finally, a response surface is created after factorial-design-directed calculations. This response surface is used to calculate target values that are then compared to measured values.

The sensitivity with respect to the thermodynamic properties was computed for all targets by changing coefficient a_6 in equation (53). In general, selected targets did not show significant sensitivity to species enthalpy with exception of HCN, the value of which was altered accordingly.

The final mechanism contains 325 reactions and 53 individual species and will be used in the following chapter to model the data obtained in this study.

C5-mechanism

The C5 mechanism used in this study is created at the Combustion Chemistry Center, C^3, located at the National University of Ireland, Galway (NUIG). The Combustion Chemistry Center is engaged in fundamental research on the combustion of fossil and biofuels. Currently a hydrogen, methylcyclohexane, di-isobutylene, natural gas 2006/07, natural gas to/including C5 2007/08, biofuels, acetone, and butane mechanism is available for download from the Combustion Chemistry Center website, http://www.nuigalway.ie/chem/c3/mechanisms.htm. The natural gas mechanism is a result of long cooperation between the NUIG and Texas A&M University [15], [111], [112]. Experimental data used to provide target data for model optimization is created

via shock-tubes, a rapid compression machine, and the flame speed facilities as described in this study.

The detailed chemical kinetic model is based on the hierarchical nature of hydrocarbon combustion mechanisms containing the H_2/O_2 sub-mechanism, together with the CO/CH_4 and larger hydrocarbon sub-mechanisms. The mechanism is similar but not identical to previous work on methane/propane mixtures [113]. Some of the major changes include new rate constants for the $H + O_2 \rightarrow O + OH$ reaction [114], the $CO + HO_2$ reaction [114], the $CH_4 + O_2 \rightarrow CH_3 + HO_2$ reaction, the $CH_3 + HO_2 \rightarrow CH_3O + OH$ reaction, and finally the $C_2H_6 + H \rightarrow C_2H_5 + H_2$ rate constant was taken from the GRI 3.0 [26].

Sensitivity analysis has shown that ignition delay times of methane, ethane, and propane fuels are very sensitive to the rate constant for the decomposition of ethyl radicals to ethylene and H atoms, and the rate constant was cut in half with respect to the value previously reported [113].

Originally, the natural gas mechanism used in this study included C_4 and C_5 chemistry based on the reaction rate rules presented in the work on the primary reference fuels published by Curran et al. [115], [116]. In order to reduce computational times, the C_4 and C_5 sub-mechanisms were removed since only alkanes up to propane are considered in this study. The potential of forming higher order alkanes such as butane and pentane via recombination reactions seem unlikely in the high-temperature reaction zone of the flame. Furthermore, some low-temperature kinetics such as addition of alkyl radicals to molecular oxygen is no longer important. Therefore, in modeling flame speed

measurements a "high-temperature" mechanism was subtracted from the full original mechanism. The original C_5 mechanism includes 1580 reactions and 289 individual species. After removal of the C_4 and C_5 sub-mechanisms and the low-temperature chemistry, the mechanism is reduced to 465 species and 76 individual species.

CHAPTER V

RESULTS

5.1   Methane Results

Many measurements exist for mixtures of methane with air. These measurements include counterflow flames, the heat flux method, and freely propagating spherically expanding flames similar to those used in this study. Data obtained in this study were temperature corrected to 298 K. A stainless steel, K-type thermocouple probe inserted into the flame speed bomb allowed for temperature measurements of the unburned reactants. All data shown in this study are corrected via the following correlation.

$$S_{L,u}^0 = \left(\frac{298}{T}\right)^{1.85} S_{L,u,measured}^0 \tag{68}$$

In equation (68), T is the measured temperature. The value for the exponential factor of 1.85 was taken from Gu et al. 0.

Figure 55 shows the results for methane/air at 1 atm compared against other studies and three chemical kinetic mechanisms: GRI 3.0 [26], Curran's C_5 mechanism [115], [116], and one additional mechanism developed for atmospheric methane/air mixtures at the University of California, San Diego. The San Diego mechanism, created by Petrova and Williams and coworkers [117], is designed for auto-ignition, deflagration, detonation, and diffusion flames. This mechanism includes 46 species and 235 reactions,

which makes it comparatively small. Working with a smaller mechanism can potentially

facilitate numerical analysis, including sensitivity analysis with respect to several input

parameters. In Figure 55, the data obtained in this study are expressed by the solid black

squares.
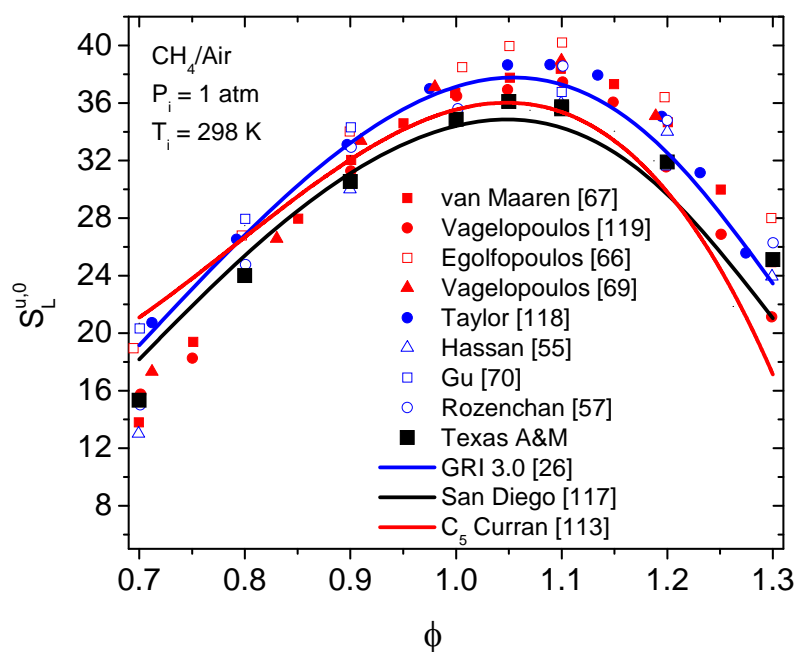
Figure 55. Atmospheric methane/air experimental results and modeling

Figure 55 shows some scatter between reported data with flame speeds at $\phi = 1.0$

ranging between 34.8 cm/s obtained in this study to 38.5 cm/s found by Egolfopoulos et

al. [66]. Burner methods are represented with red symbols and freely propagating flames

with blue. The particular bias of flame speed result does not seem to depend on

experimental technique. Data obtained in this study agree well with values obtained by

other experiments ([55], [57], 0, [66], [67], [69], [118], and [119]). Of the three models

used in this study, GRI 3.0 [26] agrees well with the data found by Vagelopoulos et al.

[69], which is the dataset used to optimize this model. All three mechanisms predict

higher flame speeds than found in this study for the fuel lean mixtures, agreeing closer

with data obtained by Taylor [118], Egolfopoulos et al. [66], Gu et al. 0, and Rozenchan

et al. [57]. Curran's C_5 mechanism [113] agrees well with this study at stoichiometric

conditions and under-predicts the data in the fuel rich regime.
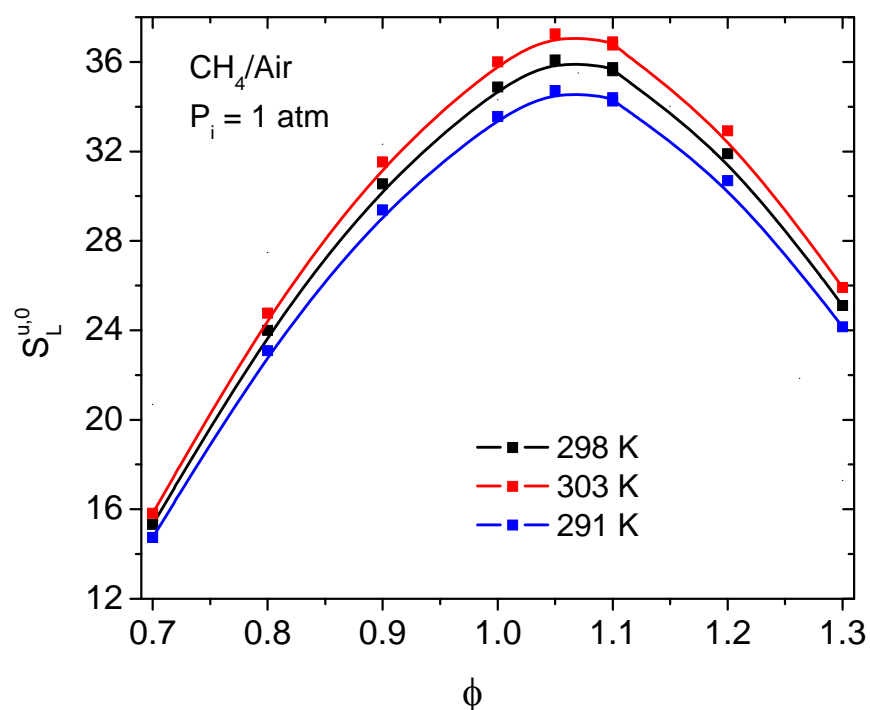
Figure 56. Initial temperature effects on measured flame speed based on the correlation given by Gu et al. 0, (equation 68)

Figure 56 shows the effect of initial temperature on the reported flame speed and the

importance of a local temperature measurement before each experiment. Measured

temperatures did not necessarily match room temperature. In the case of a constant volume bomb, the vessel might still be warmer than room temperature due to a prior experiment.
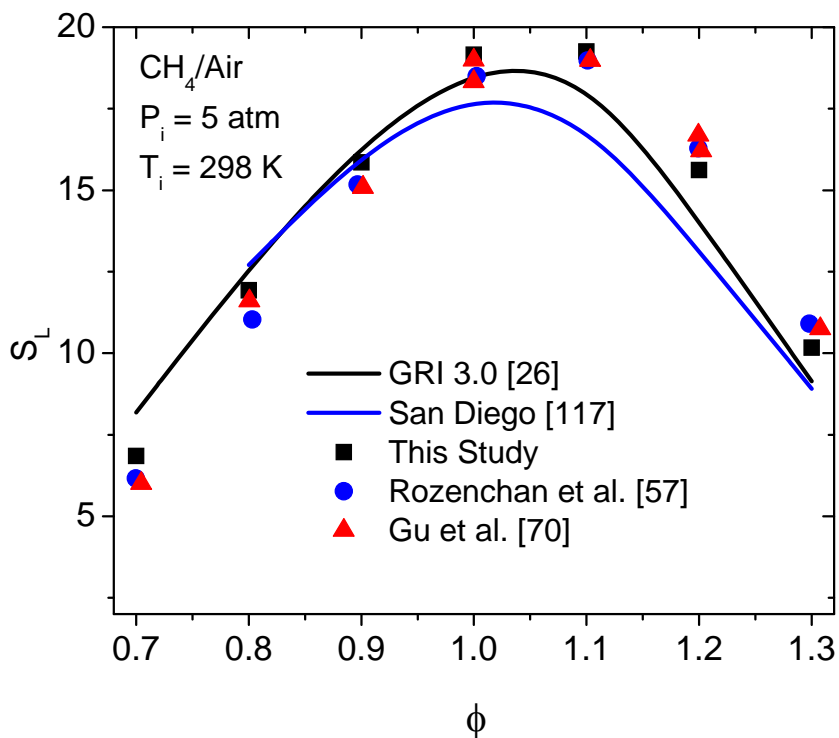
Figure 57. 5 atm methane/air experiments and modeling

Figure 57 shows experimental results for methane/air mixtures at 5 atm. Close agreement is seen with data from Rozenchan et al. [57] and Gu et al. 0. Also, GRI 3.0 [26] agrees well with flame speeds obtained at 5 atm. However, C_5 mechanism severely under-predicts the data and improvement is necessary for this model in the stoichiometric and fuel rich regime. Similar under-predictions are seen at 10 atm for fuel rich mixtures in Figure 58.

Figure 58 shows the experimental results for 10 atm methane/air mixtures. Again, good agreement is seen with the results obtained by Rozenchan et al. [57] and Gu et al. 0. GRI 3.0 0 agrees well with the experimental data, slightly over predicting fuel lean mixtures.
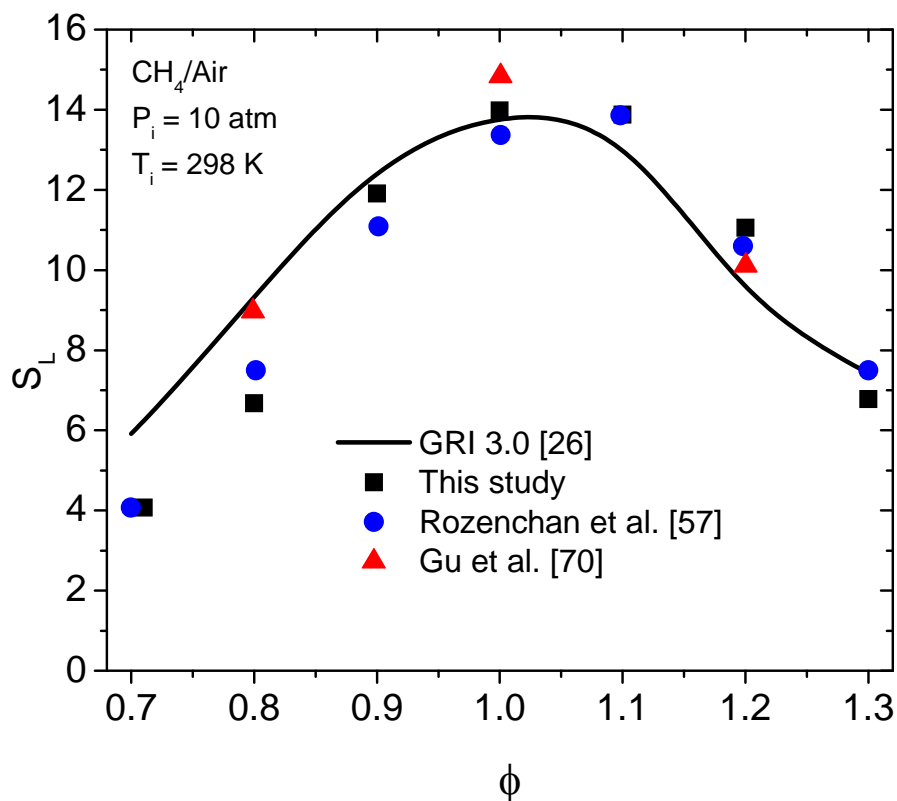
**Figure 58. 10 atm methane/air experiments and modeling**

Figure 59 shows the modeled mole fractions across a methane/air flame at fuel rich condition, $\phi = 1.2$. Mole fractions of GRI 3.0 and Curran's C_5 mechanisms are compared. OH and CH_3 are multiplied by 100 in Figure 59. Formation of OH radicals

with GRI 3.0 is double to that predicted by Curran's C_5 mechanism. Since OH chemistry is principally responsible for most of the chain branching reactions, lacking OH could be one of the causes of under predictions seen at fuel rich mixtures in Figure 57 and Figure 58.
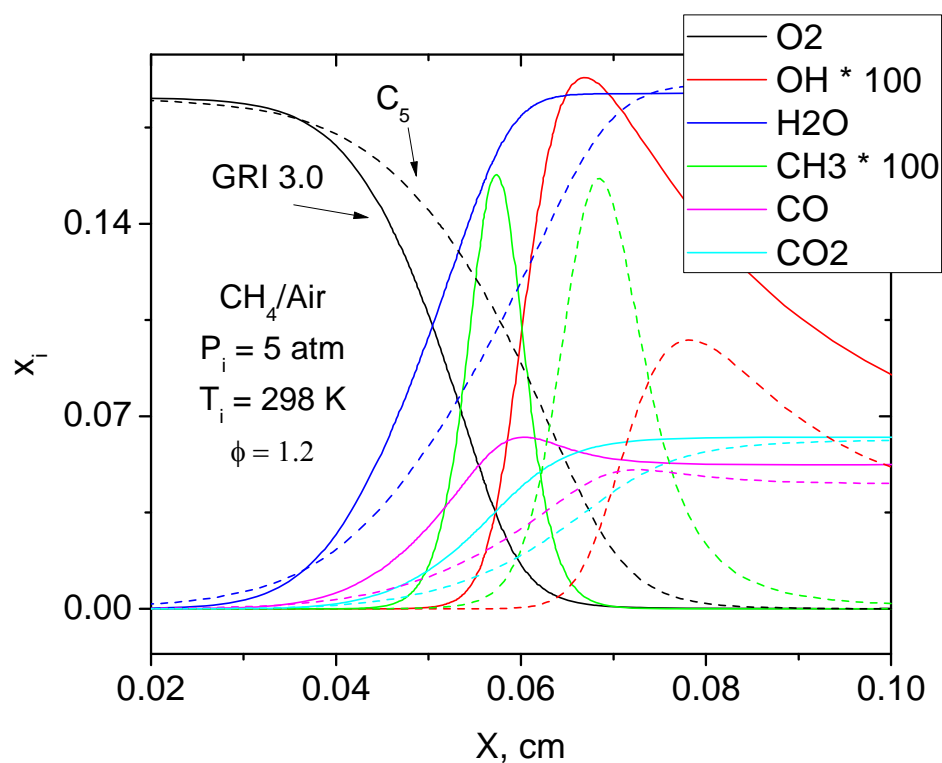
Figure 59. Mole fraction across a 5 atm methane/air flame, GRI 3.0 in solid lines versus C_5 in dashed lines

Figure 60 shows the pressure effect on laminar flame speeds for methane/air mixtures versus equivalence ratio. Increasing the pressure from 1 to 5 atm decreases the flame speed significantly. Further reduction is seen when increasing the pressure to 10 atm.
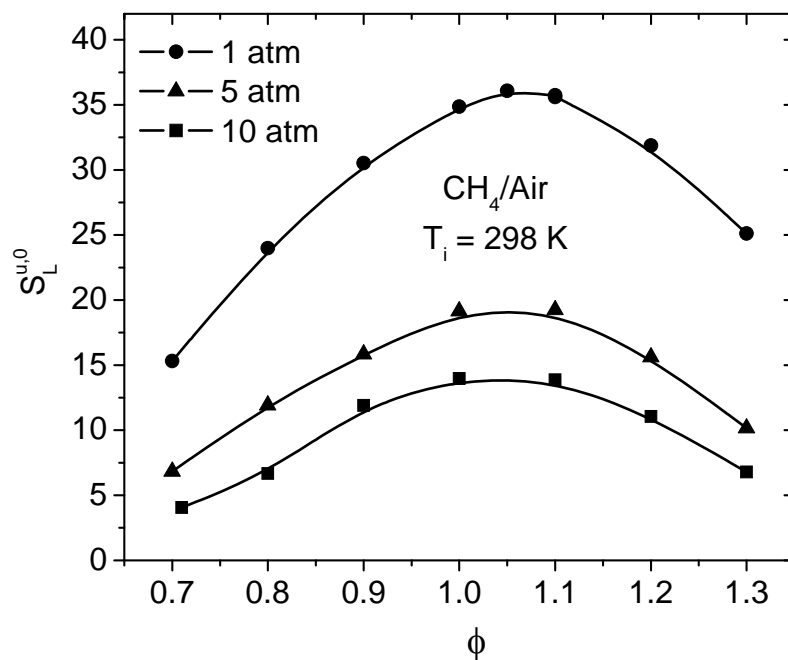
Figure 60. Flame speed of methane/air mixtures at 1, 5 and 10 atm

The results obtained for methane/air mixtures are consistent with the results obtained by other researchers [55], [57], 0, [66], [67], [69], [118], and [119]. At 5 and 10 atm, good agreement is seen with Rozenchan et al. [57] and Gu et al. [57]. Curran's C_5 mechanism predicts flame speeds sufficiently well at atmospheric conditions. However, at 5 and 10 atm the C_5 mechanism at the time of the writing of this thesis considerably under-predicts the measured values at stoichiometric and fuel rich conditions.

5.2   Ethane Results

Measurements of ethane/air flames are less common than methane/air flames. Figure 61 shows the results from this study compared against counterflow measurements by Egolfopoulos et al. [66] and Vagelopoulos et al. [69], heat flux measurements by Boschaart et al. [71] and Konnov et al. [72], and spherical expanding flames by Jomaas et al. [73].
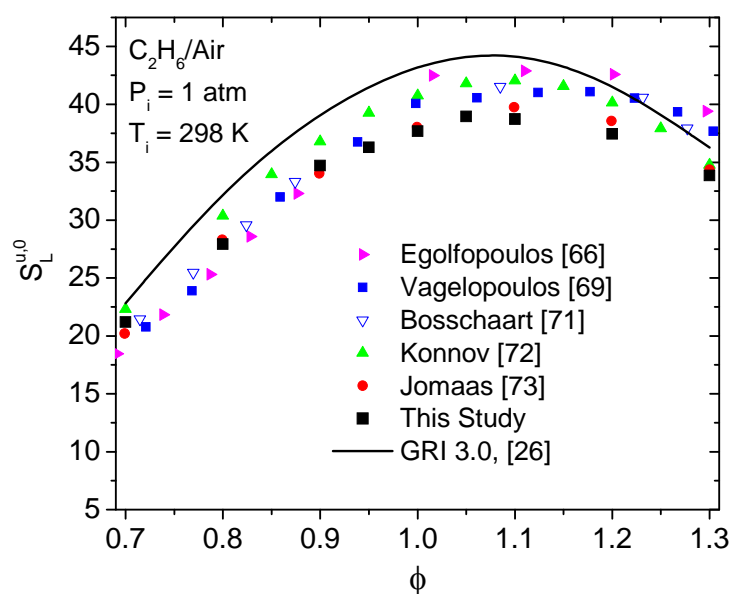
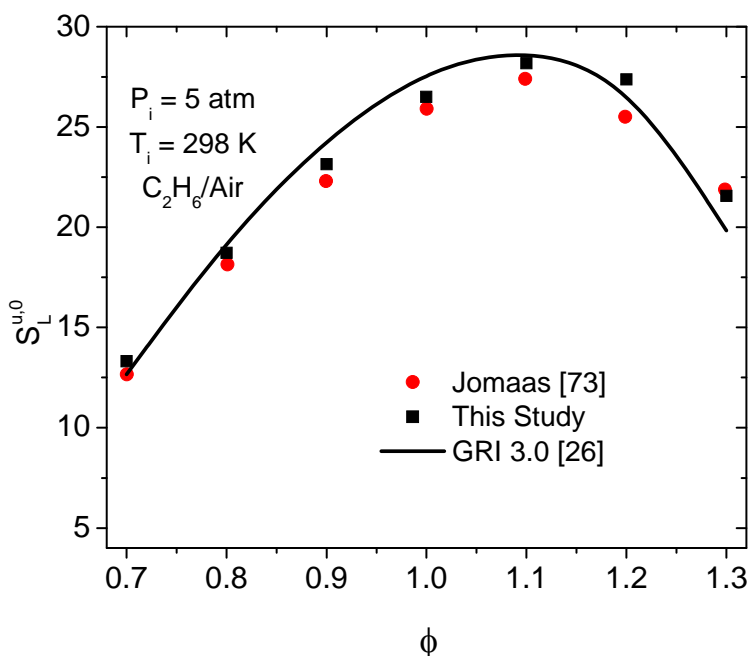**Figure 61. Flame speed of ethane/air mixtures at 1 atm, experiment and modeling**

Similar to the methane/air results, ethane/air data obtained in this study agrees with the lower range of reported measurements. Spherical expanding flame measurements by Jomaas et al. [73] agree particularly well with those obtained in this study. GRI 3.0 [26] agrees well at fuel rich conditions and over-predicts the data at stoichiometric and fuel

lean conditions. Curran's C_5 mechanism shows similar trends for ethane/air as for methane/air flames with fuel rich flame speeds greatly under-predicted.

Laminar flame speed measurements of ethane/air above atmospheric conditions are rare. Figure 62 shows experimental ethane/air flames at 5 atm compared against the measurements by Jomaas et al. [73]. GRI 3.0 [26] results agree unexpectedly well with the experimental data, since high pressure ethane data were not used as target data for this model.

Figure 62. Flame speed of ethane/air mixtures at 5 atm, experiment and modeling

Curran's C_5 mechanism under-predicts the 5 atm ethane/air data as well as the 10 atm data shown in Figure 63. At 10 atm, GRI 3.0 [26] under-predicts at fuel rich conditions to a smaller extend. Figure 63 shows that there are no other measurements of 10 atm ethane/air flames available for comparison.
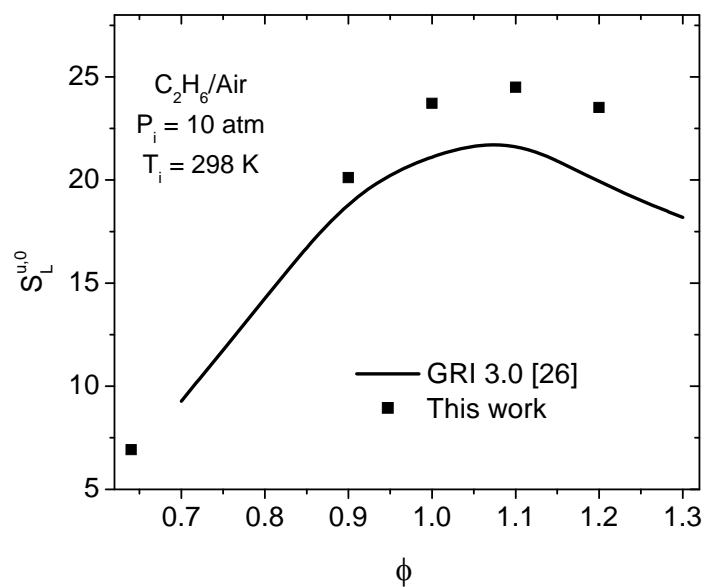
Figure 63. Flame speed of ethane/air mixtures at 10 atm, experiment and modeling

Pressure effects for ethane/air and methane/air mixture are different as shown in Figure 64 and Figure 65. Figure 64 shows laminar flame speed of methane/air and ethane/air mixtures plotted from 1 to 10 atm. Exponential relationships are shown that best fit the data. Pressure dependency of methane is approximately double that of ethane with exponents of 0.393 and 0.204, respectively.
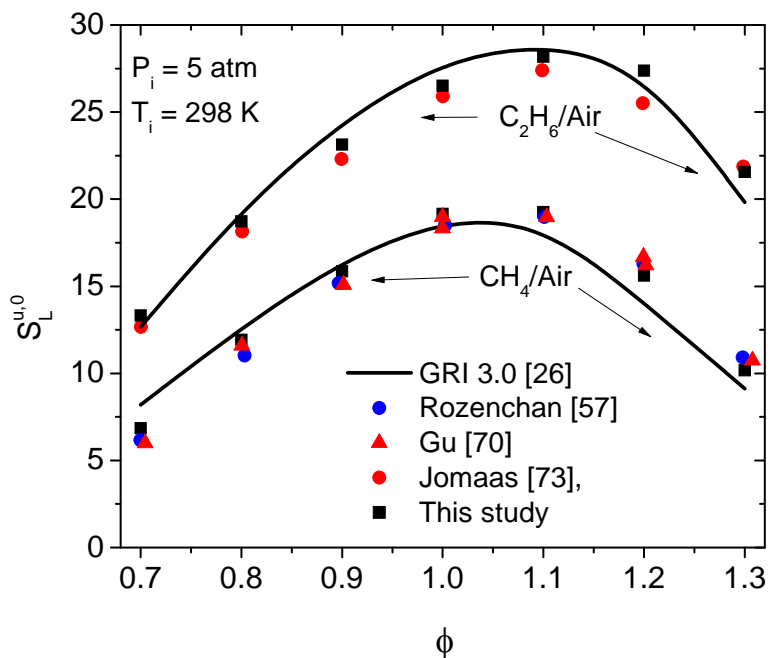
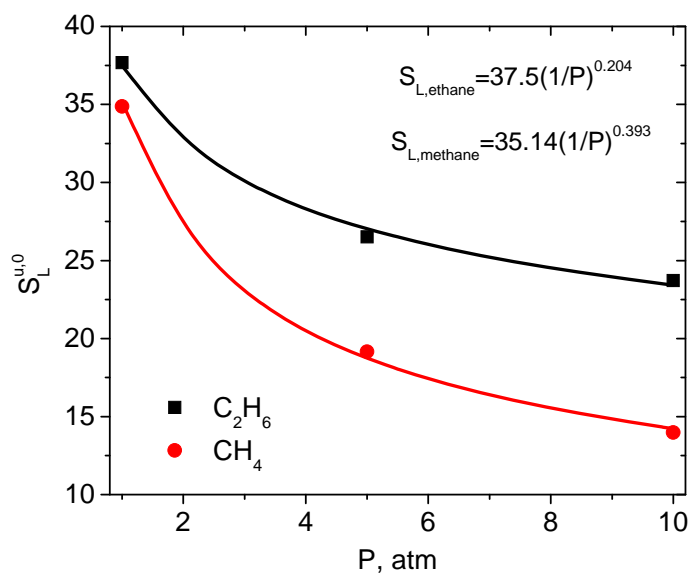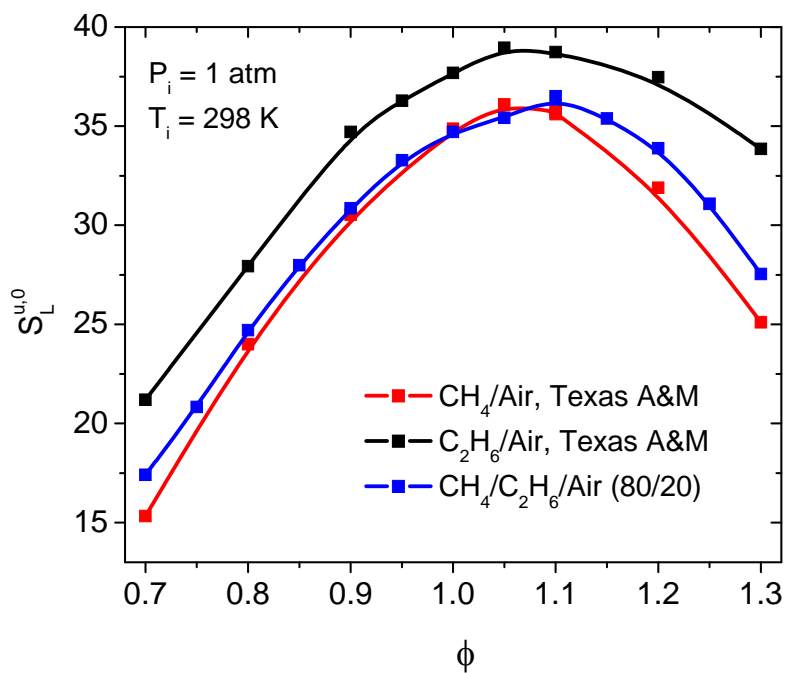**Figure 64. Methane/air and ethane/air versus equivalence ratio at 5 atm**

Figure 65. Flame speed versus pressure for ethane/air and methane/air mixtures

5.3 Methane/Ethane Results

The most common alkane in natural gas besides methane is ethane, and percentages of 20% or more of ethane are not uncommon in natural gas. The first binary mixture used in this study consists of 20% ethane and 80% methane. Prior studies showed an acceleration of auto-ignition times by a factor of six or more for methane mixtures doped with ethane. Since flame speed chemistry takes place in the high temperature region and due to the additional importance of the reactant's transport properties, similar strong effects are not expected for methane/ethane flame speeds. However, Figure 64 and Figure 65 show that ethane flames are faster than methane flames by a factor of approximately two at ten atm. Figure 66 shows experimental flame speed results for methane/air, ethane/air, and methane/ethane/air (80/20) mixtures at 1 atmosphere. Prior to this study, flame speeds of binary methane/ethane fuel mixtures have not been investigated.

Figure 66 shows that 20% ethane moderately accelerates laminar flames at fuel lean conditions and shows acceleration in the fuel rich regime. At 1 atm, methane/ethane mixtures remain close to the results obtained for pure methane. At stoichiometric conditions, the results of both methane/air and methane/ethane/air mixtures fall within each other's experimental uncertainty.

Figure 66. Methane/air, ethane/air, and methane/ethane/air mixtures at 1 atm versus equivalence ratio

A distinct difference in flame speed is seen for the same mixtures at 5 atm in Figure 67. Figure 67 and Figure 68 show flame speed results at 5 and 10 atm, and the modeled results from GRI 3.0 [26]. GRI 3.0 agrees with all 5 atm data and 10 atm data except for 10 atm 100% ethane, where the model under predicts the experimental results.
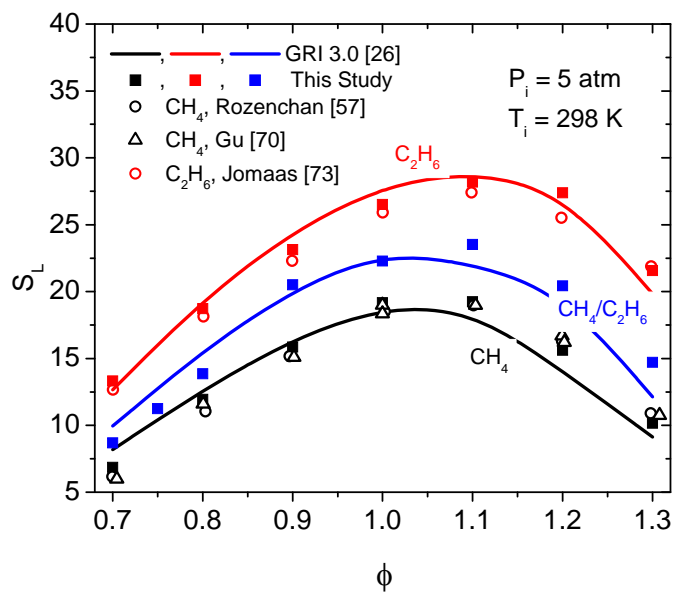
Figure 67. Methane/air, ethane/air, and methane/ethane/air mixtures at 5 atm versus equivalence ratio
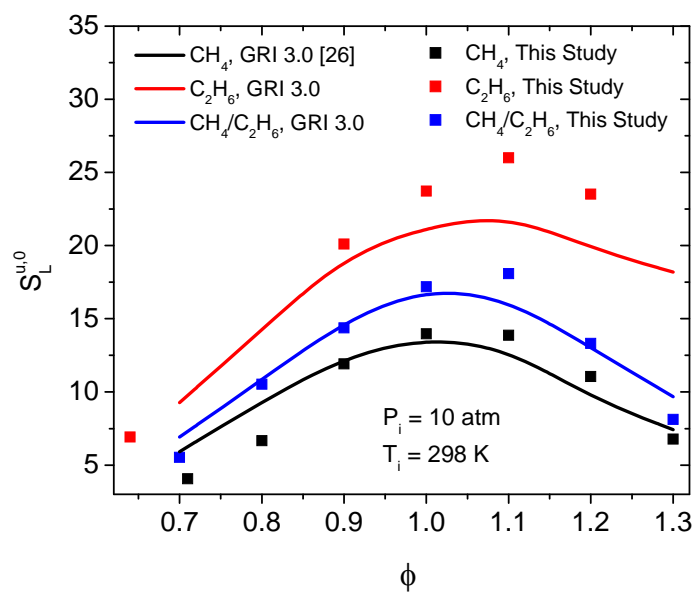
Figure 68. Methane/air, ethane/air, and methane/ethane/air mixtures at 10 atm versus equivalence ratio

Figure 69 shows the pressure effect from 1 to 10 atm for methane/air, ethane/air, and methane/ethane/air (80/20) mixtures. The trend diverges with increasing pressure. At 10 atm, ethane/air flames are 70% faster than methane/air flames. The binary mixture of methane/ethane (80/20) is 21% faster at 10 atm compared to 100% methane flames.
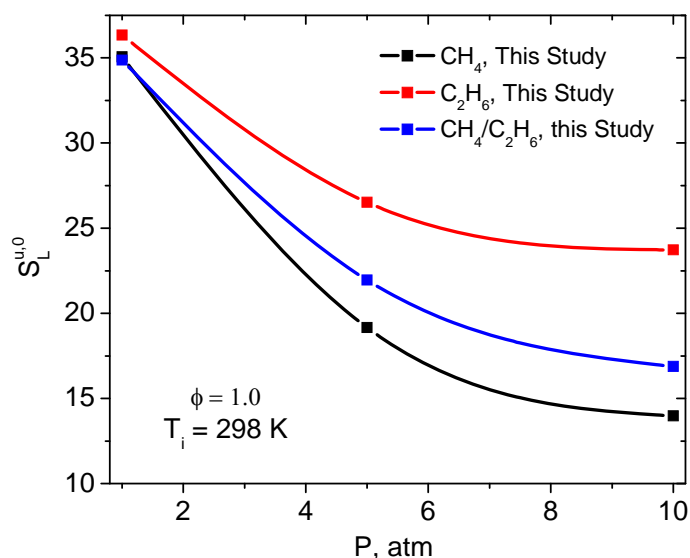
Figure 69. Flame speed versus pressure for ethane/air, methane/air, and methane/ethane/air (80/20) mixtures

For each mixture, the adiabatic flame temperature is calculated using the equilibrium code by W.C. Reynolds [120]. For 1 and 10 atm, the adiabatic flame temperatures are plotted against equivalence ratio and are shown in Figure 70. Adiabatic flame temperatures of the ethane/air mixture are slightly higher than methane/air mixtures. Figure 71 shows the flame speed of methane/air, ethane/air, and methane/ethane/air (80/20) mixtures versus adiabatic flame temperatures. For similar flame temperatures,

ethane flames remain faster than methane flames indicating that the acceleration is due to either chemical kinetic effects or changes in transport properties.
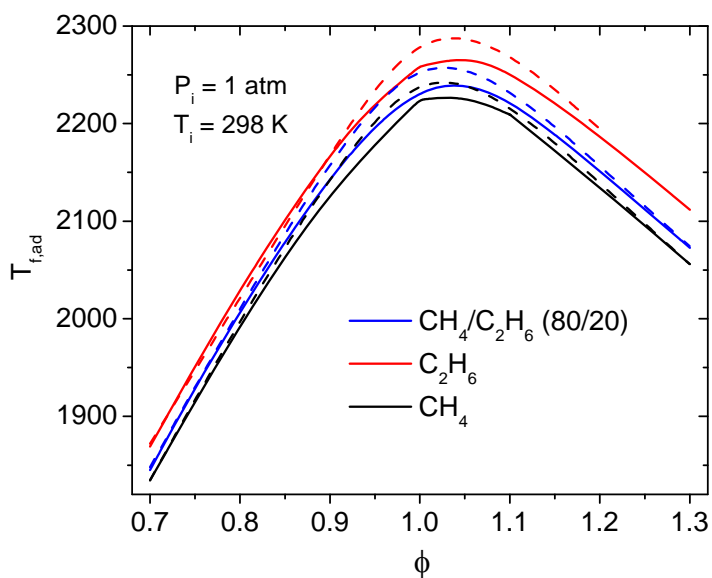
Figure 70. Adiabatic flame temperature versus equivalence ratio for mixtures used in this study
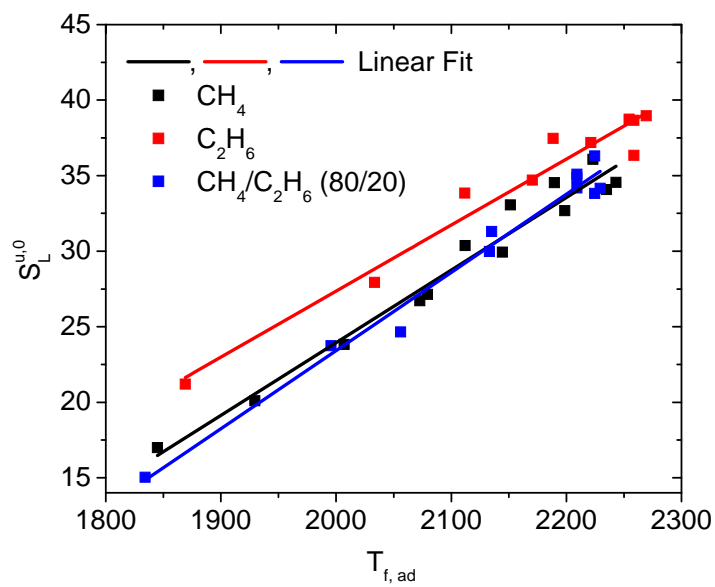
Figure 71. Flame speed versus adiabatic flame temperature showing ethane flame acceleration due to chemical and diffusive effects

5.4   Stretch Effects and Flame-Front Instabilities

Spherically expanding flame speeds depend on the flame stretch which was defined in Chapter II as $\alpha = 2/R_f\, dR_f/dt$. The slope is expressed as the Markstein length, Lm.
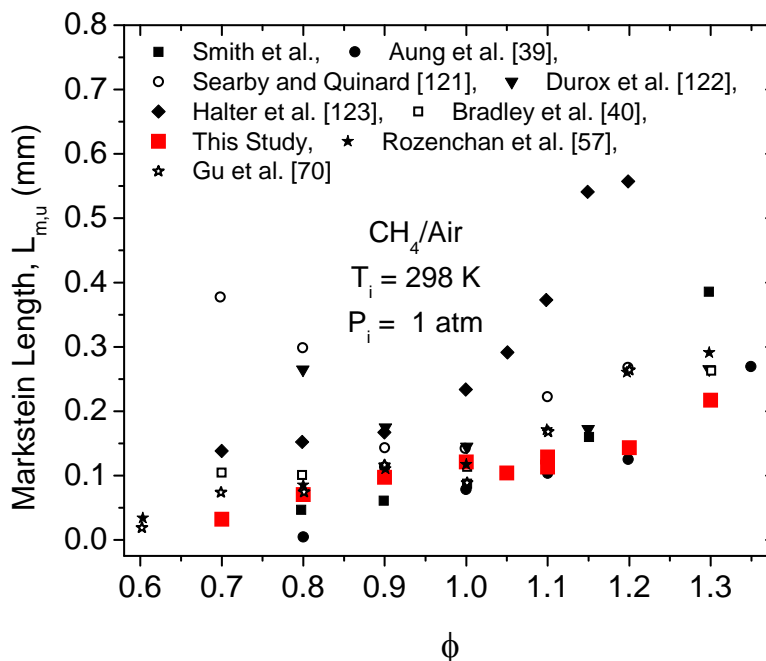
Figure 72. Markstein length for methane/air at 1atm, results by other researchers are shown

Figure 72 shows reported Markstein lengths obtained by several researchers for atmospheric methane/air flames. Markstein lengths obtained in this study are represented by solid red squares.   Reported Markstein lengths show a large variance between reported values both in magnitude and trend. In general, Markstein lengths increase from lean to rich conditions with the exception of the results by Searby and Quinard [121] and Durox et al. [122], which show decreasing flame stretch dependency from lean to rich conditions.
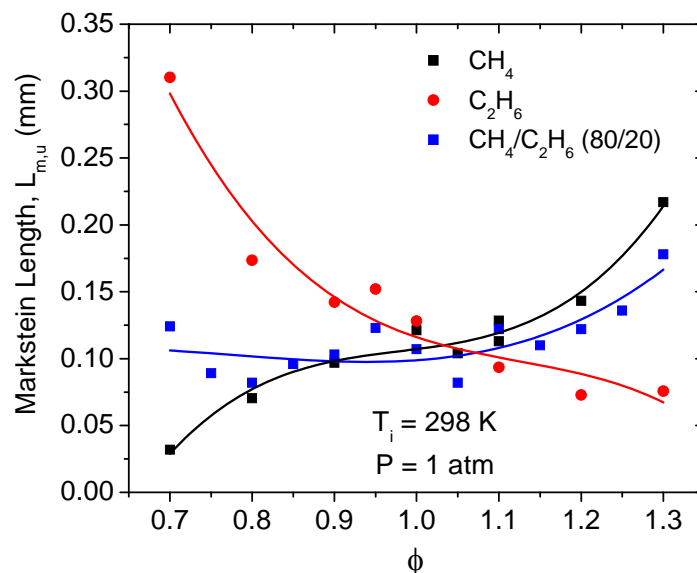
Figure 73. Markstein lengths for atmospheric methane/air, ethane/air, and methane/ethane/air

(80/20)

Figure 73 shows experimentally obtained Markstein lengths for atmospheric methane/air, ethane/air, and methane/ethane/air (80/20) versus equivalence ratio. Ethane/air mixtures show a reverse trend with the Markstein length decreasing with increasing equivalence ratio. Binary mixtures of methane and ethane (80/20) show an oscillating trend and approach the pure methane results at fuel rich conditions.

Markstein lengths for methane/air mixtures at 1, 5, and 10 atm are plotted against equivalence ratio in Figure 74. Markstein length decreases with increasing pressure and can become negative for high-pressure, lean mixtures.
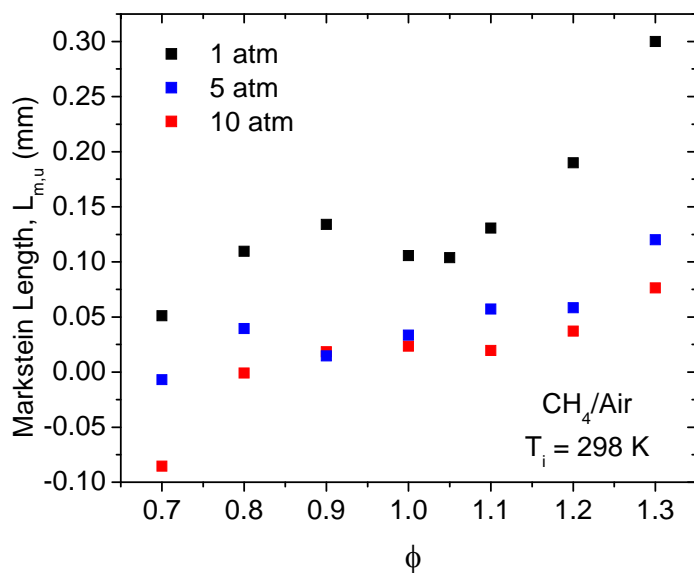
Figure 74. Markstein length for methane/air at 1, 5, and 10 atm
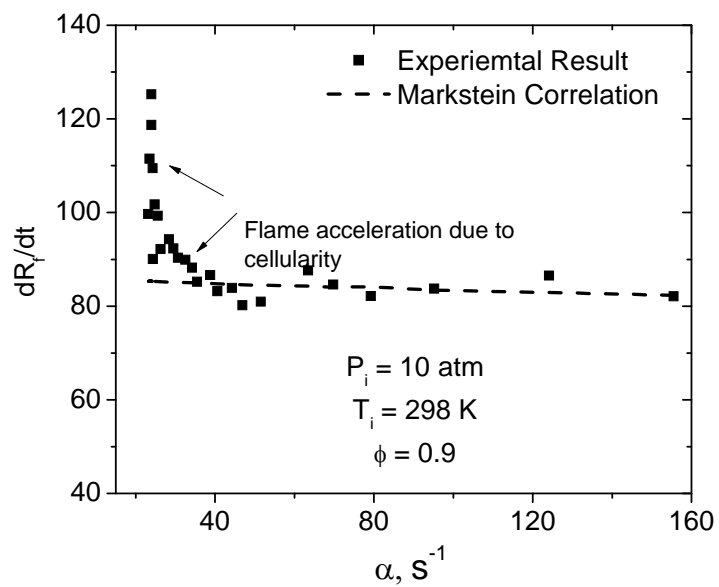
Figure 75. Flame speed versus flame stretch, acceleration due to the onset of cellularity clearly visible

At elevated pressures, flames tend to become unstable or cellular, increasing the flame speed in the process. The main mechanism for flame acceleration is the increased surface area caused by the non-uniform flame front. Figure 75 shows the flame speed versus flame stretch for methane/air at 10 atm. Flame radius increases from right to left in Figure 75.

Figure 76 shows flame images from stoichiometric methane/air at 1, 5, and 10 atm. Cellular flame fronts are observable for methane/air flames at 10 atm. At 1 atm, the flame remains laminar with only minor discrepancies found around the electrodes. At 5 atm, large scale instabilities are growing self-similarly until at larger radii new cracks are formed eventually leading to a fully cellular flame structure. At 10 atm, self-similar large scale cracks are seen, comparable to the 5 atm experiment. When the flame radius reaches approximately 3 cm, a transition occurs, and at 4 cm the flame's surface is entirely cellular.

1 atm   **5 atm**   `   **10 atm**
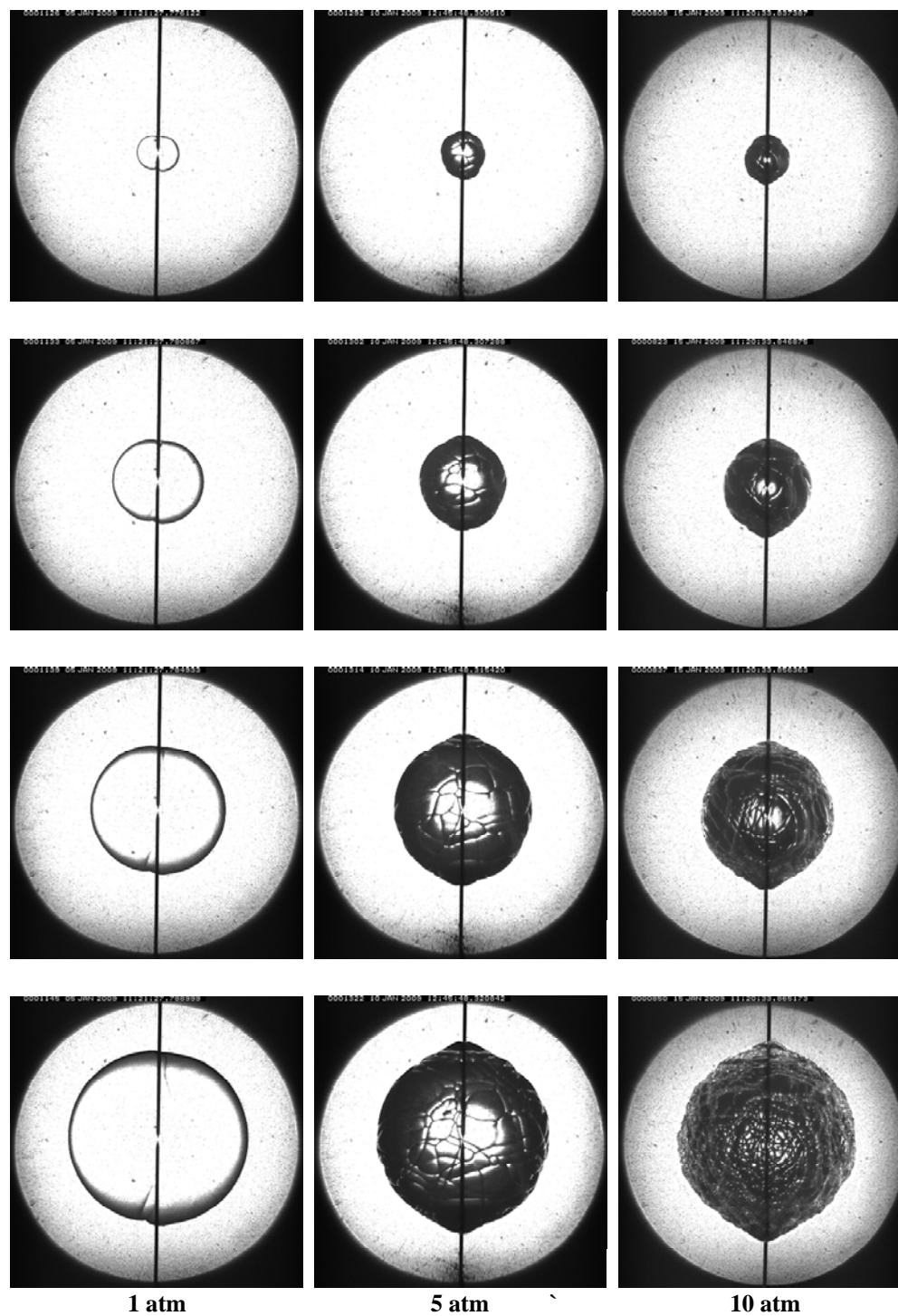
Figure 76. Methane/air flames at 1, 5, and 10 atm shown at radii of 1, 2, 3, and 4 cm, respectively

Figure 77 shows the flame radius versus time for methane/air at 10 atm. Transition to a cellular flame structure visibly leads to flame acceleration. Data for determining the laminar flame speed is taken up to this acceleration. This effect can be made better visible by subtracting the Markstein correlation (equation 22) from the experimentally obtained radii and plotting the residuals. Figure 78 and Figure 79 show residuals for methane/air flames at 10 and 1 atm, respectively. Figure 78 shows that the residuals are initially randomly distributed until, after 30 ms, they visibly increase for the cellular flame. Figure 79 shows that for low pressure laminar flames, the residuals remain randomly distributed throughout the experiment with a mean of approximately zero and a standard deviation of 0.0074 cm. Additionally, a histogram shown in Figure 80 shows the normal distribution for residuals of atmospheric methane/air flames.
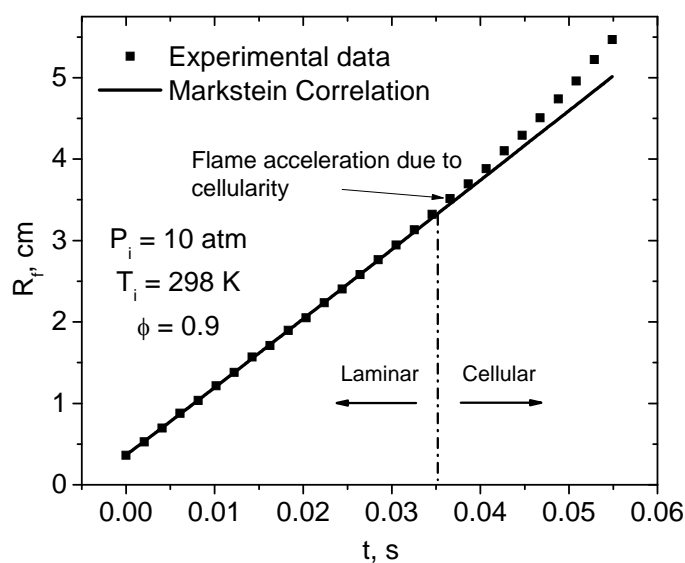
Figure 77. Flame radius versus time for methane/air at 10 atm
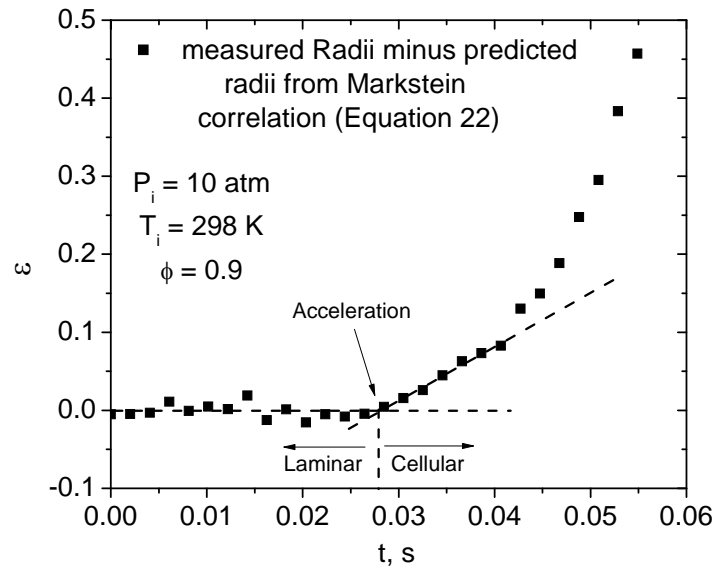
Figure 78. Residuals of measured flame radius minus predicted flame radius for methane/air at 10 atm; flame starts accelerating after approximately 30 ms
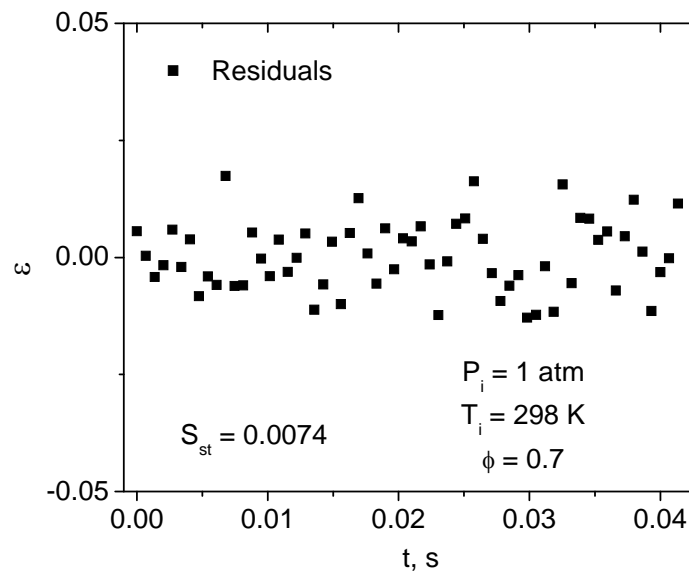
Figure 79. Residuals of measured flame radius minus predicted flame radius for methane/air at 1 atm; flame remains laminar and no acceleration is observed
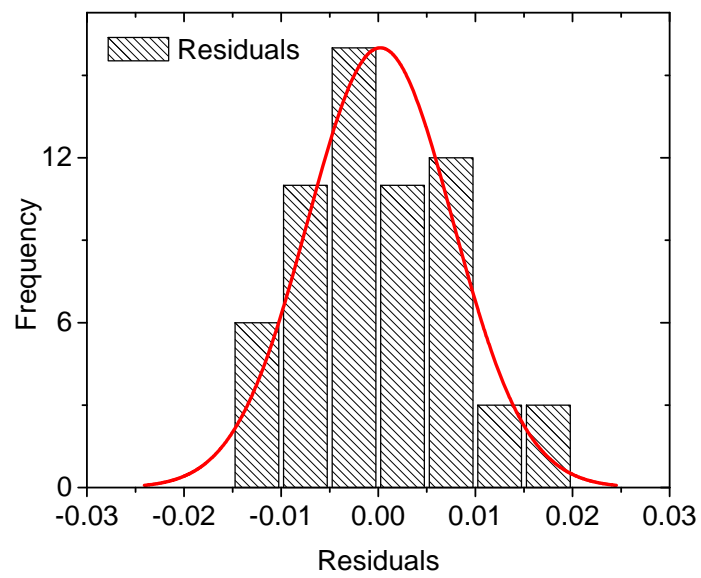
Figure 80. Histogram of residuals for atmospheric methane/air. Distribution seems random and normally distributed around zero

CHAPTER VI

CONCLUSIONS

6.1   Summary

This study focused on the design, construction, and operation of a high-pressure facility for measuring freely expanding, centrally ignited spherical flames. In addition, flame speeds were measured and analyzed for mixtures of methane, ethane, methane/ethane, and propane with air. Measured flame speed values were compared against chemical kinetic models.

The flame speed facility consists of an aluminum cylindrical vessel, a gas handling system, a vacuum system, high-speed camera optics, pressure transducers and thermocouple probes. For safety, the complete experimental apparatus is enclosed within a steel-reinforced, solid concrete cinderblock wall. All experiments were performed from a separate control room.

Mixtures were created using the partial pressure method after the vessel was evacuated to 50 mTorr by a rotary vane pump. Images were taken using a Cooke 1200hs high-speed camera at 2000 fps, resulting in 33-200 images per experiment, depending on the measured flame speed. The flame's density gradient was made visible via a Z-type schlieren optical setup powered by a 200 W mercury lamp. Images were analyzed using image tracking software and by best fitting a circle through the projection of the spherical flame front. Measured radii versus time were fitted by a flame speed/stretch relation proposed by Markstein, resulting in r^2 values of 0.9999 or better. Scatter of residuals between measured radii and those predicted by Markstein's linear model seem

randomly spread, normally distributed with a mean of zero and a standard deviation of approximately one third of the camera's spatial resolution (0.0074 cm).

A methodical uncertainty analysis was performed separating elemental uncertainties into systematic and random errors. This analysis, in combination with random uncertainties from repeated experiments, showed an overall uncertainty of approximately 1 cm/s. The uncertainty in initial temperature was reduced significantly by inserting a K-type thermocouple probe into the vessel, allowing for a local temperature measurement to be made before each experiment.

Values of measured atmospheric methane/air flame speeds were compared against several other studies and three chemical kinetic mechanisms: GRI 3.0, Curran's C_5 mechanism, and the San Diego mechanism (for stoichiometric methane/air mixtures). Results obtained in this study agree well with values obtained by other researchers. This is particularly true for flame speed measurements at 5 and 10 atm. Methane/air flame speed reduced significantly with increasing pressure. A reduced pressure effect was observed for ethane/air flame speeds. When plotted against adiabatic flame temperature, ethane flames were observed to be faster than methane flames showing flame acceleration due to kinetic or thermo diffusive effects.

For all measured mixtures, GRI 3.0 agreed remarkably well, since comparisons were made at conditions outside GRI 3.0's validity range. Curran's C_5 mechanism showed acceptable agreement at atmospheric conditions but under–predicted flame-speeds at high pressures and fuel rich conditions.

Interaction between flame speed and flame stretch was recorded and showed reverse trends for methane/air and ethane/air mixtures. With the exception of high-pressure, lean methane mixtures, all values of measured Markstein lengths were positive, showing a trend of increasing flame speed with decreasing flame stretch. For spherical flames, flame speeds increased with increased flame radii.

6.2   Recommendations

The flame speed facility built for this study is part of a long term project and will be used in several future studies. Based on the results obtained in this study, the following recommendations are made:

- Heating the flame speed vessel would allow experiments to be made at elevated temperatures. Since gas-turbine compressor discharge temperatures are much higher than 298 K, measuring flame speed's dependency on temperature as well as pressure would be a necessary next step.

- Future studies with hydrogen and carbon monoxide mixtures are expected to result in significantly higher flame speeds. The current camera's temporal resolution may not allow for capturing enough images used in the statistical analysis. Therefore, a camera capable of capturing 10,000 fps or more at full spatial resolution might be required for future studies.

- A laser absorption spectroscopy measurement in the infrared (3.39 μm) can validate initial hydrocarbon content in the vessel. This would validate initial equivalence ratios and establish required mixing times.

- Curran's C_5 mechanism needs improvement at elevated pressures, mainly in the stoichiometric and fuel rich regime. Care must be taken not to change kinetic parameters in such a fashion that the model's auto-ignition predictions are significantly altered.

REFERENCES

[1]   Energy Information Administration, 2008, *International Energy Outlook 2008* [online]. Available: www.eia.doe.gov/oiaf/ieo/index.html [accessed 20 December 2008]

[2]   IST World, 2004, *World Energy Technology Outlook -2050 (WETO-H$_2$)* [online]. Available: http://cordis.europa.eu/fetch?CALLER=FP6_PROJ &ACTION=D&DOC=2734&CAT=PROJ&QUERY=1170700785637&RCN=73 908 [accessed 15 December 2008]

[3]   Energy Information Administration, 2008, Annual *Energy Outlook 2009 Early Release* [online]. Available: http://www.eia.doe.gov/oiaf/aeo/ [accessed 20 December 2008]

[4]   Campbell A, Goldmeer J, Healy T, Washam R, Moliere M and Citeno J 2008 *ASME Turbo Expo 2008 (Berlin)* Paper nr. GT2008-51368

[5]   Lieuwen T, McDonell V, Petersen E L and Santavicca D 2006 *ASME Turbo Expo 2006 (Barcelona)* ASME Paper nr. GT2006-90770

[6]   Cohen H, Rogers G F C and Saravanamuttoo H I H 1996 *Gas Turbine Theory* 4th *ed* (Edingburg Gate, England: Pearson Education Limited)

[7]   Boyce M P 2006 *Gas Turbine Engineering Handbook, 3rd ed*. (Burlington, MA: Elsevier Inc)

[8]   Power-Technology.com, 2005, *Statkraft 800MW CCGT Knapsack, Cologne, Germany* [online]. Available: www.power-technology.com/projects/ knapsackccgt/ [accessed 22 December 2008]

[9]   GE Energy, 2009, [online]. Available: http://www.gepower.com/home/index.htm [accessed 5 january 2009]

[10]   Rolls Royce Energy, 2004, *Energy Technology* [online]. Available: http://www. rolls-royce.com/energy/tech/default.jsp [accessed 15 January 2009]

[11]   Samuelsen S 2006 *NETL Gas Turbine Handbook 3.2.1.1* p 209 [online]. Available: (http://www.netl.doe.gov/technologies/coalpower/turbines/ refshelf/handbook/TableofContents.html) [accessed 20 January 2009]

[12]   Bender W R 2006 *NETL Gas Turbine Handbook 3.2.1.2* p 217 [online]. Available: (http://www.netl.doe.gov/technologies/coalpower/turbines/ refshelf/handbook/TableofContents.html) [accessed 21 January 2009]

[13]   Sims G J, Mistry S L, Wood J P, Bowen P and Crayford A 2008 A Study Into The Auto-Ignition Characteristics of Hydrocarbon Fuels With Application To Gas Turbines *ASME Turbo Expo 2008 (Berlin)* Paper nr. GT2008-50824

[14]   Petersen E L, Hall J M, Smith S D, de Vries J, Amadio A R and Crofton M W 2007 Ignition of lean methane-based fuel blends at gas turbine pressures *J. Eng. for Gas Turbines Power* **129** 937-44

[15]   Bourque G, Healy D, Curran H, Zinner C, Kalitan D, de Vries J, Aul, C and Petersen E L 2008 Ignition and Flame Speed Kinetics of Two Natural Gas Blends with High Levels of Heavier Hydrocarbons ASME Turbo Expo 2008 (Berlin) Paper nr. GT2008-51344, 2008

[16]   de Vries J and Petersen E L 2007 Autoignition of methane-based fuel blends under gas turbine conditions *Proc. Combust. Inst.* **31** 3163–71

[17]   Lieuwen T C 2006 *NETL Gas Turbine Handbook 3.2.1 p* 197 [online]. Available: http://www.netl.doe.gov/technologies/coalpower/turbines/refshelf/handbook/ TableofContents.html [accessed 4 January 2009]

[18]   Lieuwen T C and Yang V 2005 *Combustion Instabilities in Gas Turbine Engines: Operational Experience, Fundamental Mechanisms, and Modeling* (Danvers, MA: AIAA)

[19]   Singh K, Varatharajan B, Yilmaz E, Han F and Kim K 2008 Effect of Hydrogen Combustion on the Combustion Dynamics of a Natural Gas Combustor ASME Turbo Expo 2008 (Berlin) Paper nr. GT2008-51343.

[20]   Dennis R 2006 *NETL Gas Turbine Handbook 6.0.1* p 1 [online]. Available: (http://www.netl.doe.gov/technologies/coalpower/turbines/refshelf/handbook/ TableofContents.html) [accessed 22 January 2009]

[21]   Mcdonell V G 2006 *NETL Gas Turbine Handbook 3.1* [online]. Available: (http://www.netl.doe.gov/technologies/coalpower/turbines/refshelf/handbook/ TableofContents.html) [accessed 22 January 2009]

[22]   Daniele S, Jansohn P and Boulouchos K 2008 Lean premixed combustion of undiluted syngas at gas turbine relevant conditions: NOx emissions and lean operational limits *ASME Turbo Expo 2008 (Berlin)* Paper nr. GT2008-50265

[23]   Turns S T 2000 *An Introduction to Combustion 2ⁿᵈ ed* (New York: McGraw-Hill)

[24]   Law C K 2006 *Combustion Physics* (New York: Cambridge University Press)

[25]   Williams F A 1985 *Combustion Theory 2nd ed.* (Boulder, CO: Westview Press)

[26]   Smith G P, Golden D M, Frenklach M, Moriarty N W, Eiteneer B, Goldenberg M, Bowman C T, Hanson R K, Song S, Gardiner W C, Lissianski V V and Qin Z, *GRI 3.0* [online]. Available: http://www.me.Berkeley.edu/gri-mech/ [accessed 15 December 2008]

[27]   Kuo K K *2002 Principles of Combustion 2nd ed.* (Hoboken, NJ: John Wiley & Sons, Inc)

[28]   de Vries J, Hall, Simmons S L, J M, Rickard M J A, Kalitan M D and Petersen E L 2007 Ethane ignition and oxidation behind reflected shock waves *Combust. Flame* **150** 137-50

[29]   Grillo A and Slack M W 1976 Shock tube study of ignition delay times in methane---oxygen---nitrogen---argon mixtures *Combust. Flame* **27** 377–81

[30]   Petersen E L, Davidson D F and Hanson R K 1999 Ignition Delay Times of Ram Accelerator CH_4 /O_2/Diluent Mixtures *J. Propul. Power* **15** 82–91

[31]   Bosschaart K J and de Goey L P H 2004 The laminar burning velocity of flames propagating in mixtures of hydrocarbons and air measured with the heat flux method *Combust. Flame* **136** 261-69

[32]   Konnov A A, Dayakov I V and De Ruyck J 2003 Measurement of adiabatic burning velocity in ethane - oxygen - nitrogen and in ethane - oxygen - argon mixtures *Exp. Therm. Fluid. Sci.* **27** 379-84

[33]   Manton J, Von Elbe G and Lewis B. 1953 Burning velocity measurements in a spherical vessel with central ignition Proc. Combust. Inst. **4** 358-63

[34]   Smith D and Agnew J T 1956 The effect of pressure on the laminar burning velocity of methane-oxygen-nitrogen mixtures *Proc. Combust. Inst*. **6** 83-88

[35]   Agrawal D D 1981 Experimental determination of burning velocity of methane-air mixtures in a constant volume vessel *Combust. Flame* **42** 243-52

[36]   Groff E D 1982 The cellular nature of confined spherical propane-air flames *Combust. Flame* **48** 51-62

[37]   Gülder L Ö 1982 Laminar burning velocities of methanol, ethanol and isooctane-air mixtures *Proc. Combust. Inst*. **19** 275-81

[38]   Iijima T and Takeno T 1986 Effects of temperature and pressure on burning velocity *Combust. Flame* **65** 35-43

[39] Aung K T, Hassan M I and Faeth G M 1997 Flame stretch interaction of laminar premixed hydrogen/air flames at normal temperature and pressure *Combust. Flame* **109** 1-24

[40] Bradley D, Gakell P H and Gu X J 1996 Burning velocities, Markstein lengths, and flame quenching for spherical methane-air flames: A computational study *Combust. Flame* **104** 176-98

[41] Elia M, Ulinski M and Metghalchi M Laminar burning velocity of methane–air–diluent mixtures 2001 *Trans. ASME* **123** 190-96

[42] Radwan M, Ismael M, Younes Selim M, Saleh H and Salem H 2001 Laminar burning velocity of some coal derived fuels *Energy Sources Part A* **23** 345-61

[43] Lamoureux N, Djebaili-Chaumeix N and Paillard C E 2003 Laminar flame velocity determination for H_2−air−He−CO_2 mixtures using the spherical bomb method *Exp. Therm. Fluid, Sci*. **27** 385-93

[44] Saeed K and Stone C R 2004 Measurements of the laminar burning velocity for mixtures of methanol and air from a constant-volume vessel using a multizone model *Combust. Flame* **139** 152-66

[45] Dahoe A E 2005 Laminar burning velocities of hydrogen–air mixtures from closed vessel gas explosions *J. Loss Prev. Process. Ind*. **18** 152-66

[46] Ilbas M, Crayford A P, Yılmaz I, Bowen P J and Syred N 2006 Laminar-burning velocities of hydrogen-air and hydrogen-methane-air mixtures: an experimental study *Int. J. Hydrogen Energy* **31** 1768-79

[47] Johnston R J and Farrell J T 2005 Laminar burning velocities and Markstein lengths of aromatics at elevated temperature and pressure *Proc. Combust. Inst*. **30** 217-24

[48] Takizawa K, Takahashi A, Tokuhashi K, Kondo S and Sekiya A 2005 Burning velocity measurement of fluorinated compounds by spherical-vessel method *Combust. Flame* **141** 298-07

[49] Kitagawa T 2005 Effects of pressure on burning velocity and instabilities of propane-air premixed flames *JSME Int. J. Ser. B* **48** 2-8

[50] Huang Z, Zhang Y, Zeng K, Liu B, Wang Q and Jiang, D 2006 Measurements of laminar burning velocities for natural gas-hydrogen-air mixtures *Combust. Flame* **146** 302-11

[51]   Tse S D, Zhu D L and Law C K 2000 Morphology and burning rates of expanding spherical flames in H_2/O_2/inert mixtures up to 60 atmospheres *Proc. Combust. Inst*. **28** 1793-800

[52]   Groff E D 1982 The cellular nature of confined spherical propane-air flames *Combust. Flame* **48** 51-62

[53]   Manton J, von Elbe G and Lewis B 1951 Nonisotropic propagation of combustion waves in explosive gas mixtures and the development of cellular flames *J. Chem. Phys*. **20**, 153-57

[54]   Dowdy R D, Smith D B, Taylor S C and Williams A 1990 The use of expanding spherical flames to determine burning velocities and stretch effects in hydrogen/air mixtures *Proc. Combust. Inst*. **23** 325-32

[55]   Hassan M I, Aung K T, Kwon O C and Faeth G M 1998 Properties of laminar premixed hydrocarbon/air flames at various pressures *J. Propul. Power* **14** 479-88

[56]   Bradley D, Hicks R A, Lawes M., Sheppard C G W and Woolley R 1998 The measurements of laminar burning velocities and Markstein numbers for iso-octane air and iso-*n*-heptane mixture at elevated temperatures and pressures in an explosion bomb *Combust. Flame* **115** 126-44

[57]   Rozenchan G, Zhu D L, Law C K and Tse S D 2002 Outward propagation, burning velocities, and chemical effects of methane flames up to 60 atm *Proc. Combust. Inst*. **29** 1461-69

[58]   Clingman W H, Brokaw R S and Pease R N 1952 Burning velocities of methane with nitrogen-oxygen, argon-oxygen and helium-oxygen mixtures *Proc. Combust. Inst.* **4** 310-13

[59]   Edmondson H and Heap M P 1969 The burning velocity of methane-air flames inhibited by methyl bromide *Combust. Flame* **13** 472-78

[60]   Edmondson H and Heap M P 1970 Ambient atmosphere effects in flat-flame measurements of burning velocity *Combust. Flame* **14** 195-202

[61]   Andrews G E and Bradley D 1972 The burning velocity of methane-air mixtures *Combust. Flame* **19** 275-88

[62]   Günther R and Janisch G 1972 Measurements of burning velocity in a flat flame front *Combust. Flame* **19** 49-53

[63]   Wu C K and Law C K 1984 On the determination of laminar flame speeds from stretched flames *Proc. Combust. Inst.* **20** 1941-9

[64]   Iijima T and Takeno T 1986 Effects of temperature and pressure on burning velocity *Combust. Flame* **65** 35-43

[65]   Kawakami T, Okajima S and Iinuma K 1988 Measurement of slow burning velocity by zero-gravity method Proc. *Combust. Inst.* **22** 1609-13

[66]   Egolfopoulos F N, Zhu D L and Law C K 1990 Experimental and numerical determination of laminar flame speeds: mixtures of C2-hydrocarbons with oxygen and nitrogen *Proc. Combust. Inst.* **23** 471-8

[67]   van Maaren A, Thung D S and de Goey L P H 1994 Measurement of flame temperature and adiabatic burning velocity of methane/air mixtures *Combust. Sci. Technol.* **96** 327-44

[68]   Clarke A, Stone R and Beckwith P 1995 The measurement of the laminar burning velocity of methane/diluent/air mixtures in a constant volume combustion bomb in a micro-gravity environment *J. Inst. Energy* **68** 130-6

[69]   Vagelopoulos C M and Egolfopoulos F N 1998 Direct experimental determination of laminar flame speeds *Proc. Combust. Inst.* **27** 513-9

[70]   Gu X J, Haq M Z, Lawes M and Woolley R 2000 Laminar burning velocity and Markstein lengths of methane-air mixtures *Combust. Flame* **121** 41-58

[71]   Bosschaart K J, de Goey L P H and Burgers J M The laminar burning velocity of flames propagating in mixtures of hydrocarbons and air measured with the heat flux method 2004 *Combust. Flame* **136** 261-9

[72]   Konnov A A, Dyakov I V and De Ruyck J 2003 Measurement of adiabatic burning velocity in ethane - oxygen - nitrogen and in ethane - oxygen - argon mixtures *Exp. Therm. Fluid Sci.* **27** 379-84

[73]   Jomaas G, Zheng X L, Zhu D L and Law C K 2005 Experimental determination of counterflow ignition temperatures and laminar flame speeds of C2-C3 hydrocarbons at atmospheric and elevated pressures *Proc. Combust. Inst.* **30** 193-200

[74]   Singer J M 1952 Burning velocity measurements on slot burners; comparison with cylindrical burner determinations *Proc. Combust. Inst.* **4** 352-358

[75]   Law C K, Peters N and Rogg B 1993 *Reduced Kinetic Mechanisms for Application in Combustion Systems* (Berlin: Springer-Verlag)

[76]   Kitagawa T 2005 Effects of pressure on burning velocity and instabilities of propane-air premixed flames *JSME Int. J. Ser. B* **48** 2-8

[77]   Zhao Z, Kazakov A, Juan L and Dryer F 2004 The initial temperature and N_2 dilution effect on the laminar flame speed of propane/air *Combust. Sci. and Tech.* **176** 1705-23

[78]   Strehlow R A 1984 *Combustion Fundamentals* (New York: McGraw-Hill, Inc)

[79]   Landau L 1944 On the theory of slow combustion *Acta Physicochim*, URSS, **19** 77-85

[80]   Darrieus G 1938 Propagation d'un front de flamme *Presented at La Technique Moderne (Paris) and in 1945 at Congr`es de M´ecanique Appliqu´ee (Paris)*

[81]   Karlovitz B, Denniston D and Wells F 1951 Investigation of turbulent flames *J. Chem. Phys.* **19** 541-7

[82]   American Society of Mechanical Engineers 2000 *Boiler and Pressure Vessel Code* (New York: ASME)

[83]   American Society for Metals 1993 *Metals Handbook* (ASM) Volume 1 & 2

[84]   Petersen E L, Rickard M J A, Crofton M D, Abbey E D, Traum M J and Kalitan, D M 2005 A facility for gas- and condensed-phase measurements behind shock waves *Meas. Sci. Technol.* **16** 1716–29

[85]   Settles G S 2006 *Schlieren and Shadowgraph Techniques 1ˢᵗ ed.* Springer (Heidelberg, Germany: Springer)

[86]   Klimek R and Wright T 2006 *Spotlight-8 Image Analysis Software* NASA/TM-2006-214084

[87]   Chen Z and Ju Y 2007 On the accurate determination of flame speeds at normal and elevated pressures by using a spherical bomb: the effects of compression and stretch *45th AIAA Aerospace Sciences Meeting and Exhibit (Reno, NV)* AIAA 2007-378

[88]   Markstein G H 1964 *Non-Steady Flame Propagation* (New York: Pergamon)

[89] Sharma S P, Agrawal D D and Gupta C P 1981 The pressure and temperature dependence of burning velocity in a spherical combustion bomb *Proc. Combust. Inst*. **18** 493-501

[90] Kee R J, Rupley F M, Meeks E and Miller J A 1996 *A Fortran chemical kinetics package for the analysis of gas phase chemical and plasma* (Sandia Report SAND96-8216)

[91] JANNAF 1971 *Thermo-chemical Tables* Natl. Stand. Ref. Data Ser. (NSRDS-NBS 37); also Dow Chemical Company 1965 distributed by Clearinghouse for Federal Scientific and Technical Information (PB168370)

[92] McBride B J and Gordon S 1967 *FORTRAN IV Program for calculation of thermodynamic data* (NASA TN D-4097)

[93] Hirschfelder J O, Curtiss C F and Bird R B 1954 *Molecular Theory of Gases and Liquids* (New York: John Wiley and Sons)

[94] Warnatz J 1982 *Numerical Methods in Flame Propagation* e*dited by N. Peters and J. Warnatz* (Weisbaden, Germany: Friedr. Vieweg and Sohn)

[95] Wilke C R 1950 A viscosity equation for gas mixtures *J. Chem. Phys.* **18** 517-9

[96] Bird R B, Stewart W E and Lightfoot E N 1960 *Transport Phenomena* (New York: John Wiley and Sons)

[97] Mathur S, Tondon P K and Saxena S C 1967 Thermal conductivity of binary, ternary and quaternary mixtures of rare gases Mol. Phys. **12** 569-79

[98] Kee R J, Rupley F M, Miller J A, Coltrin M E, Grcar J F, Meeks E, Moffat H K, Lutz A E, Dixon-Lewis G, Smooke M D, Warnatz J, Evans G H, Larson R S, Mitchell R E, Petzold L R, Reynolds W C, Caracotsios M, Stewart W E, Glarborg P, Wang C and Adigun O 2001 *PREMIX: A Program for Modeling Steady, Laminar, One-dimensional Premixed Flames* (San Diego: Reaction Design)

[99] Spalding B 1956 The theory of flame phenomena with a chain reaction *Philos. Trans. R. Soc. London* **249** 1-25

[100] Wilde K A 1972 Boundary-value solutions of the one-dimensional laminar flame propagation equations *Combust. Flame* **18** 43-52

[101] Kendall R M and Kelly J T 1978 *Premixed One-Dimensional Flame (PROF) Code User's Manual* (EPA Report EPA-600/7-78-172a)

[102] Seery D J and Bowman C T 1970 An experimental and analytical study of methane oxidation behind shock waves *Combust. Flame* **14** 37-47

[103] Hidaka Y, Gardiner W C and Eubank C S 1982 Shock tube an modeling study of the ignition chemistry of small hydrocarbons *J. of Mol. Sci. China* **2** 141-53

[104] Frenklach M and Bornside D E 1984 Shock-initiated ignition in methane-propane mixtures *Combust. Flame* **56** 1-27

[105] Spadaccini L J and Colket M B 1994 Ignition delay characteristics of methane fuels *Prog. Energy Combust. Sci.* **20** 431-59

[106] Chang A Y Davidson D F, DiRosa M, Hanson R K and Bowman C T 1994 *Proc. Combust. Inst.* **23** (Poster 3-23)

[107] Davidson D F, DiRosa M, Chang A Y Hanson R K and Bowman C T 1992 A shock tube study of methane decomposition using laser absorption by CH_3 *Proc. Combust. Inst.* **24** 589-96

[108] Yu C L, Wang C and Frenklach M 1995 Chemical kinetics of methyl oxidation by molecular oxygen *J. Phys. Chem.* **99** 14377-87

[109] Eiteneer B, Yu C L, Goldenberg M and Frenklach M 1998 Determination of rate coefficients for reactions of formaldehyde pyrolysis and oxidation in the gas phase J. *Phys. Chem. A* **102** 5196-205

[110] Hidaka Y, Taniguchi T, Tanaka H, Kamesawa T, Inami K and Kawano H 1993 Shock-tube study of CH_2O pyrolysis and oxidation *Combust. Flame* **92** 365-76

[111] Healy D, Curran H J, Dooley S, Simmie J M, Kalitan D M, Petersen E L and Bourque G 2008 Methane/ethane/propane mixture oxidation at high pressures and at high, intermediate and low temperatures *Combust. Flame* **155** 451-61

[112] Healy D, Curran H J, Simmie J M, Kalitan D M, Zinner C M, Barrett A B, Petersen E L and G. Bourque 2008 *Combust Flame* **155** 441–8

[113] Petersen E L, Kalitan D M, Simmons S, Bourque G, Curran H J and Simmie J M 2007 Methane/propane oxidation at high pressures: experimental and detailed chemical kinetic modeling *Proc. Combust. Inst.* **31** 447-54

[114] Hessler J P 1998 Calculation of reactive cross sections and micro-canonical 61 rates from kinetic and thermo-chemical data *J. Phys. Chem. A* **102** 4517–26

[115] Curran H J, Gaffuri P, Pitz W J and Westbrook C K 1998 A comprehensive modeling study of *n*-heptane oxidation *Combust. Flame* **114** 149–77

[116] Curran H J, Gaffuri P, Pitz W J and Westbrook C K 2002 A comprehensive modeling study of iso-octane oxidation *Combust. Flame* **129** 253–8

[117] Petrova M V and Williams F A 2006 A small detailed chemical-kinetic mechanism for hydrocarbon combustion *Combust. Flame* **144** 526-44

[118] Taylor S C 1991 *Burning Velocity and the Influence of Flame Stretch* (Leeds, England: Ph.D. Dissertation, University of Leeds)

[119] Vagelopoulos C M and Egolfopoulos F N 1994 Laminar flame speeds and extinction strain rates of mixtures of carbon monoxide with hydrogen, methane, and air *Proc. Combust. Inst.* **25** 1317-23

[120] Reynolds W C 1986 *The Element Potential Method for Chemical Equilibrium Analysis: Implementation in the Interactive Program STANJAN* (Stanford, CA: Mechanical Engineering Department, Stanford University)

[121] Searby G and Quinard J 1990 Direct and indirect measurements of Markstein numbers of premixed flames *Combust. Flame* **82** 298-311

[122] Durox D, Ducruix S and Candel S 2001 Experiments on collapsing cylindrical flames *Combust. Flame* **125** 982-1000

[123] Halter F, Chauveau C, Djebaïli-Chaumeix N and Gökalp I 2005 Characterization of the effects of pressure and hydrogen concentration on laminar burning velocities of methane-hydrogen-air mixtures *Proc. Combust. Int.* **30** 201-8
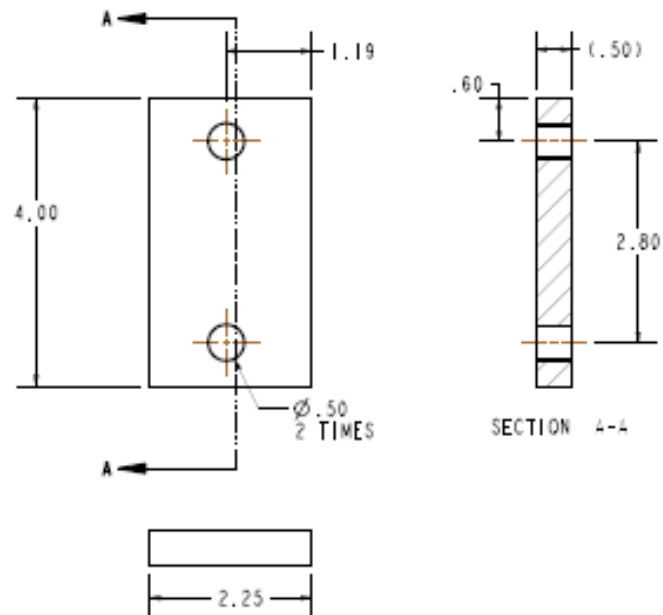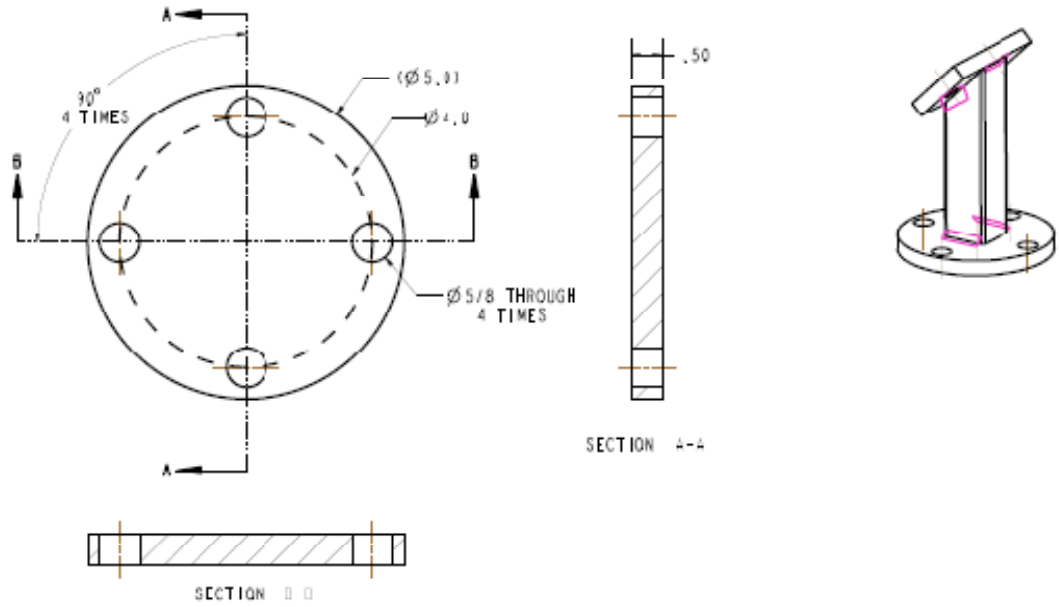
APPENDIX A
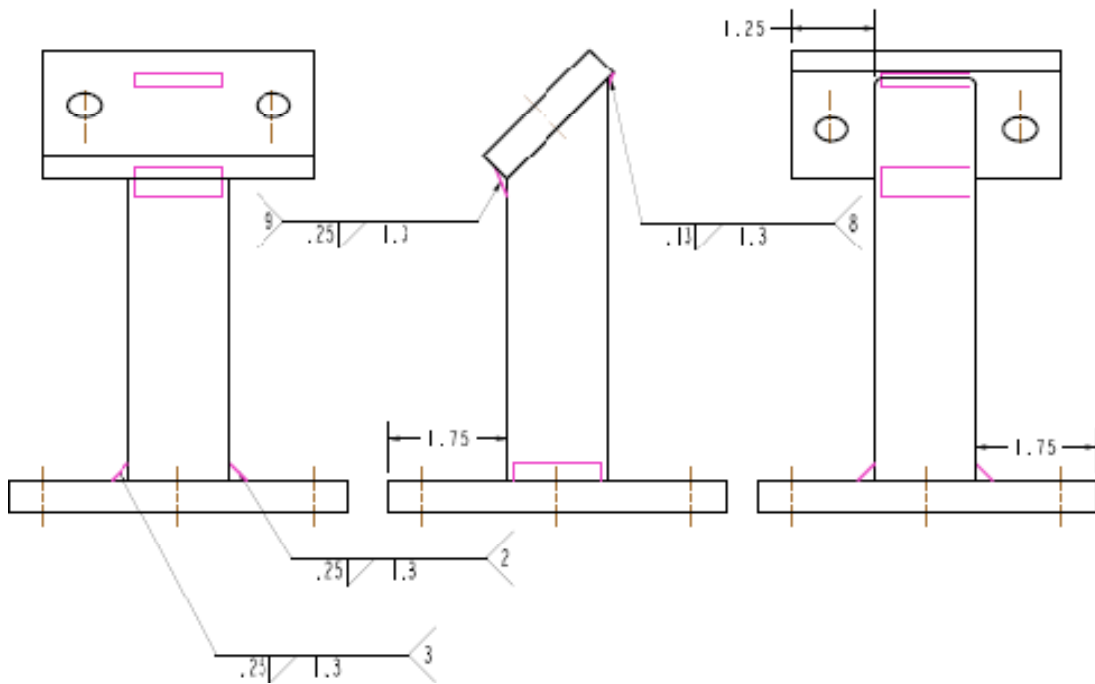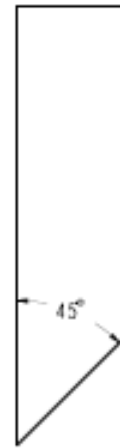
Table 1-2
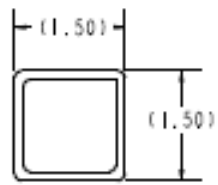Economic and Operation Characteristics of Plant

Type of Plant	Capital Cost $/kW	Heat Rate Btu/kWh kJ/kWh	Net Efficiency	Variable Operation & Maintenance ($/MWh)	Fixed Operation & Maintenance ($/MWh)	Availability	Reliability	Time from Planning to Completion Months
Simple cycle gas turbine (2500 °F/1371 °C) natural gas fired	300-350	7582-8000	45	5.8	0.23	88-95%	97-99%	10-12
Simple cycle gas turbine oil fired	400-500	8322-8229	41	6.2	0.25	85-90%	95-97%	12-16
Simple cycle gas turbine crude fired	500-600	10662-11250	32	13.5	0.25	75-80%	90-95%	12-16
Regenerative gas turbine natural gas fired	375-575	6824-7200	50	6.0	0.25	86-93%	96-98%	12-16
Combined cycle gas turbine	600-900	6203-6545	55	4.0	0.35	86-93%	95-98%	22-24
Advanced gas turbine combined cycle power plant	800-1000	5249-5538	65	4.5	0.4	84-90%	94-96%	28-30
Combined cycle coal gasification	1200-1400	6950-7332	49	7.0	1.45	75-85%	90-95%	30-36
Combined cycle fluidized bed	1200-1400	7300-7701	47	7.0	1.45	75-85%	90-95%	30-36
Nuclear power	1800-200	10000-10550	34	8	2.28	80-89	92-98%	48-60
Steam plant coal fired	800-1000	9749-10285	35	3	1.43	82-89%	94-97%	36-42
Diesel generator-diesel fired	400-500	7582-8000	45	6.2	4.7	90-95%	96-98%	12-16
Diesel generator-power plant oil fired	600-700	8124-8570	42	7.2	4.7	85-90%	92-95%	16-18
Gas engine generator power plant	650-750	7300-7701	47	5.2	4.7	92-96%	96-98%	12-16

APPENDIX B

	Diesel Fuel Burner Fuel				High-Ash Crude Heavy Residual	Typical Libyan Crude	Navy Distillate	Heavy Distillate	Low-Ash Crude
	Kerosene	#2	Oil #2	JP-4					
Flash point °F	130/160	118–220	150/200	< RT	175/265		186°F	198	50/200
Pour point °F	−50	−55 to +10	−10/30		15/95	68	10°F		15/110
Visc. CS @ 100°F	1.4/2.2	2.48/2.67	2.0/4.0	.79	100/1,800	7.3	6.11	6.20	2/100
SSU		34.4					45.9		
Sulfur %	.01/.1	.169/.243	.1/.8	.047	.5/4	.15	1.01	1.075	.1/2.7
API gr.		38.1	35.0	53.2			30.5		
Sp. gr. @ 100°F	.78/.83	.85	.82–.88	.7543@60°F	.92/1.05	.84	.874	.8786	.80/.92
Water & sed.			0			.1%wt			
Heating value Btu/lb	19,300/ 19,700	18,3 30	19,000/19,600	18,700/ 18,820	18,300/18,900	18,250		18,239	19,000/19,400
Hydrogen %	12.8/14.5	12.83	12/13.2	14.75	10/12.5			12.40	12/13.2
Carbon residue 10% bottoms	.01/.1	.104	.03/.3			2/10			.3/3
Ash ppm	1/5	.001	0/20		100/1,000	36ppm			20/200
Na + K ppm	01.5		0/1		1/350	2.2/4.5			0/50
V	0/.1		0/.1		5/400	0/1			0/15
Pb	0/.5		0/1		0/25				
Ca	0/1	0/2	0/2		0/50				

APPENDIX C

30°
4 TIMES

(Ø5.0)

Ø4.0

Ø5/8 THROUGH
4 TIMES

.50

SECTION A-A

SECTION B B

1.19

4.00

Ø.50
2 TIMES

(.50)

.60

2.80

SECTION A-A

2.25

APPENDIX D

APPENDIX E

1/8-40 UNC-2B

Ø.375 STOCK

A

.05
(2 TIMES)

1/8-40 UNC-2B

45.0°
(2 TIMES)

1.00

A

.50

.188

SECTION A-A

Ø.066

APPENDIX F

SEE DETAIL A

SCALE 0.200

SECTION AA-AA

DETAIL A
SCALE 0.500

3.00   2.50

APPENDIX G

SEE DETAIL A

12.00

15.00

.50
(0.25 FOR TC)

1.50

1/2'' NPT
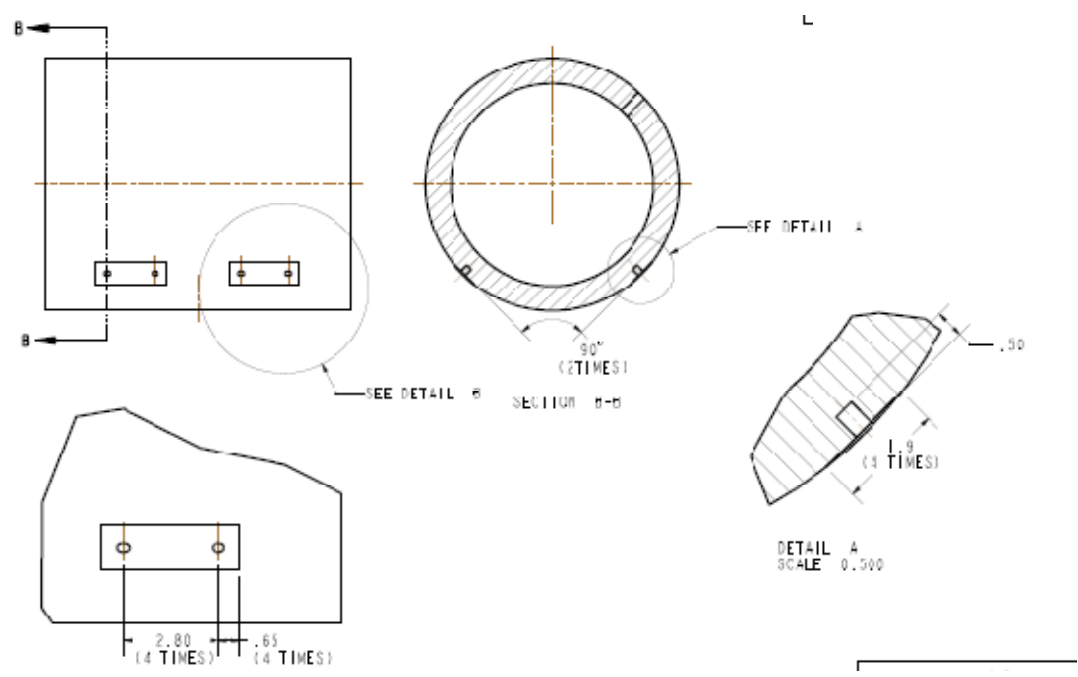(1/4'' NPT FOR
THERMOCOUPLE)

DETAIL A
SCALE 0.300

APPENDIX H

DETAIL A
SCALE 0.500
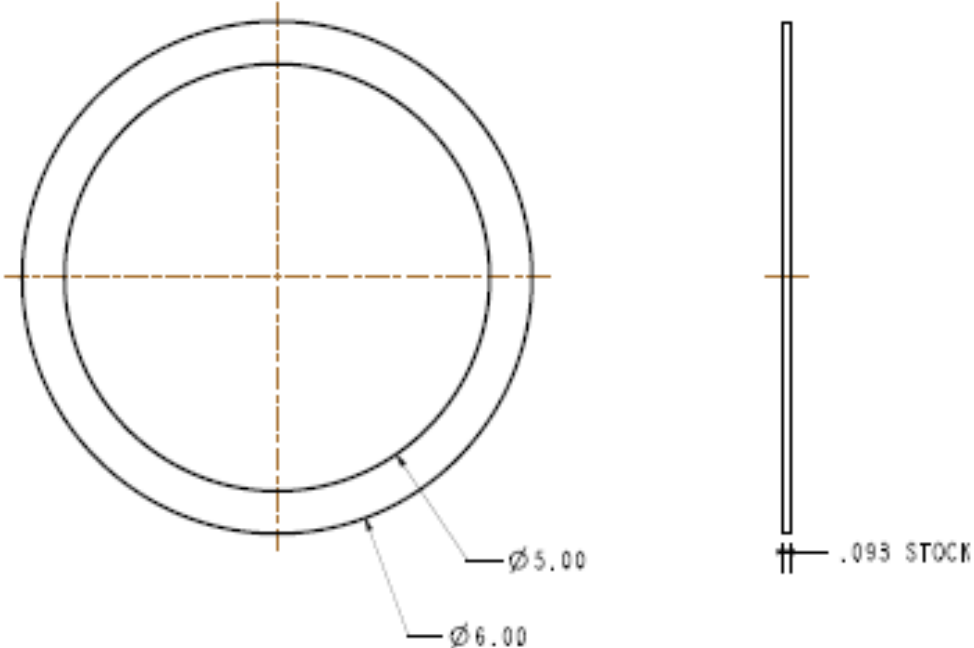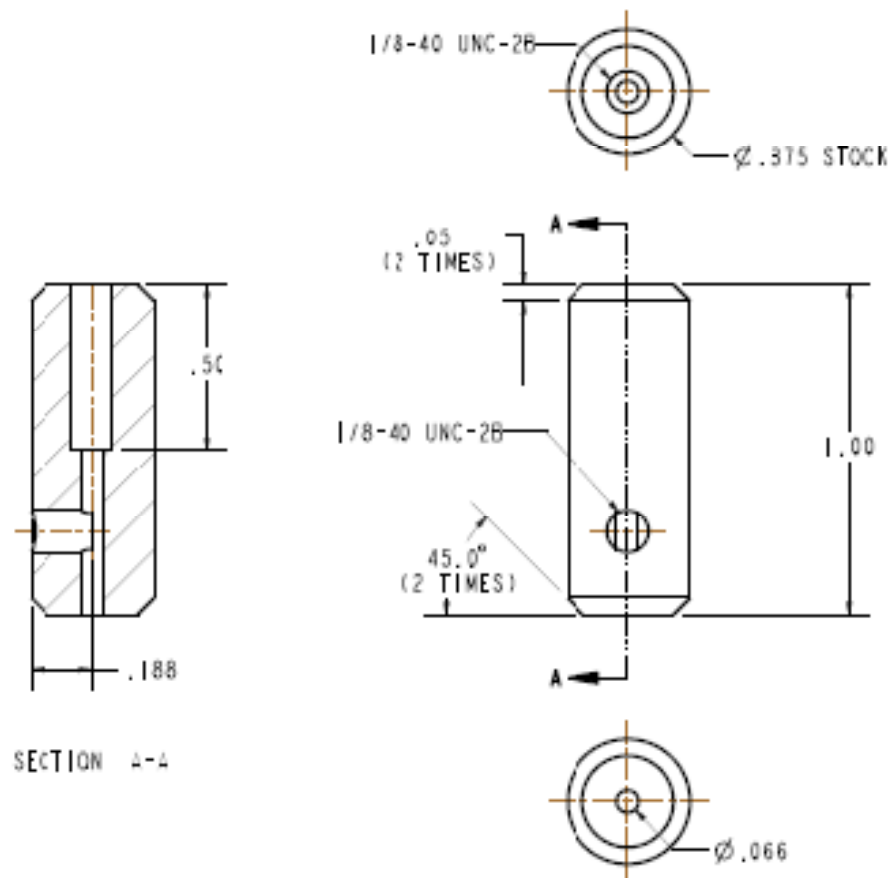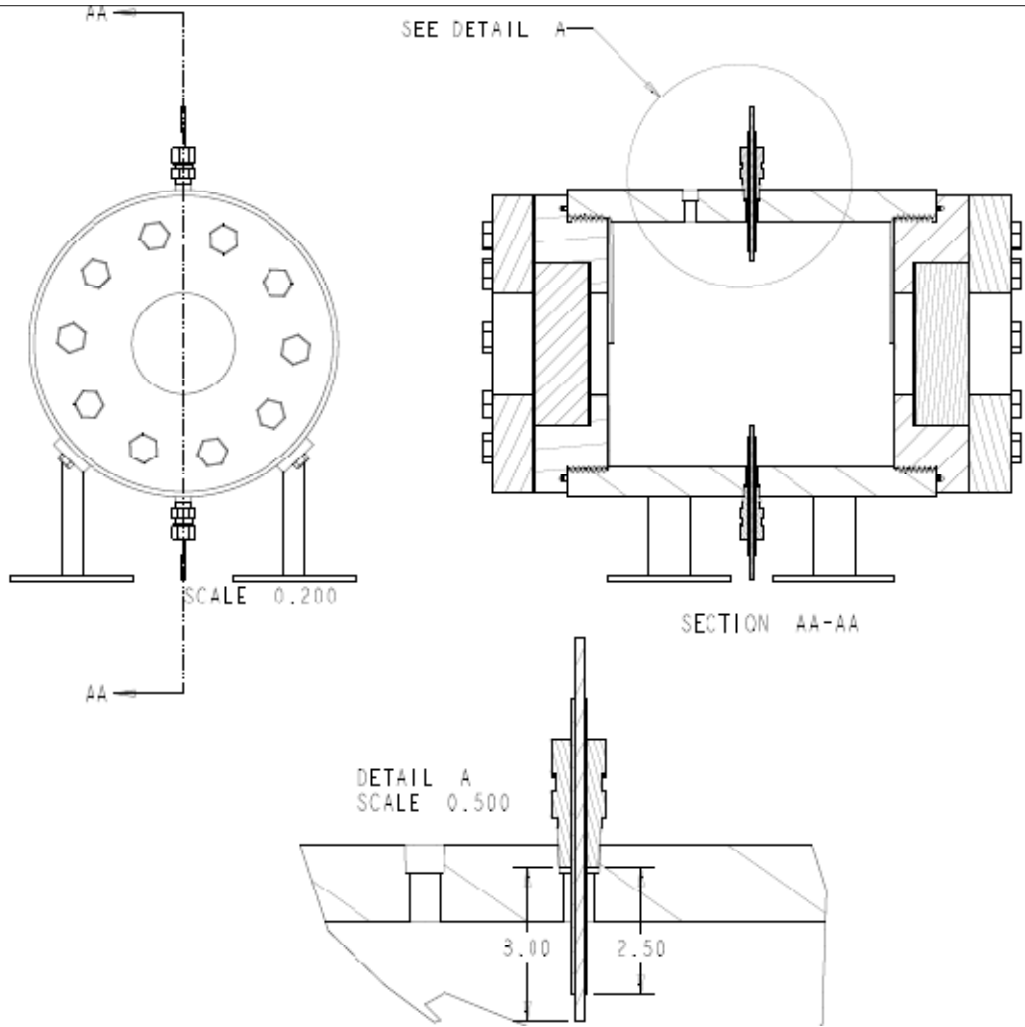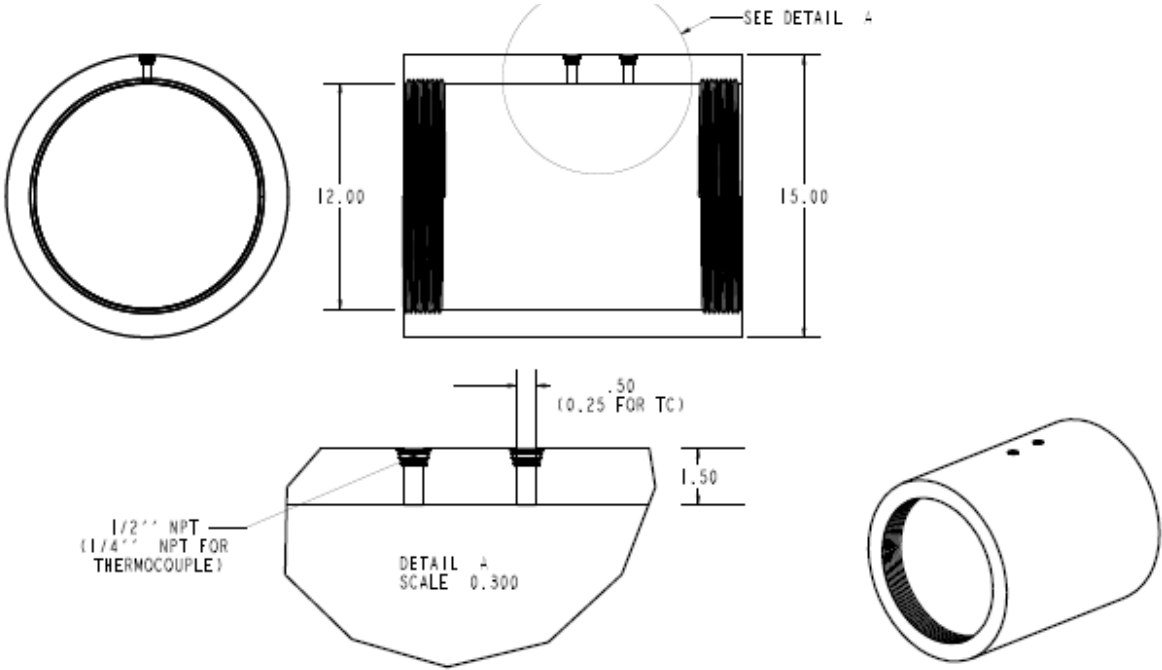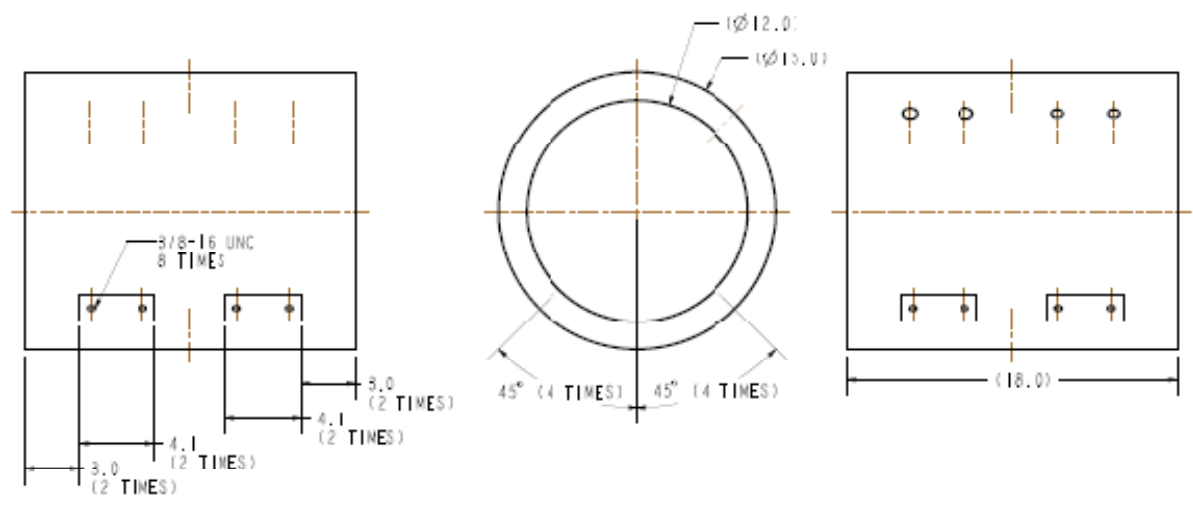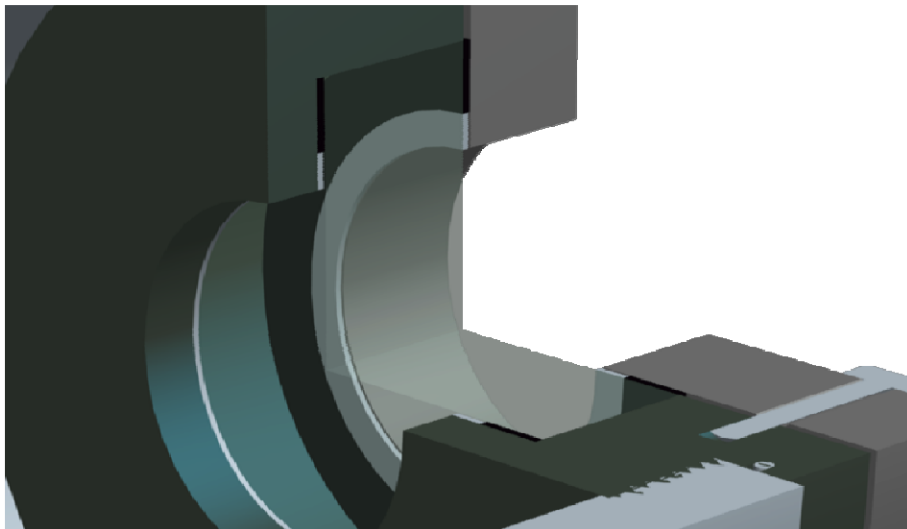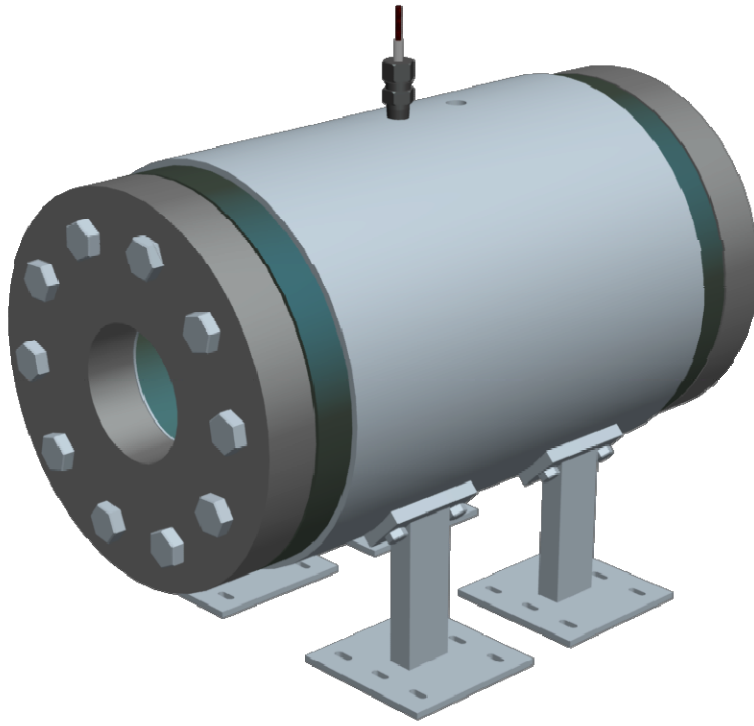
APPENDIX I

APPENDIX J

```
/    Freely propagating flame
/    Kinetic mechanism: GriMech
FREE
ENRG
/    Initial flow rate estimate
FLRT  0.04   ! gm/cm**2-sec
PRES  10    ! atmospheres
/    Initial grid and profile specifications
NPTS   10
XEND      0.5
XSTR      0
XCEN      0.1
WMIX      1
/    Temperature to be fixed for the flame speed computation
TFIX  400.
SPOS  1.0E-12
/    Mesh adaptation criteria
GRAD      0.99
CURV      0.99
/    Unreacted fuel-oxidizer makeup
/ Phi 0.7
MOLE
REAC CH4    1
REAC C2H6    0
REAC CO    0
REAC CO2    0
REAC H2    0
REAC O2    2.85714285714286
REAC N2    10.7428571428571
REAC H2O    0
/    Estimated products mole fraction
PROD CO 0
PROD CO2 1
PROD H2O 2
PROD N2 10.7428571428571
PROD O2 0.857142857142857
PROD CH4 0
PROD C2H6 0
PROD H2 0
/    Estimated peak intermediate mole fractions
INTM  CO      0.08
INTM  HCO     0.000001
INTM  HO2     0.0001
INTM  O       0.0001
INTM  H2O2    0.0001
INTM  H       0.02
INTM  H2      0.01
INTM  OH      0.001
INTM  CH2     0.0001
INTM  CH      0.00001
```

```
INTM  CH2O    0.001
INTM  CH3     0.0005
/   Convergence tolerance for Newton
ATOL  1.E-5
RTOL  1.E-4
/   Convergence tolerance for timestepping
ATIM  1.E-5
RTIM  1.E-5
/   Maximum printing
PRNT   1
/   Time step control
TIME   100   5.0E-7   ! sec
TIM2   200   1.0E-6   ! sec
/   Estimated temperature profile
TEMP   0.0      298.
TEMP   0.02     300.
TEMP   0.03     325.
TEMP   0.04     450.
TEMP   0.05     750.
TEMP   0.06     1200.
TEMP   0.07     1800.
TEMP   0.1      1900.
TEMP   0.2      1925.
TEMP   0.35     1935.
TEMP   10.0     1950.
/
/   a continuation run will follow
/   Phase 1 of 9
CNTN
END
/
PRES   10
/ Phi 0.7
MOLE
GRAD   0.8725
CURV   0.8725
XSTR   -0.125
XEND   0.8125
/
/   a continuation run will follow
/   Phase 2 of 9
CNTN
END
/
PRES   10
/ Phi 0.7
MOLE
GRAD   0.755
CURV   0.755
XSTR   -0.25
XEND   1.125
/
/   a continuation run will follow
```

```
/    Phase 3 of 9
CNTN
END
/
PRES   10
/ Phi 0.7
MOLE
GRAD   0.6375
CURV   0.6375
XSTR   -0.375
XEND   1.4375
/
/   a continuation run will follow
/    Phase 4 of 9
CNTN
END
/
PRES   10
/ Phi 0.7
MOLE
GRAD   0.52
CURV   0.52
XSTR   -0.5
XEND   1.75
/
/   a continuation run will follow
/    Phase 5 of 9
CNTN
END
/
PRES   10
/ Phi 0.7
MOLE
GRAD   0.4025
CURV   0.4025
XSTR   -0.625
XEND   2.0625
/
/   a continuation run will follow
/    Phase 6 of 9
CNTN
END
/
PRES   10
/ Phi 0.7
MOLE
GRAD   0.285
CURV   0.285
XSTR   -0.75
XEND   2.375
/
/   a continuation run will follow
/    Phase 7 of 9
```

```
CNTN
END
/
PRES   10
/ Phi 0.7
MOLE
GRAD   0.1675
CURV   0.1675
XSTR   -0.875
XEND   2.6875
/
/   a continuation run will follow
/   Phase 8 of 9
CNTN
END
/
PRES   10
/ Phi 0.7
MOLE
GRAD   0.0500000000000003
CURV   0.0500000000000003
XSTR   -1
XEND   3
/
/   a continuation run will follow
/   Phase 9 of 9
END
```

VITA

Jaap de Vries received his bachelor degree in Aircraft Operations from the College of Amsterdam, The Netherlands, in 2002. He entered the Aerospace Engineering program at the University of Central Florida in 2004 and received his Master of Science degree in December 2005. During his graduate work de Vries published 5 journal articles and 25 conference papers. He also presented at 13 national and international conferences and symposia, while maintaining a 4.0 grade point average on all graduate work. His research interests include gas turbine combustion, heat transfer, flame chemistry, and design of experiment.

In 2008 Jaap de Vries won the best paper award at the Gas Turbine Expo in Berlin, Germany. He also won the best Graduate Teaching Award for teaching Heat Transfer (MEEN 461) in the fall of 2008.

Jaap de Vries can be reached at Texas A&M Turbomachinery Laboratory Room 236, Corner of George Bush and 2818, College Station, TX, 77843. His email is jpdvrs@yahoo.com.